POINT-OF-CARE BIOSENSING PLATFORM BASED ON PHOTOLUMINESCENT NANOPARTICLES AND MICROFLUIDIC BIOCHIP FOR IN-VITRO BIOMARKERS DIAGNOSTICS

LIU YUAN

PhD

The Hong Kong Polytechnic University

2025

The Hong Kong Polytechnic University

Department of Applied Physics

Point-of-care Biosensing Platform Based on Photoluminescent Nanoparticles and Microfluidic Biochip for In-Vitro Biomarkers Diagnostics

LIU Yuan

A thesis submitted in partial fulfillment of the requirements for
the degree of Doctor of Philosophy

August 2024

CERTIFICATE OF ORIGINALITY

I hereby declare that this thesis is my own work and that, to the best of my knowledge and belief, it reproduces no material previously published or written, nor material that has been accepted for the award of any other degree or diploma, except where due acknowledgement has been made in the text.

______________________________(Signed)

__________LIU YUAN__________(Name of student)

Abstract

Identifying biomarkers with high sensitivity and portability is of significant importance for screening and managing diseases that threaten human health. Compared with some commercial biomarkers diagnostic methods, the developed point-of-care biosensing platform possesses various advantages involving easy to operation, low cost, portable, and rapid, which implies potential application in the future.

In terms of the biomarker of Nucleocapsid protein (N protein) detection, the point-of-care biosensing platform based on UCNPs and microfluidic biochip was designed and fabricated. The UCNPs were successfully synthesized and used as the luminescent agent. The microfluidic biochip was utilized as the detection chamber of the portable virus diagnostic platform, which possesses luminescence enhancement properties with a maximum of over 100-fold than the cuvette samples. Moreover, the cleanable property of microfluidic biochip also implied promised application for the virus diagnosis area. Compared with the typical commercial rapid test strips for virus detection, this biosensing platform exhibited a higher sensitivity of around 1.12 pg/ml for N protein detection. In addition, the clinical samples are also investigated and manifested that the designed point-of-care virus detection platform possessed better diagnostic sensitivity compared with the normal commercial LFA rapid test strips.

For the carcinoembryonic antigen (CEA) tumor marker diagnostics, the developed point-of-care biosensing platform based on QDs luminescence and microfluidic biochip with machine vision algorithm analysis was well-designed and manufactured. The core-shell QDs nanoparticles with excellent luminescent properties were employed for the labelling indicator in the immunoassay. The microfluidic biochip with excellent separation and cleanable abilities was utilized as assisted chamber for the biosensing platform, which illustrated a sensitivity of around 0.021 ng/mL. The Python-based machine vision algorithm was developed for this point-of-care CEA detection. Furthermore, for the research of practical application, the designed intelligent biosensing platform exhibited remarkable cut-off value comparing with some common-used commercial LFA test strips.

In addition, for the relevant biomarker of α-Syn protein for emerging neurodegenerative diseases (NDDs), a PDMS-based hydrophobic biochip was designed and manufactured. Specifically, the AutoCAD software was used to create the PDMS-based biochip's pattern while considering pertinent hydrophobic equations and associated studies. The SERS functionalized biochip was successfully designed and manufactured from the related morphology investigations of various view of SEM images using the PDMS demolding and UV irradiation photoreduction techniques. Moreover, the related optical pictures further demonstrate the great hydrophobic performance for fabricated biochip. In the end, the associated Raman spectra suggest that a well-designed and manufactured point-of-care biochip can be used to differentiate the various α-Syn protein structures, suggesting enormous promise for the detection of NDDs in the future.

List of Publications

1. **Yuan Liu**, Xinyue Lao, Man-Chung Wong, Menglin Song, Huang Lai, Pui Wang, Yingjin Ma, Lihua Li, Mo Yang, Honglin Chen, and Jianhua Hao, Microfluidic chip-assisted upconversion luminescence biosensing platform for point-of-care virus diagnostics, Advanced Healthcare Materials, 2303897 (2024).
2. **Yuan Liu**, Man-Chung Wong, Xinyue Lao, Yifei Zhao, Menglin Song, Yingjin Ma, Qianqian Bai, Jianhua Hao, Intelligent point-of-care biosensing platform based on quantum dots luminescence and microfluidic biochip with machine vision algorithm analysis for in vitro tumor marker diagnostics, Biosensors and Bioelectronics, under review.
3. Xinyue Lao, **Yuan Liu**, Lihua Li, Menglin Song, Yingjin Ma, Mo Yang, Guanying Chen, and Jianhua Hao, Plasmon-enhanced FRET biosensor based on Tm^{3+}/Er^{3+} co-doped core-shell upconversion nanoparticles for ultrasensitive virus detection, Aggregate, 5, e448 (2024).

4. Yingjin Ma, Menglin Song, Lihua Li, Xinyue Lao, **Yuan Liu**, Man-chung Wong, Mo Yang, Honglin Chen, and Jianhua Hao, Attomolar-level detection of respiratory virus long-chain oligonucleotides based on FRET biosensor with upconversion nanoparticles and Au-Au dimer, Biosensors and Bioelectronics, 243, 115778 (2024).
5. Menglin Song, Man-Chung Wong, Lihua Li, Feng Guo, **Yuan Liu**, Yingjing Ma, Xinyue Lao, Pui Wang, Honglin Chen, Mo Yang, and Jianhua Hao, Rapid point-of-care detection of SARS-CoV-2 RNA with smartphone-based upconversion luminescence diagnostics, Biosensors and Bioelectronics, 222, 114987 (2023).
6. Lihua Li, Menglin Song, Xinyue Lao, Sin-Yi Pang, **Yuan Liu**, Man-Chung Wong, Yingjin Ma, Mo Yang, and Jianhua Hao, Rapid and ultrasensitive detection of SARS-CoV-2 spike protein based on upconversion luminescence biosensor for COVID-19 point-of-care diagnostics, Materials & Design, 223, 111263 (2022).

Acknowledgments

First and foremost, I would like to express my sincere gratitude to my supervisor, Prof. Jianhua Hao, for his inestimable suggestions and support during my Ph.D. study. His passion and encyclopedic perception for scientific research has always inspired me throughout my whole research time. And I profoundly appreciate his unselfish support and help for me both in academic study and future development.

I would like to extend my appreciation for all the groupmates and collaborators, Ms. Xinyue Lao, Dr. Man-Chung Wong, Dr. Menglin Song, Ms. Yingjin Ma, Mr. Yifei Zhao, Dr. Qianqian Bai, Dr. Lihua Li, Dr. Yi Wei, Dr. Xiao Han, Dr. Feng Guo, Ms. Io Weng-Fu, Dr. Jianfeng Mao, Ms. Fumei Yang, Ms. Yuqian Zhao, Dr. Ran Ding, Dr. Zehan Wu, Ms. Zhaoying Dang, and Dr. Sin-Yi. Pang for their unwavering support, suggestions, and encouragement during my Ph.D. study. Moreover, I would also convey my gratitude to my friends, Ms. Xinyue Lao, Mr. Duanzijing Liu, Mr. Yiping Xiao, Ms. Lu Li, and Mr. Meizhao Han for the friendship and happy times.

I also would like to thank all the academic and technical staff at the Applied Physics (AP) and University Research Facility in Materials Characterization and Device Fabrication (UMF) of the Hong Kong Polytechnic University, who help my study of professional knowledge and experimental research skills.

Finally, I would like to express my gratitude to my family with their endless love, understanding, and encouragement throughout my life.

Table of Contents

List of Figures

Chapter 1 Introduction

1.1 Health threatening diseases and biomarkers

With the development of society, these health-related diseases have always drawn a great attention for common people and scientific researchers all over the world. Among these threatened diseases, virus induced diseases, cancer, and neurodegenerative diseases are three of significant concerned diseases recent years [1-3]. Detecting the corresponding biomarkers of these momentous diseases possesses great importance for health monitoring and timely disease therapy.

The virus is determined as a submicroscopic infectious agent, which can only survive in the living objectives and can infect all the life bodies involving animals, plants, and even bacteria [4]. The tobacco mosaic virus is considered as the first founded virus from two scientists, Adolf Mayer from Germany and Dmitri Ivanovsky from Russia in 1886 and 1992, respectively [5]. Besides, some other significant viruses involving Ebola, influenza, and HPV are also vital for threatening human life. The soluble glycoprotein is regard as a significant diagnostic biomarker for Ebola virus detection [6]. The influenza virus is a very prevalent virus, in which the hemagglutinin and neuraminidase are important detection biomarkers [7]. As a momentous virus for women, the HPV virus seriously impact the health and life, which the HPV L1 capsid protein is one of the crucial biomarkers for timely HPV detection.

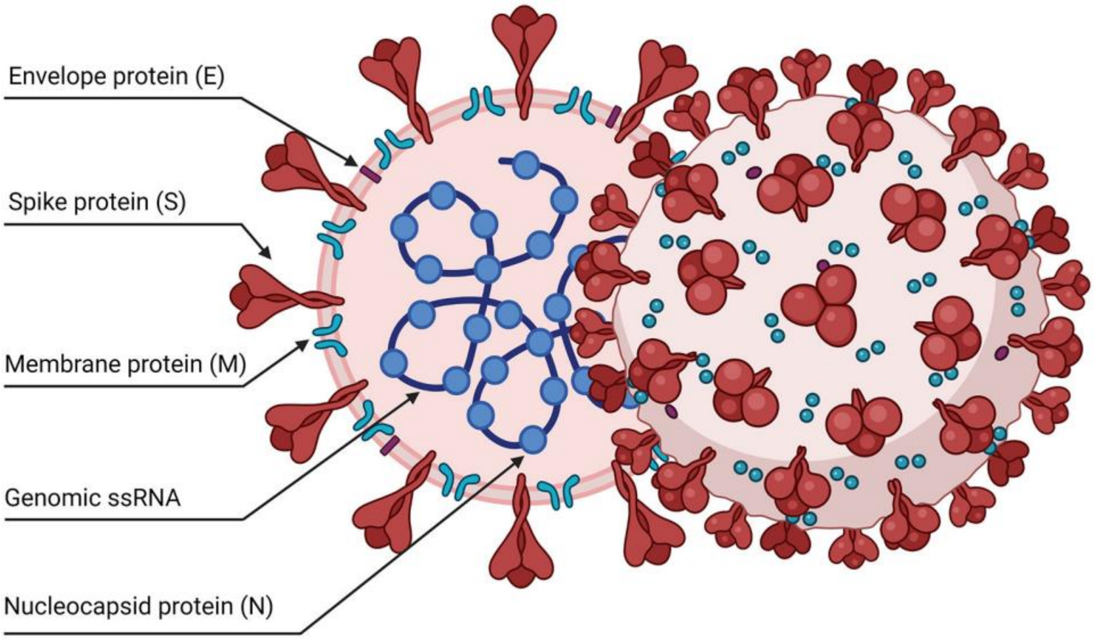

Figure 1. The schematic illustration of representative SARS-Cov-2 viral particle [8].

The COVID-19 epidemic with SARS-Cov-2 virus is one of the most concerned viruses induced disease in recent years [9, 10]. As shown in Figure 1, it illustrates the related structure of SARS-CoV-2 virus, which involves envelope protein, spike protein, membrane protein, genomic ssRNA, and nucleocapsid protein. besides, according to relevant research, the SARS-CoV-2 is a single-stranded RNA virus with a size of 60-140 nm and the related length of spike protein is around 9-12 nm [11].

Moreover, as a hard-to-cure disease worldwide, the cancer is a momentous disease threatening the health and life for human beings. Among these significant cancer diseases, the lung cancer and pancreatic cancer are considered as two of the most important cancers, in which the lung cancer is the major cause of death, and the pancreatic cancer is named as the king of carcinoma implying extremely difficult for therapy [12, 13]. Meanwhile, the relevant diagnostic biomarkers are significant for timely monitoring of these unexpected cancer diseases. According to the related studies, the biomarkers of CYFRA21-1, CA125, and SCC-Ag are often utilized for lung cancer detection [14]. The CA 19-9 biomarker is usually employed for pancreatic cancer diagnosis [15]. And some common cancer related biomarkers, like CEA and AFP are also usually used for general cancer scattering in clinical area.

In addition, with the intensification of the aging society, the neurodegenerative diseases are the emerging diseases, which affects the health of elderly people. Parkinson’s disease and Alzheimer’s disease are two of significant neurodegenerative diseases. The relevant biomarker for Parkinson’s disease involves Alpha-Synuclein, Leucine-Rich Repeat Kinase 2, Tau Protein, and et. al [16-18]. In terms of the Alzheimer’s disease, the Aβ42/Aβ40, Phosphorylated Tau, Neurofilament Light Chain, and et. al. are considered as the corresponding biomarkers for neurodegenerative diseases evaluation [19-21]. Therefore, realizing the detection of related biomarkers of disease possesses significant importance for timely screening and diagnosis of human health and life.

1.2 Commercial detection methods

1.2.1 Diagnostic methods of virus

Some traditional commercial techniques including polymerase chain reaction (PCR) and lateral flow assays are usually employed for viruses' biomarkers diagnosis. The PCR, with a high detection sensitivity of around 100 copies/ml, is regard as a gold standard for virus detection [22].

As exhibited in Figure 2, the typical procedures of PCR are illustrated. In details, the first stage involves converting a double-stranded DNA (known as a template) to single strands at high temperatures (a melting process known as denaturation). The temperature is then decreased to allow complementary short oligonucleotides (known as primers) to attach to the single-stranded DNA. The enzyme, a heat-resistant DNA polymerase2 in the mixture, then extends these primers using the template to create a new strand.

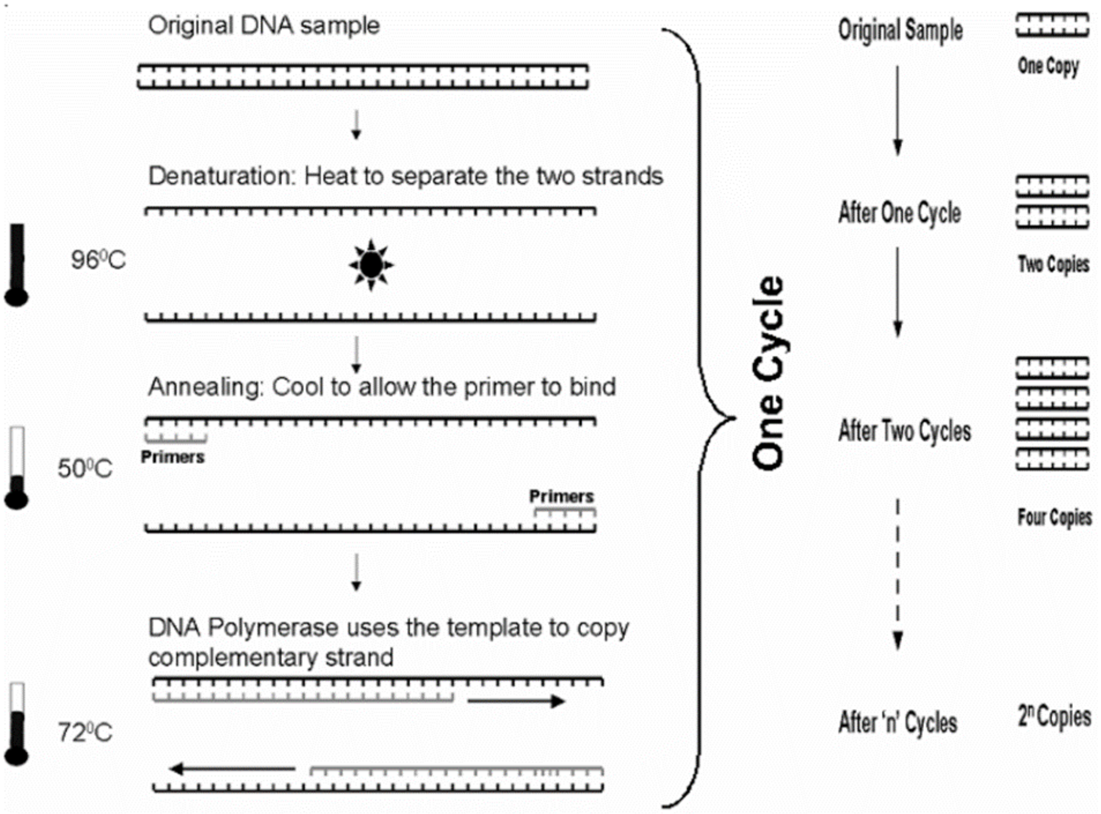

Figure 2. The schematic diagram of typical polymerase chain reaction [23].

After each round of DNA copying, the double-stranded DNA must be melted at high temperatures (~95 °C) in the reaction tube, making heat resistance essential. So, at the end of the first cycle, the number of DNA molecules has doubled. In the second cycle, the DNA is melted again to produce single-stranded DNA, and the cycle repeats until the reaction mixture is depleted. This leads to an exponential growth in the number of copies of the template DNA.

1.2.2 Biosensing approaches of cancer

In terms of the commercial detection methods of cancer, several approaches are employed involving *in-vivo* and *in-vitro* diagnosis. For the in-vivo detection, the radiology techniques such as computed tomography and magnetic resonance imaging scans are frequently employed for in-vivo imaging diagnosis of cancer [24, 25]. These technologies can help doctors get a clearer image of sick parts for suitable therapy selection. On the other hand, tissue biopsy is generally irreplaceable for identifying tumor features, and it is recognized as a gold standard for cancer in-vitro diagnostics [26]. The schematic process for this tissue biopsy method is briefly illustrated in Figure 3, which involves samples acquiring via needle from patient, related tissue sections, histological staining, images observation by optical microscope, and research estimation from experienced pathologists. And the whole detection processes usually spend a few hours to a few days, typically.

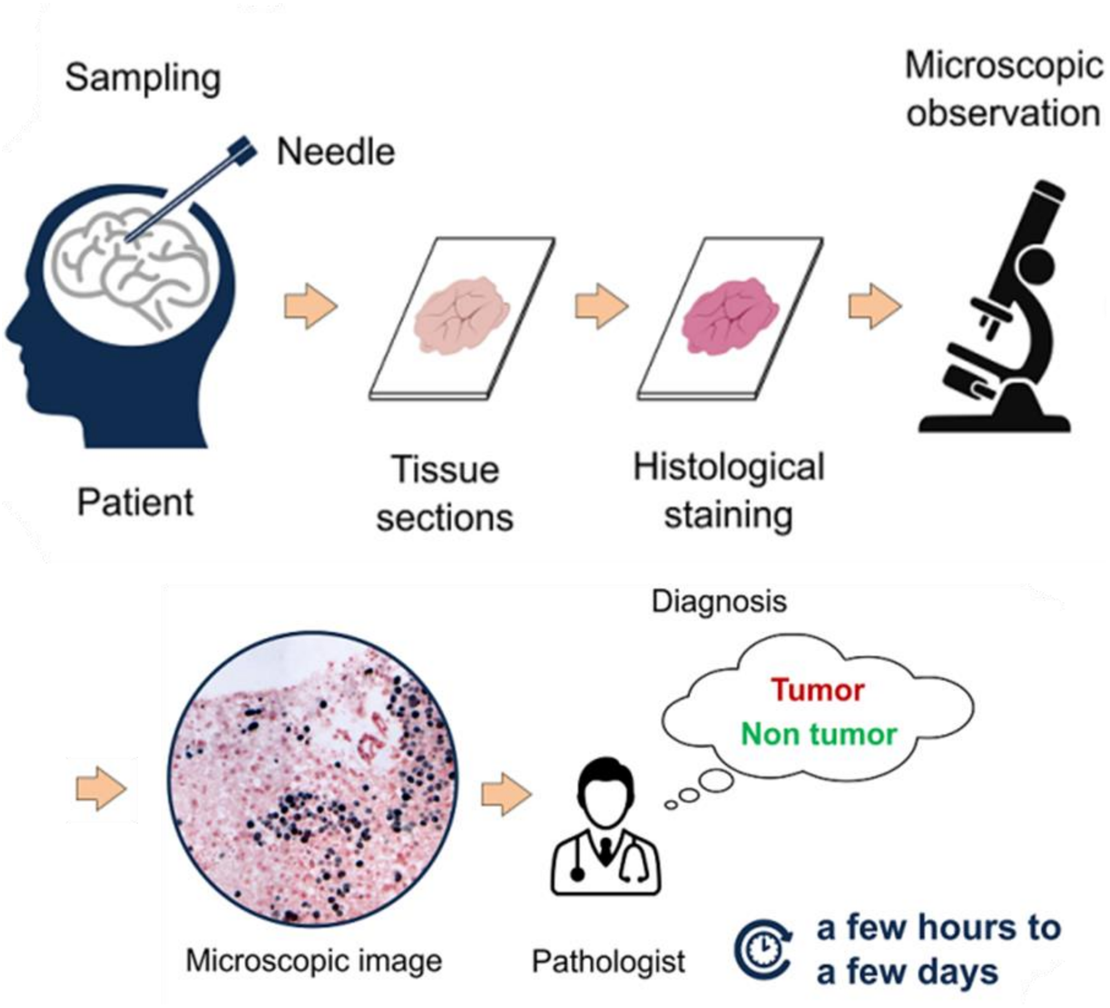

Figure 3. The classical workflow of tissue biopsy for most type of cancer detection [27].

1.2.3 Detection methods of neurodegenerative disease

The relevant commercial detection methods for neurodegenerative diseases are crucial for early monitoring progression and evaluating treatment efficacy of the unexpected neurodegenerative diseases. Up to now, these diagnostic methods involve magnetic resonance imaging, positron emission tomography, cerebrospinal fluid biomarkers detection, genetic testing, and cognitive and functional assessments [28-31]. Moreover, from corresponding studies, the mass spectrometry and enzyme-linked immunosorbent assay detection methods are mainly considered as the gold standard for the neurodegenerative diseases related biomarkers diagnosis [32].

Although these commercial detection methods are mainly employed for the disease-related biomarkers diagnosis in practical. Form these above relevant descriptions of biomarkers diagnostic approaches involving virus, cancer and neurodegenerative diseases, many disadvantages are currently existing including time-consuming, tedious detection procedures, professional diagnostic equipment requirements, specialistic operation staff, which limits the broad application towards masses of the people. As a result, developing and investigation the point-of-care biosensing platform for relevant detection methods of biomarkers possesses great significance.

1.3 Point-of-care biodetection platform

Point-of-care (POC) diagnostics devices are low-cost, user-friendly, quick, and independent of instruments [33]. Small sample volumes of complicated biological and chemical materials can be used to operate an idealized POC device. POC diagnostics can lower medical expenses, incorrect labelling, improper handling, and incorrect analysis direction. Owing to these excellent characteristics, the POC based biosensing platform are extremely appropriate for improving and extending the biomarkers detection applications. In this research area, corresponding researchers have designed and fabricated several POC biosensing platforms for the detection of related biomarkers.

1.3.1 Colorimetric based point-of-care biosensing platform

The mobile phone-based point-of-care biosensing platforms have been increasingly employed in biomedical application involving biomarkers detection [34, 35].

For instance, as shown in Figure 4, a POC based nucleic acid amplified testing (NAAT) device was developed by Priye et al. It combines a smartphone-based detection system with multiplexed reverse transcription loop-mediated isothermal amplification assay to allow for simultaneous investigation of several biomarkers without any cross-reactivity with other flaviviruses or alphaviruses [36]. Their proprietary detection technology, when combined with smartphone picture analysis, allows for detection that is on par with benchtop NAAT equipment in terms of performance. A colorimetric detection algorithm was also devised by them for the analysis of photos taken with smartphones' CMOS sensors.

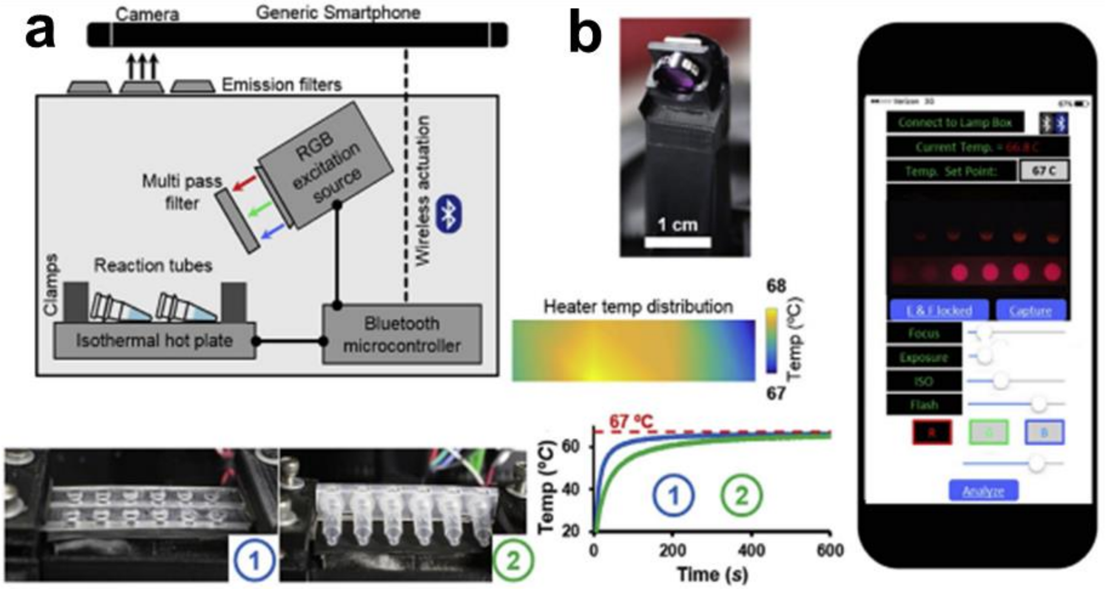

Figure 4. The colorimetric based biosensing platform for Zika virus detection (a) The diagnostic setup of point-of-care RT-LAMP assay (b) The equipped LED with different filters and related smartphone app [37].

The red (R), green (G), and blue (B) light are passed to specific pixels by the CMOS sensors in conjunction with a Bayer filter. This kind of RGB sensor is employed to reproduce images on the device's display in an effective manner. The point-of-care biosensing platform's potential for extensive clinical use is demonstrated by its use in the direct detection of Zika virus from unprocessed human materials, such as blood, urine, and saliva.

1.3.2 Fluorescence based point-of-care biosensing platform

The point-of-care biosensing platform based on fluorescence has been always utilized for biomarkers detection area because of the advantages such as, non-invasiveness diagnosis, easy to operation, and availability of many fluorescence nanoparticles [38]. For example, Algar and coworkers designed and developed a point-of-care platform consisting of quantum dots photoluminescence and smartphone based biodetection with performance of quantitative, multiplexed, and rapid [39]. The fluorescent dye-labeled peptides were coupled with CdSeS/ZnS quantum dots, which emitted red, green, and blue (RGB) light. And any of the related changes in the RGB channel intensities in digital color images were indicative of differences in quantum dots photoluminescence.

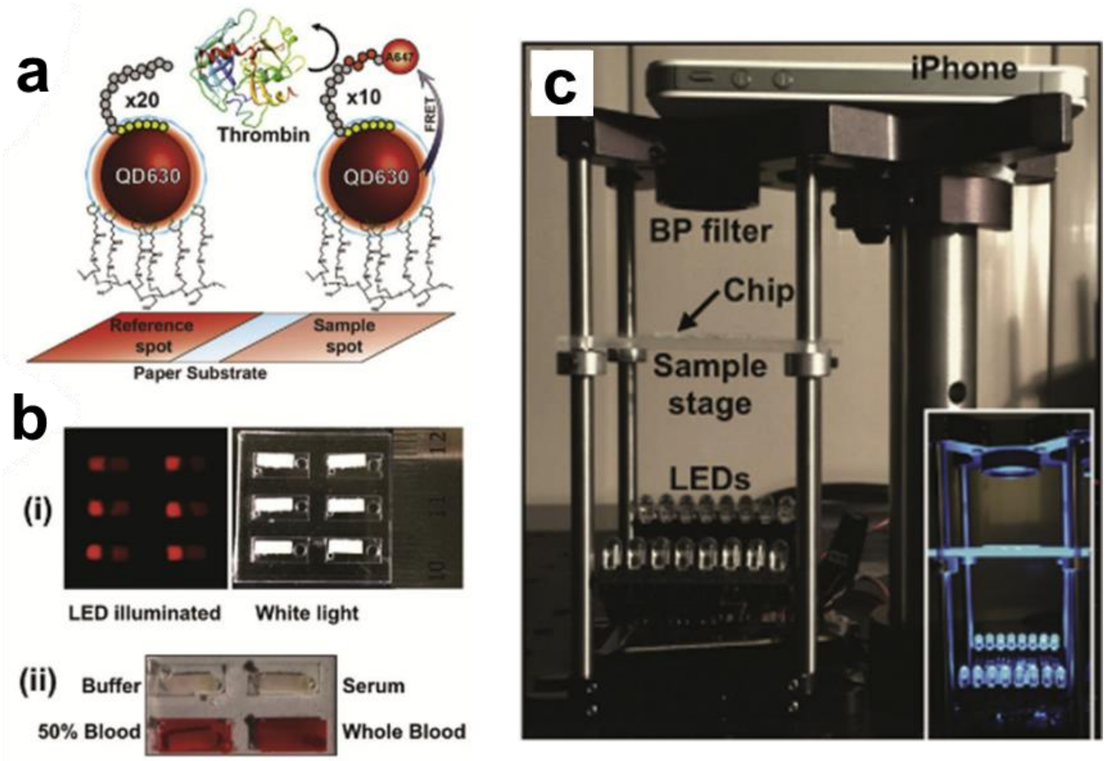

Figure 5. Fluorescence based point-of-care biosensing for virus diagnosis. (a) The paper strips design based on FRET method. (b) Optical photos of paper test strips. (c) Point-of-care device based on smartphone for test results obtain [37].

1.3.3 Surface plasmon resonance biosensing platform

The related point-of-care biosensing platform based on surface plasmon resonance (SPR) has promised potential for biomarkers detection application, in which the corresponding advantages involves great sensitivity, non-destructive, label-free assays for every molecule interaction. A fiber optic SPR biosensor was created by Liu and coworkers for smartphone platforms [40]. The light from the phone's LED flash illuminates the measurement, control, and reference channels, and the camera phone detects light coming from the lead-out's end faces. This phone-based SPR technology is used to reliably and accurately detect various antibody concentrations that are linked to a sensing element that has been functionalized.

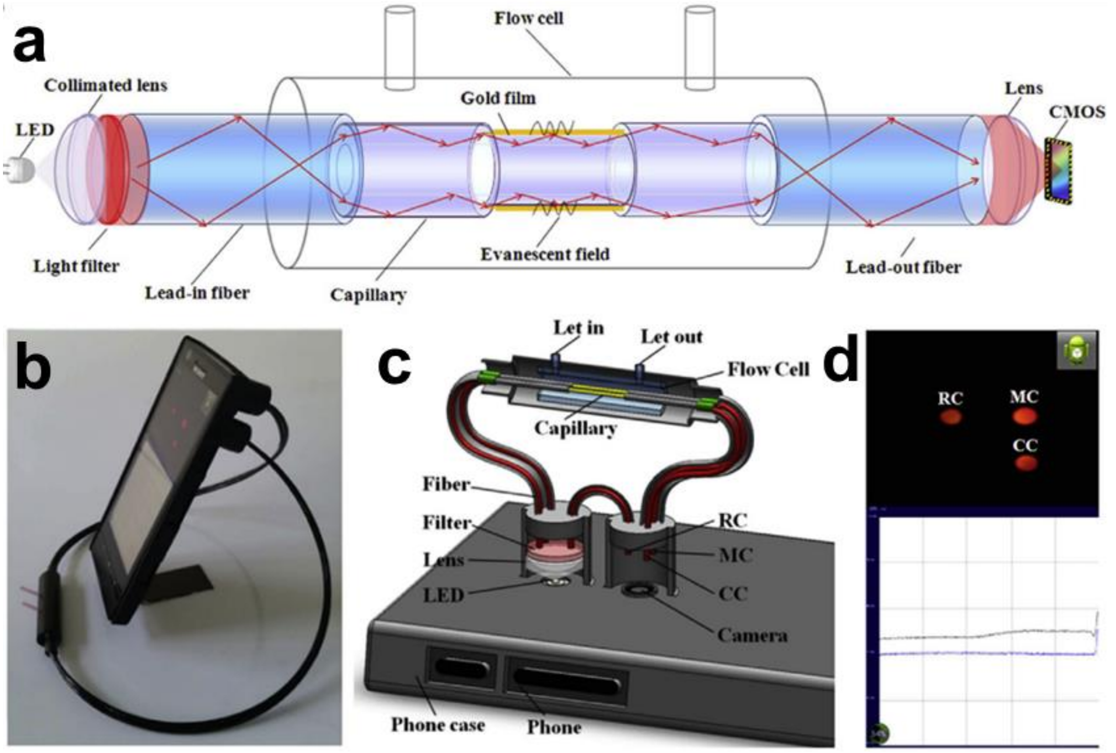

Figure 6. Surface plasmon resonance based biosensing platform for antibody detection. (a) Schematic diagram of the point-of-care biosensing platform. (b) SPR optical sensor combined with smartphone. (c) Schematic illustration of internal structure. (d) The relevant biosensing images [37].

1.4 Photoluminescent nanoparticles

Generally, the photoluminescent nanoparticles are nanosized particles, typically ranging from 1 to 100 nanometers, in which the photoluminescence refers to the luminescent emission under the excitation of photons. These nanoparticles have unique optical properties, which make them great valuable for biomarkers-related detection applications. Normally, these photoluminescent nanoparticles can be divided into two categories, namely upconversion (UC) nanoparticles and downconversion (DC) nanoparticles from the different types of photon energy conversion. As shown in Figure 7, it illustrates the corresponding luminescent elements in the periodic table, which mainly consists of lanthanide elements and some transition metal elements.

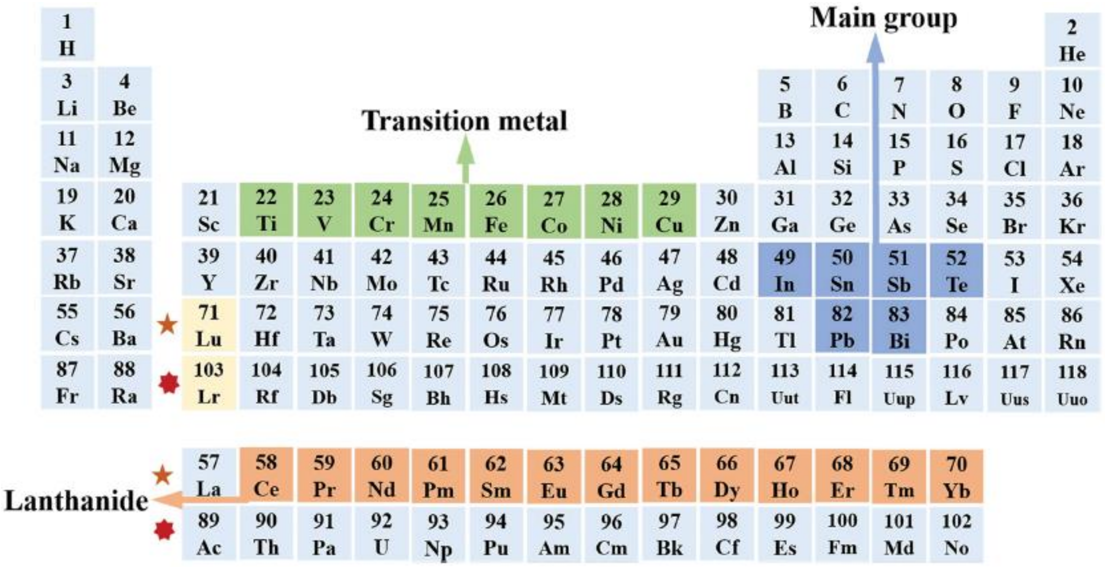

Figure 7. The related luminescent doping elements in periodic table [41].

1.4.1 Upconversion luminescent nanoparticles

The lanthanide dopant ions are incorporated in the host lattice and the UC nanoparticles are typically composed of an inorganic host as shown in Figure 8a. Theoretically, most lanthanide ions should produce UC emission, but only Er^{3+}, Tm^{3+}, and Ho^{3+} can produce visible optical emissions at low pump power densities. These dopants were chosen because of their well-spaced energy levels, which help with the energy transfer and photon absorption processes involved in UC processes. Yb^{3+} with a greater absorption cross section in the NIR spectral region is often doped as a sensitiser in conjunction with the activators to improve UC efficiency. The activator's doping level in a sensitizer-activator system should be kept below 2 mol% in order to reduce the excitation energy lost during the cross-relaxation process [42].

As shown in Figure 8b, the major mechanism of UC processes is the ladder-like configuration of lanthanide dopant ion energy levels. The crystal structure and optical properties of the host materials are crucial and need to be carefully considered in order to realize efficient UC processes. Via lattice vibrations, the host materials may absorb the excited energy of the dopant ions [43]. The optical characteristics of the nanoparticles vary due to changes in the crystal field surrounding the dopant ions caused by variations in the crystal structure of the host materials [44]. Low phonon energy, a high optical damage threshold, and sufficient transparency within the wavelength range of interest are desirable properties for host materials. To achieve high doping levels, the host materials also need to have close lattice matching to the dopant ions. In this sense, appropriate host materials for lanthanide dopant ions include inorganic complexes including rare earth ions, alkaline earth ions, and various transition metal ions [45-47]. Several methods can be utilized for the synthesis of UC nanoparticles, and it is significant that the strong crystal fields surrounding dopant ions are created by nanoparticles with well-crystallized structures, which also reduce the energy loss caused by crystal defects in the dopant ions. Moreover, to integrate with biological molecules and macromolecules, nanoparticles used in biological applications must likewise have a small particle size and high dispersity.

In the situation of overlapping emission spectra, as shown in Figure 8c, lanthanide ions usually exhibit a distinct set of strong emission peaks, which allows for the identification of different spectroscopic fingerprints for correct emission spectrum interpretation. Intra-configurational $4f^n$ electron transitions are the main source of lanthanide ion absorption and emission spectra. The fully occupied $5s^2$ and $5p^6$ sub-shells operate as a shield, minimizing interactions between the 4f electrons and the host lattice. Therefore, the physical or chemical makeup of the host materials has little bearing on the emission peak wavelength of UC nanoparticles. In addition, as shown in Figure 8d, the host/dopant combinations and dopant concentrations are controlled to alter the emission wavelength or the relative emission intensities, which in turn affects the emission colors [48, 49].

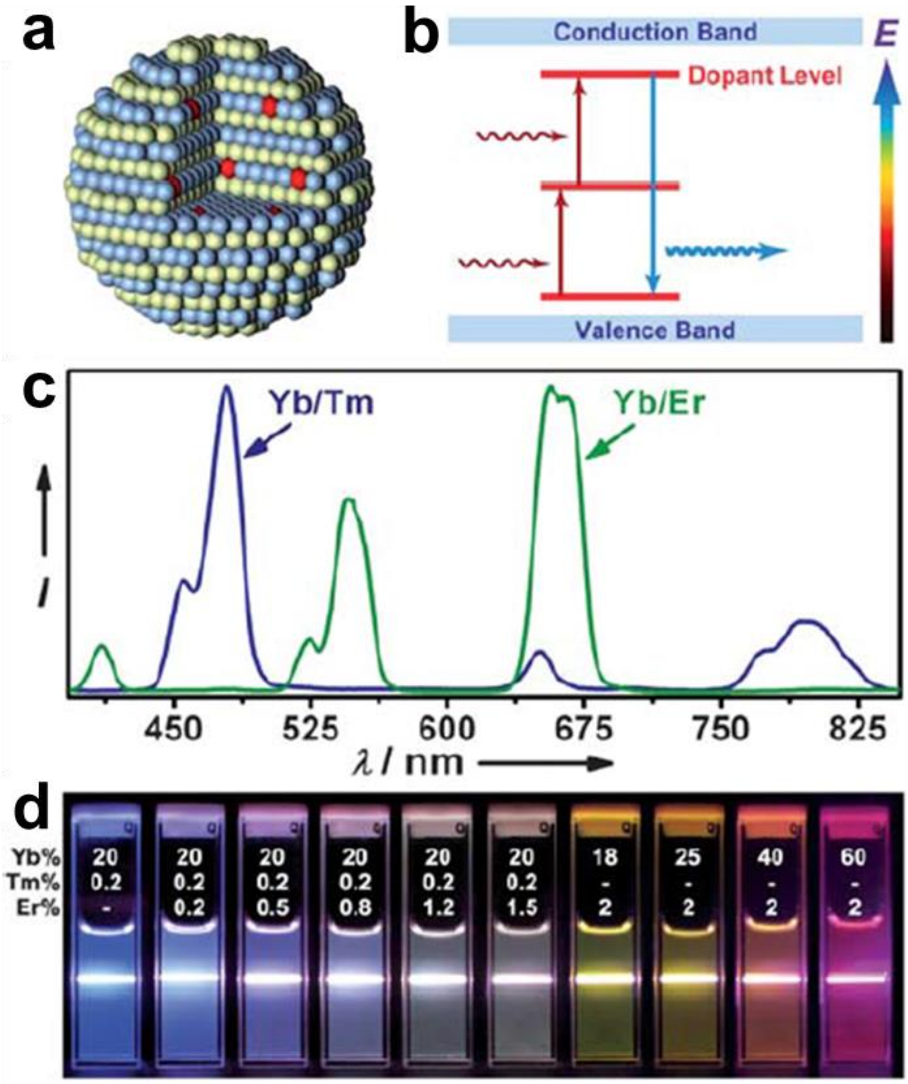

Figure 8. The crystal structure and involved optical performance of UC luminescent nanoparticles. (a) Schematic diagram of lanthanide ions doped nanoparticles. (b) Schematic illustration of energy levels for UC luminescence. (c) Typical emission spectra of UC luminescent nanoparticles. (d) The optical pictures of luminescence tuning for UC luminescent nanoparticles [50].

1.4.2 Downconversion luminescent nanoparticles

On the other hand, the DC nanoparticles are a class of luminescent nanoparticles that convert high-energy photons into lower energy, also known as the Stokes shift process. The quantum dots (QDs) are nanocrystalline semiconductors with excellent luminescent performance as shown in Figure 9. Specifically, the QDs offer a new kind of nanomaterial with distinctive optical and electrical properties. The particle sizes of 1–10 nm, close to or less than the exciton of the Bohr radius, with significant quantum effects [51]. The remarkable optical properties involve long fluorescence lifetime, tunable emission wavelength, wide and successive excitation bands, high absorptivity, narrow and symmetric emission, and good photostability with low susceptibilities to photo-bleaching [52-54]. Owing to these characteristics, they are fluorescent probes that have unmatched benefits over conventional organic dyes [55]. In that case, DC nanoparticles of QDs have been used extensively as fluorescent probes in the biomedical sector in recent years.

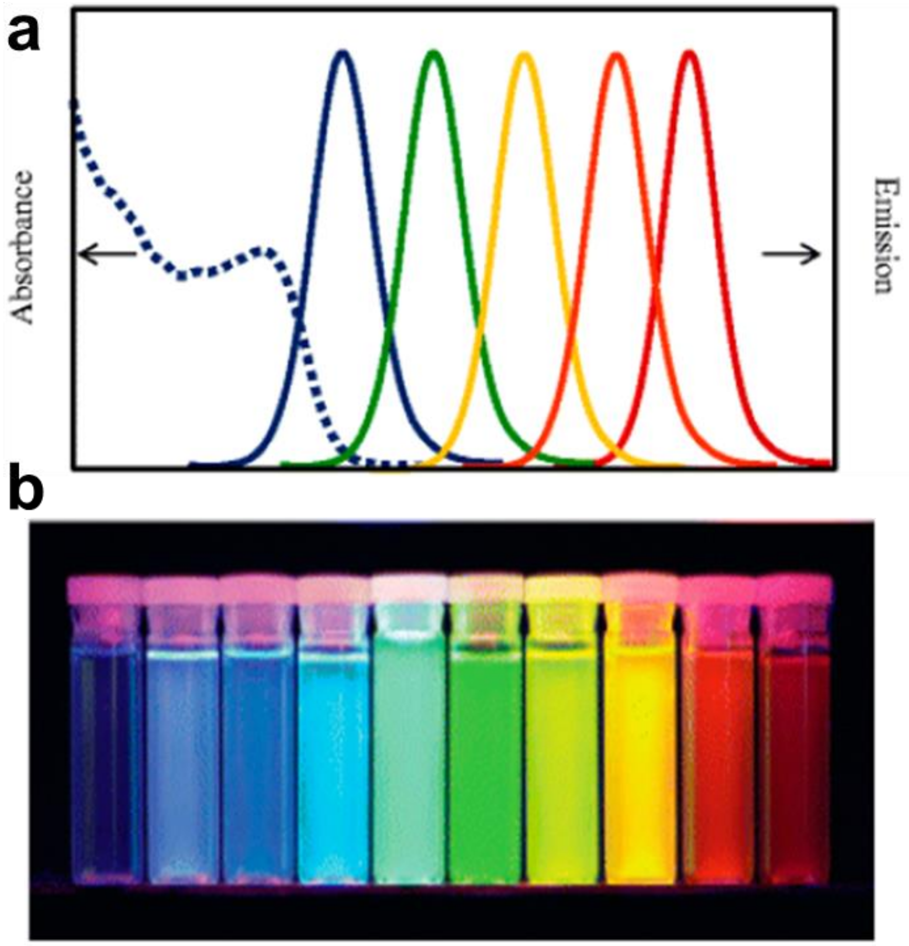

Figure 9. The emission spectra and tuned luminescence of downconversion luminescent nanoparticles. (a) The emission spectra of different size QDs. (b) Tuning emission colors for downconversion luminescent QDs nanoparticles [56].

1.5 Microfluidic biochip

1.5.1 Brief introduction

The microfluidic biochip, also known as a lab-on-a-chip, is a miniaturized device that integrates multiple laboratory functions onto a single chip. These devices manipulate small volumes of fluids through microchannels and chambers, enabling various biochemical and biological analyses. In terms of a microfluidic biochip system, these involved components including designed and fabricated microchannels, pumps and valves for controlling flow of fluids, and integrated sensors or detectors. Owning to these interesting abilities, the microfluidic biochip is widely used for many applications especially for biosensing area.

1.5.2 Fabrication methods

Manufacturing the microfluidic biochip involves creating intricate microchannels, chambers, and other structures on a small scale. And various methods are used for fabricating the microfluidic biochip. The photolithography is a typical manufactured method for microfluidic biochip fabrication [57]. The main processes involve: the photoresist is applied to a substrate like silicon or glass; The photoresist is exposed to UV light through a photomask that defines the desired pattern; The exposed areas of the photoresist are developed, leaving behind a patterned resist that can be used as a mask for etching or deposition. Soft lithography is another important fabrication technique for microfluidic biochip [58]. For the manufacturing procedures, a master mold is created using photolithography or other methods. Nest, the PDMS or another elastomer is poured over the master mold and cured. Finally, the cured PDMS is peeled off, creating a replica of the mold with microchannels. In addition, recent years, the 3D printing is an emerging method for microfluidic biochip fabrication, in which the 3D printer builds the microfluidic device layer by layer from a digital design file [59]. This method can be employed for the rapid prototyping and custom microfluidic devices, which possess advantages of design flexibility and ability to create complex geometries.

1.5.3 Properties and applications

Due to these developed fabrication approaches and continuous investigations, the microfluidic biochip reveals various superiorities involving, miniaturization, high throughput, precise controlling, integration, timely, cost-effectiveness, and biocompatibility. Furthermore, the well-designed and fabricated microfluidic biochip possesses broad application, such as medical diagnostics, genomics and proteomics, cell biology, drug development and screening, environmental monitoring, food safety, and chemical analysis [60]. As shown in Figure 10, researchers from McGill University in Cannada designed and fabricated an elaborate programmed microfluidic biochip for SARS-CoV-2 related biomarker detection [61].

Therefore, considering these thrilling advantages, the combining of MFC for biomarker detection possesses great significance for developing the point-of-care biosensing platform.

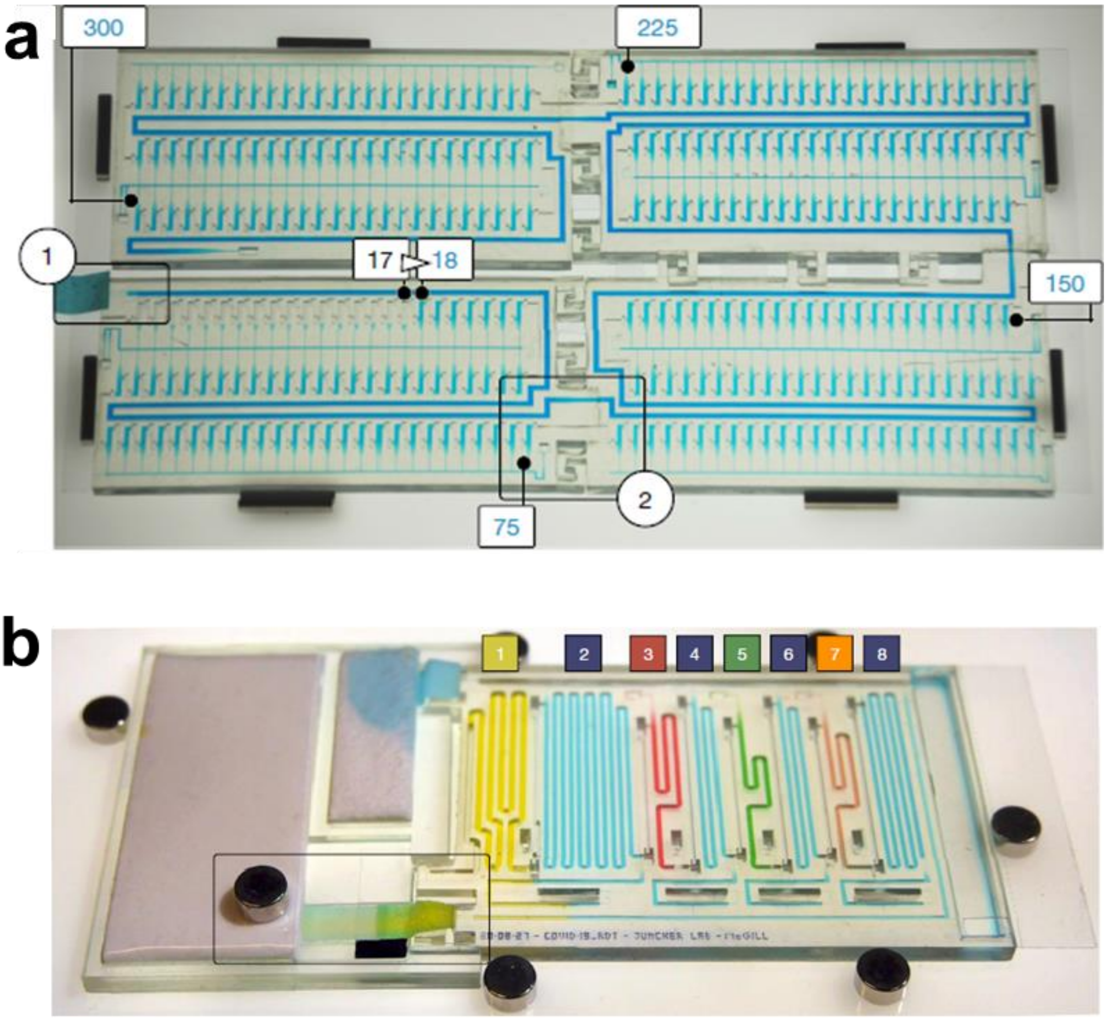

Figure 10. The large-scale microfluidic biochip for SARS-Cov-2 detection. (a) Optical images for four chained and connected microfluidic biochip. (b) The assembled microfluidic biochip with various color solutions filling [61].

1.6 Significance of research

Although the current commercial biosensing method are intensively employed for related biomarkers detection. The appearing problems involving time-consuming, complicated procedures, professional instruments, and specialistic operation personnel have to be considered and settled urgently. Recent years, some point-of-care biosensing platforms have attracted remarkable attention of relevant researcher worldwide owing to their excellent advantages including easy-to-use, portable, economical and practical, and intelligent. Among these point-of-care biosensing platforms, the luminescence-based platforms possess various advantages and arouse great interest. Moreover, the microfluidic biochips are widely employed for the biomedical applications, but the related system is relatively tedious and complex, which restrict its practical application. Therefore, combining and balancing their advantages to develop the point-of-care biosensing platform possesses great significance for investigation the next generation biodetection approaches of diseases-related biomarkers.

1.7 Overview of thesis

The corresponding chapters of this thesis are organized as follows:

Chapter 1: Introduction. This chapter introduces the related biomarkers of three common diseases threatened human health, the commercial detection methods for relevant biomarkers, the importance of point-of-care biosensing platforms and current research works, corresponding concepts and significance of photoluminescent and microfluidic biochips, and the involved objectives for present work.

Chapter 2: Experimental techniques. In this chapter, the preparation methods of utilized photoluminescent nanoparticles and manufacturing approaches of employed microfluidic biochips are introduced. Moreover, the related characterizations are also described in this chapter.

Chapter 3: Microfluidic biochip assisted upconversion luminescent platform for N-protein biomarker *in-vitro* detection. To better realize the portable and sensitive virus detection, in this chapter, we propose a point-of-care biosensing platform involving microfluidic biochip assisted and upconversion luminescence. The related characterizations including morphology and optical properties of nanoparticles, separating and concentrating performance of biochip, biodetection abilities, and biosensing comparation with commercial test strips indicate that this well-designed point-of-care biosensing platform possesses great potential for the future virus detection application.

Chapter 4: Point-of-care biodetection platform based on QDs and biochip for CEA biomarker diagnosis. In this chapter, we introduce a point-of-care biodetection platform for cancer related biomarker diagnosis. The corresponding investigations involving morphology and luminescent performance of nanoparticles, detection sensitivity, machine version algorithm, and biosensing platform illustration demonstrate that the developed biodetection platform can be utilized for the prospective biomarker detection.

Chapter 5: Hydrophobic SERS biochip based biosensing platform for α-syn protein biomarker detection. With the emerging of neurodegenerative disease, we design and fabricate a hydrophobic SERS biochip for the related biomarker evaluation in this chapter. The biochip patterns are designed and studied concerning relevant theory and research. The successfully manufactured biochip can be employed for distinguishing the different structure of corresponding biomarker via Raman spectra, implying a great potential application for neurodegenerative disease related biomarker evaluation.

Chapter 6: Conclusions and future work suggestions. This chapter summarizes these research works from chapter 3 to 5 and gives some suggestions for prospective works.

Chapter 2 Experimental techniques

2.1 Preparation method of photoluminescent nanoparticles

The coprecipitation method is much commonly used for the synthesizing of uniform photoluminescent nanoparticles, especially for the relevant upconversion nanoparticles preparation. The coprecipitation is nanomaterials synthesizing method, in which the several involved chemicals are precipitated simultaneously in solvent. When the solution is supersaturated, the coprecipitation usually occurs and resulting in the particles formation, enlargement, and clustering. The nucleation process is the significant process for coprecipitation method, which implies the initiation of particle generation. After that, the secondary processes like Ostwald ripening and aggregation start to work. For the secondary processes, it plays an impotent role in the size shaping and particles characteristics. The reaction circumstances involving reactants addition rate and stirring intensity take effect for the distribution, shape, and sized of prepared nanoparticles. Due to these advantages consisting of cost-effectiveness for reaction equipment, conventional procedures, and rapid reaction time, the coprecipitation method can be well appropriate for the related preparation of photoluminescent nanoparticles in our research works.

2.2 Fabrication approaches of microfluidic biochip

The microfluidic chips were fabricated by the conventional soft lithography and reverse molding procedures. In details, the manufacture processes were illustrated as follows: At first, the wafer mold was fabricated by the photolithography method. The designed pattern was drawn through the AutoCAD software and then manufactured to film Mask. For the specific wafer mold photolithography process, the 4-inch wafer was cleaned via acetone, IPA, DI Water, and N_2 gas. The SU-8 photoresist around 4 ml was next spun coating onto the surface of the wafer with no bubble. Then the photoresist coated wafer was treated for soft bake under 65 & 95 degrees Celsius and follow by pattern transfer via the photoetching machine. Subsequently, the post bake was carried out with 65 & 95 degrees Celsius and the baked wafer was executed for developing with SU-8 developer, IPA, DI Water, and N_2 gas. After the final hard bake for 150 degrees Celsius, the wafer was cooling down to room temperature for the later processes. The PDMS-glass MFC was fabricated via the followed steps: the obtained wafer mold under lithography was evaporated with a thin organic film for better demolding, and follow by the PDMS pouring and thermocuring with the ratio of 1:10 for the curing agent and base. Next, the cured PDMS with designed pattern was implemented with demolding and clipping for the following plasma treatment. And the plasma treated PDMS chips and glasses were bonded and heated for 85 degrees Celsius with 5 minutes. Finally, the designed MFC was obtained after the channels cleaning by gas.

2.3 Characterization methods

2.3.1 X-ray diffraction

The X-ray diffraction (XRD) is a very useful non-destructive technique for the structure properties investigation in a micro or nano scale. This technique provides the related structure analysis including crystal structure, phase orientation, crystal defects, and particle size evaluation. The schematic illustration of X-ray diffractometer fundamental working principle is exhibited in Figure 11, which describes the relevant constructed interference of the incident X-ray induced by lattice planes.

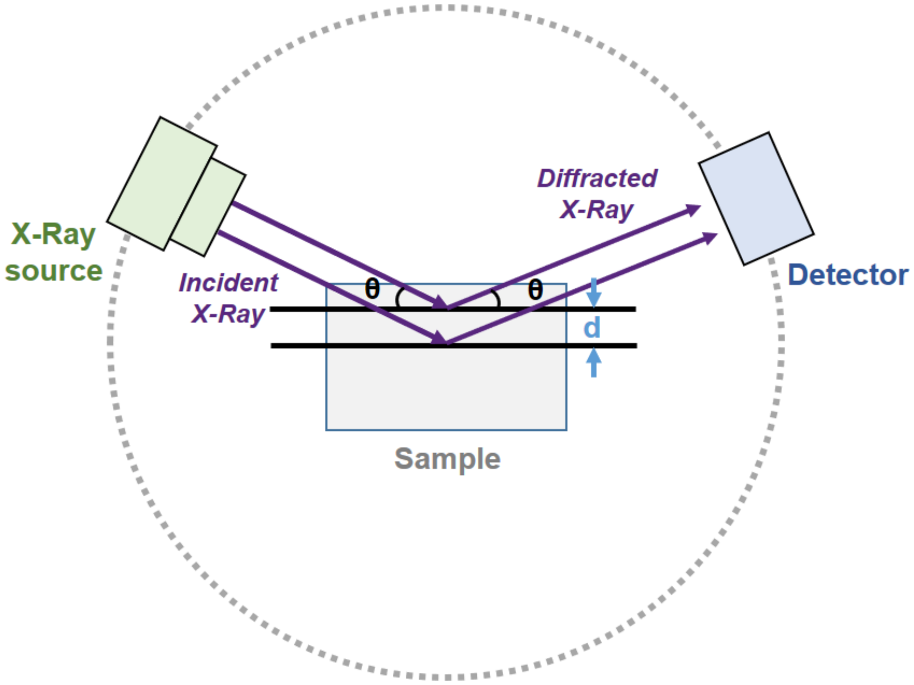

Figure 11. The schematic diagram of X-ray diffractometer with fundamental working principle.

As can be seen, the incident X-ray monochromatic beam is irradiated on the surface of sample with lattice plane spacing “d”. The lattice planes scattered wave of sample will superpose constructively and accord with the Bragg’s law [62]:

$$2\mathrm{d}\sin\theta = n\lambda$$

The scattered X-rays path difference equals to the integral number (n) of the wavelength (λ) in a specific incident angle θ. And after compared with the standard diffraction data base, the information of measurement with crystal structure or phase will be acquired. In our research work, the Rigaku, SmartLab 9kW X-ray diffractometer was utilized for investigation for the crystal structure of samples.

2.3.2 Optical microscopy

The optical microscope is a powerful technology for observation the magnified images of small objects, which is generally consisted of visible light source and a lenses system. The sample can be observed by transparent or reflectance mode of optical microscope for the sample conditions and investigation requirement.

Besides, the corresponding polarized incident light can be used for studying the crystal orientation of materials. In our work, the Leica DM1750 optical microscopy was employed for the morphology study of relevant PS microspheres.

2.3.3 Electron microscopy

Transmission electron microscopy (TEM)

The transmission electron microscopy (TEM) is a type of electron microscopy technique for obtaining an image via the transmitted electronic beams through a sample. Normally, the thickness of TEM sample is less than 100 nm or suspension on a grid holder. The TEM image is formed from the electron interaction as the transmitting of the beam through sample, then the image is magnified and focused on a fluorescent screen for imaging. Due to the smaller de Broglie wavelength, the resolution of TEM is much higher than the light microscopes, which enables the TEM instrument to acquire some fine details even in a single atom scale. This TEM technique is widely used in the scientific field, such as physics, chemistry, and materials science. In our study work, the JEOL JEM-2100F TEM instrument was utilized for the morphology investigation of employed photoluminescent nanoparticles and related lattice space.

Scanning electron microscope (SEM)

The scanning electron microscope (SEM) is a valuable electron microscope, which acquires the sample image via scanning the objectives surface with a focused electronic beam. The electrons interact with the sample atoms and generating the surface morphology information of the investigated sample. In details, the electron beam will be scanned in the raster scan pattern and the electron beam will be combined with the detected signal intensity for producing the SEM image. For most of the SEM technology, the Everhart–Thornley detector, a secondary electron detector, is used to detect the secondary electrons, which is emitted via atoms after the electron beams exciting. For our research work, the Tescan MIRA field emission SEM with relatively high resolution was utilized for morphology investigations of PS microbeads and the conjugation for the photoluminescent nanoparticles.

Energy dispersive X-ray spectroscopy (EDS)

The Energy Dispersive X-ray Spectroscopy (EDS) is a useful technique, which is utilized for the composition of chemicals and elements for a investigated sample. For the detection mechanism of EDS system, it is based on the related interaction between the sample and X-ray simulation source excitation. In details, the incident stimulation strikes on the surface of studied sample, in which the electrons are sitting on the ground state in the discrete energy levels. From the related inner shell, the external stimulation will excite and eject an electron and result in an electron hole. In order to stabilize the atomic structure, the electron with high energy from outer shell tend to fill up the electron hole. And ultimately, the photon is released in X-ray from as these two shell energy difference compensation. It is the related characteristic properties of an element for the X-ray emission position and intensity measurements, which is attributed to the unique individual atomic structure. Besides, the external stimulation source commonly includes high energy X-ray or charged particles focused beam in practical applications.

In our experiments, the EDS was equipped with the transmission electron microscopy (TEM) instruments for the relevant investigations of core-shell structured of photoluminescent nanoparticles.

2.3.4 Photoluminescent spectroscopy

The photoluminescence (PL) spectroscopy a non-contact and destructive method for the measurement of any form materials luminescent performance. As shown in Figure 12, the PL spectrometer consists of Xenon lamp, Xenon flashlamp, NIR photomultiplier (PMT) detector, UV-Vis PMT detector, sample chamber, and external laser holder. The brief mechanism of PL spectroscopy is illustrated as follows: at first, the incident light is irradiated on a sample, and the ground state electrons will jump to a higher energy level via the photon’s energy absorption. Then, the electrons excited by photon in excited states relax to their ground state and illuminate the related emitted photons. By the measurement of emitted photons distribution as a relationship with their wavelength, the steady-state PL spectra will be recorded. By using the fixed excitation wavelength, the emission spectra are acquired for the various emission spectra range.

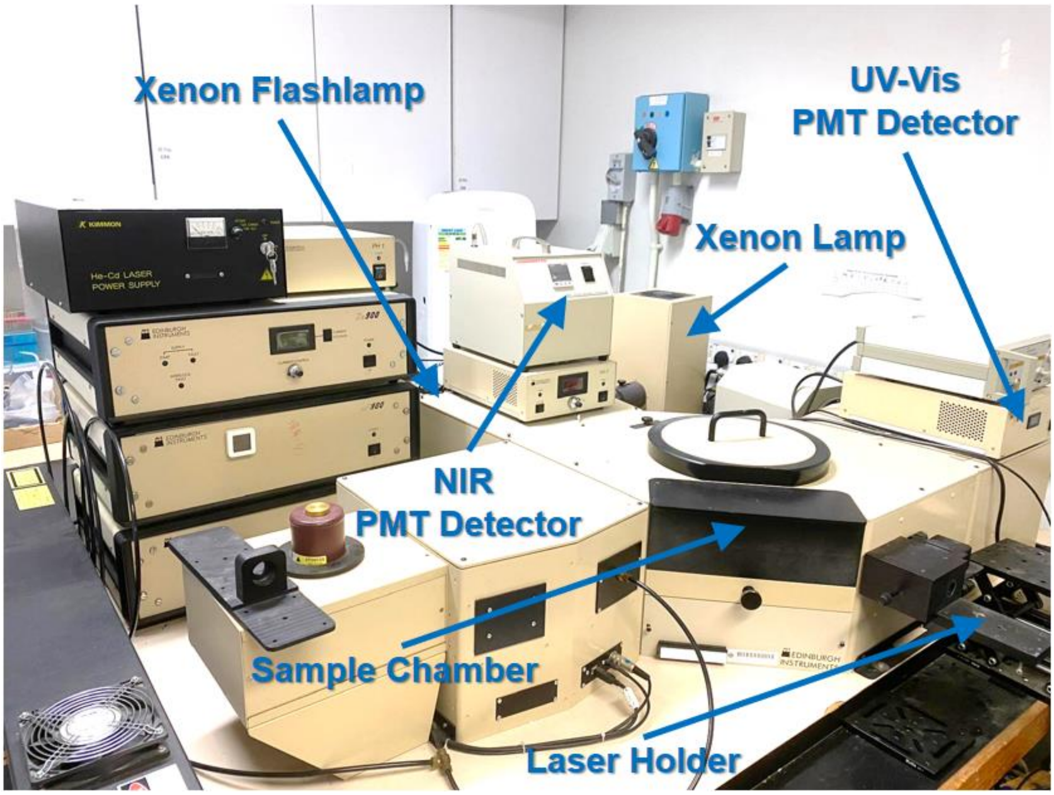

Figure 12. The optical image of PL spectrometer employed in our laboratory.

On the other hand, the excitation spectra are obtained by fixing the emission wavelength for different excitation wavelengths range measuring. The computer-controlled mirrors equipped in the sample chamber enables the rapid excitation and emission paths selection. Besides, the NIR PMT detector is operated at the low temperature of -80 °C with the detection wavelength from 900 to 1700 nm. The UV-Vis PMT detector can measure the wavelength from 200 to 870 nm at the temperature of -20 °C. The pre-equipped Xenon lamp can offer an excitation light from 230 to 1000nm, and the Xenon flashlamp can emit the pulsed incident light at the modified frequency. The external laser can place in the laser holder for the NIR excitation requirement. In our research work, the EDINBURGH FLS900 PL spectrometer was employed for the corresponding photoluminescence investigation of utilized nanoparticles.

2.3.5 Atomic force microscopy

The atomic force microscopy (AFM) is a useful technique for studying the materials performance involving morphology, size, and surface roughness. The AFM system runs by probing the surface of specimen by using a specifically designed tip at the free end of a cantilever. The XYZ scanner allows the probe to scan sample surface with three axis direction. Through the beam deflection technology, the vertical distance between the AFM probe and sample can be well controlled. The laser diode generated beam is focused on the probe tip back and will be reflected to the photodiode, in which its voltage signal is produced from the related amplifier circuit. The processing voltage signal can send to feedback circuit and control the z-axis displacement. The related lateral positions and vertical displacement are transmitted to the computer and follow by the surface information recording of investigated samples. Three common modes of AFM technique are usually employed, which involves tapping mode, contact mode, and non-contact mode. In our relevant experiments, the Asylum MFP 3D Infinity is used to investigate the conjugation conditions of utilized antigen and antibody.

2.3.6 Zeta potential measurement

The zeta potential is defined as the electrical potential of slipping plane, in which this plane is the interface separating the mobile fluid form surfaced attached fluid. Zeta potential resulted from the net electrical charge in the region bounded by slipping plane, which can be widely employed for charge magnitude quantification. Moreover, the zeta potential is usually the only path for investigation the double-layer properties. In our research work, the Malvern Zeta Potential Analyzer was utilized for the relevant modification investigations of prepared samples.

2.3.7 Fourier transform infrared spectroscopy

The Fourier-transform infrared spectroscopy (FTIR) is a beneficial technique for measuring the absorption or emission infrared spectra of sample with solid, liquid, or gas form. For a broad wavelength range, the FTIR instrument can collect and acquire the high-resolution spectral data for materials study. Compared with the typical dispersive spectrometer, the FTIR can measure a wide range of spectra, while the dispersive spectrometer can only detect one narrow wavelength at a time.

Instead of shining a single wavelength beam at the sample, the FTIR technique shine the composited wavelength beam involving several frequencies and measure the absorbed wavelength of the investigated sample. Subsequently, the beam will be modified for obtaining the different frequencies and resulting in a second data point. The measurement process is repeated many times in a very short time. Finally, the computer processes these data points and works backward to deduce each absorption of wavelength. In our study work, the Bruker VERTEX 70, HYPERION 2000 FTIR spectrometer was employed for investigating the corresponding modification conditions of utilized photoluminescent nanoparticles.

2.3.8 UV-Vis absorption spectroscopy

The ultraviolet–visible (UV–Vis) absorption spectroscopy is a powerful technique, which refers to the collection of absorption spectra with the range from full or part of ultraviolet to visible wavelength light. Owing to the advantages of relatively easily implemented and inexpensive, the UV-Vis absorption spectroscopy is commonly employed for various fundamental research applications. And the only requirement is that the absorption wavelength of studied sample is in the UV-Vis range.

Compared with the commercial fluorescence spectroscopy, the UV-Vis absorption spectroscopy is complementary. Apart from the measurement of wavelength, the UV-Vis absorption spectroscopy can also obtain some important parameters, which consists of reflectance (%R), absorbance (A), and transmittance (%T). In our research work, the PERKIN ELMER UV-Vis absorption spectroscopy was used for the related studies including the absorption spectra of PDMS based biochip and investigation of bandgap for prepared photoluminescent nanoparticles.

Chapter 3 Microfluidic biochip assisted upconversion luminescent platform for N-protein biomarker *in-vitro* detection

3.1 Introduction

Throughout history, the human health and medical systems have consistently encountered substantial threats by various viruses. Among these, certain prevalent viruses have left enduring and painful memories for humanity. Smallpox, an infectious disease caused by the smallpox virus, resulted in severe toxemia and led to the deaths of hundreds of millions of individuals centuries ago [63]. The Spanish flu pandemic, primarily attributed to a flu virus akin to the influenza A virus subtype H1N1 (A/H1N1), caused significant distress across Europe [64]. In more recent years, several well-known viruses, including the Ebola virus, Zika virus, severe acute respiratory syndrome coronavirus 2 (SARS-CoV-2), and the Mpox virus, have exerted a profound impact on human society [65-67]. Consequently, the detection of viruses is of paramount importance for the proactive control of viral transmission.

Traditional techniques such as polymerase chain reaction (PCR) and lateral flow assays (LFA) are commonly used for detecting viruses. PCR, which amplifies specific gene segments, boasts an extremely high sensitivity of approximately 100 copies per milliliter, making it a gold-standard approach for virus diagnostics. However, PCR has several disadvantages, including being time-consuming (taking several hours), having high detection costs, requiring skilled operators, and posing a risk of unintended virus spread [68, 69].

Through the development of PCR diagnosis, Chang et al. utilized a non-optical multiplexed PCR method to detect the dengue virus with the fairly high detection sensitivity. However, the assay time still reaches about 90 minutes, which limits the application of rapid diagnosis [70]. LFA is a relatively rapid detection method using the colloidal gold lateral flow bonding to the modified nitrocellulose membrane[71]. Nonetheless, the diagnosis sensitivity of LFA is quite low (around 100 ng/ml), which poses disadvantages in terms of early and accurate virus detection. Jin et al. reported the developed upconversion nanoparticles (UCNPs)- based LFA strips for specific virus and protein detection. However, the diagnosis sensitivity and convenience of this device also need to be improved before it can be widely used [72]. Chang et al. developed a PCR diagnostic method that employs a non-optical multiplexed approach to detect the dengue virus with a relatively high sensitivity. However, the assay duration is approximately 90 minutes, which hinders its use for rapid diagnosis[70]. Lateral flow assay (LFA) is a quicker detection technique that utilizes colloidal gold on a modified nitrocellulose membrane. Despite its speed, LFA has low diagnostic sensitivity, which limits its effectiveness for early and accurate virus detection. Jin et al. introduced LFA strips based on upconversion nanoparticles (UCNPs) for the detection of specific viruses and proteins. However, the sensitivity and usability of this device still require enhancement before it can be widely adopted [72].

To overcome the limitations of conventional diagnostic techniques, many new biosensors have been created for detecting viruses. Chailapakul et al. used a paper-based fluorescent sensor to identify the hepatitis C virus, but the stability of the organic fluorochrome used did not maintain high performance in certain complex conditions [73]. Our team has proposed and developed innovative strategies for highly sensitive virus detection by leveraging fluorescence resonance energy transfer. However, the procedures require specialized equipment and trained personnel, which somewhat restricts their application [74-76]. Thus, it is crucial to achieve virus diagnosis that combines stability, sensitivity, and ease of use for effective virus detection.

The microfluidic biochip (MFC) is a device designed with micro-channels arranged in a specific configuration. These channels facilitate the controlled movement of fluids, allowing them to flow through various paths and connect with the external environment at specific inlets and outlets. This lab-on-a-chip MFC device features programmed functionalities, is compact and intricate, and has biological significance, which enhances its integration and portability [77, 78]. Additionally, MFCs with separation capabilities are commonly utilized in biosensing applications, including particle filtration and cell sorting [79]. By employing MFC technology, it is possible to isolate targeted biomarkers in a sample, significantly improving detection sensitivity without needing amplification methods. The sandwich structure is frequently used to capture targeted biomarkers in optical immunoassays, incorporating a luminescent agent for optical detection [80-83]. Due to the transitions of 4f electrons in the f-f or f-d configurations of lanthanide luminescent ions, upconversion nanoparticles (UCNPs) doped with lanthanide ions demonstrate stable and consistent luminescent performance [84-86]. Established research techniques for modifying UCNPs have greatly broadened their use in biosensing applications [87-89].

Moreover, point-of-care detection is a biosensing technology that operates close to the patient and offers many benefits, garnering significant research attention [90]. For example, a team from Harvard Medical School has developed a compact luminescence-based in vitro diagnostic tool for virus detection. However, the processes of sample purification and separation remain somewhat cumbersome, limiting its practical use in virus diagnosis [91]. Consequently, it is essential to find a balance between the advantages of biosensing technologies and the need for quick, sensitive, and portable virus diagnostic solutions.

3.2 Experimental section

3.2.1 Preparation of $NaYF_4$:Yb/Er UCNPs

The synthesis of NaYF4:Yb/Er was conducted utilizing the conventional coprecipitation technique. In a 50-ml flask, 1.6 ml of 0.2 M Y(CH3COO)3, 0.72 ml of 0.2 M Yb(CH3COO)3, and 0.08 ml of 0.2 M Er(CH3COO)3 were combined with 6 ml of octadecene (ODE) and 4 ml of oleic acid (OA). The resulting solution was gradually heated to 150 °C and maintained at this temperature for 40 minutes while being stirred magnetically. Following this, the reaction mixture was allowed to cool to room temperature, after which a mixture consisting of 1 ml of 1 M NaOH in methanol and 3.3 ml of 0.4 M NH4F in methanol was introduced. The mixture was subsequently heated to 50 °C for 30 minutes to facilitate the evaporation of methanol. Thereafter, the temperature was increased to 100 °C, accompanied by a 10-minute vacuum degassing to remove any residual moisture. The flask was then subjected to heating at 290 °C under an argon atmosphere for a duration of 2 hours before being allowed to cool to room temperature. The resulting upconversion nanoparticles (UCNPs) were precipitated by the addition of 5 ml of ethanol and collected via centrifugation. The UCNPs underwent further purification through three cycles of washing with cyclohexane and ethanol, and were ultimately dispersed in cyclohexane for subsequent applications.

3.2.2 Surface modification of UCNPs

The synthesized upconversion nanoparticles (UCNPs) were precipitated in 15 mL of ethanol with the addition of 112 μL of 2 M hydrochloric acid (HCl). Following a 30-minute incubation period, the UCNPs were collected via centrifugation and subsequently redispersed in 15 mL of ethanol containing 11.2 μL of 2 M HCl, followed by sonication for an additional 30 minutes. The ligand-free UCNPs were then isolated through high-speed centrifugation. Subsequently, 20 mg of polyacrylic acid (PAA) dissolved in 0.2 M sodium hydroxide (NaOH) was introduced to the ligand-free UCNPs and stirred overnight. The resulting UCNP-PAA complex was collected through high-speed centrifugation and dispersed in 1 mL of water for storage purposes.

3.2.3 Conjugation of UCNP-PAA with antibody

The conjugation of antibody with UCNP-PAA was performed utilizing conventional chemical methodologies. Initially, 200 µL of UCNP-PAA underwent buffer exchange in MES buffer at pH 5 (500 µL). Subsequently, 6 mg of NHS and 3 mg of EDC were introduced to the csUCNPs while stirring for a duration of 30 minutes. Following this, 0.1 mg of antibody was incorporated into the mixture and stirred for an additional 2.5 hours to facilitate a complete coupling reaction. The antibody-conjugated UCNP was then isolated through high-speed centrifugation and subjected to three wash cycles with water.

3.2.4 Conjugation of PS microbeads with antibody

At first, 1 mg of carboxy group-modified polystyrene (PS) microbeads was dissolved in 1 mL of 2-(N-morpholino)ethanesulfonic acid (MES) buffer. Subsequently, 10 µL of a 10 mg/mL solution of 1-ethyl-3-(3-dimethylaminopropyl)carbodiimide (EDC) and N-hydroxysuccinimide (NHS) was introduced, and the mixture was incubated at 37 °C for 30 minutes. Following this incubation, the PS microbeads were precipitated and redispersed in phosphate-buffered saline (PBS), to which 0.3 mg of antibody was added in a total volume of 800 µL PBS. This mixture was then incubated at 37 °C for 1 hour.

Upon completion of the reaction, a 5 mg/mL solution of bovine serum albumin (BSA) was incorporated and allowed to incubate for an additional hour. The resulting antibody-conjugated PS microbeads were subsequently washed and resuspended in PBS for future applications.

3.3 Characterization and discussion

3.3.1 Mechanism of designed biosensing platform

The MFC-assisted diagnostic platform was developed and employed for the purpose of point-of-care and portable detection of the nucleocapsid protein (N protein) of SARS-CoV-2, as depicted in Figure 13. As illustrated in Figure 13a, viral samples were collected from patients, airports, and various confined environments, such as elevators and restrooms. The collected swabs, which may or may not contain the N protein, were subsequently combined with prepared diagnostic reagents, including modified upconversion nanoparticles (UCNPs) and polystyrene (PS) microbeads, referred to as PSMBs in Figure 13a. This mixture was incubated for several minutes, resulting in the formation of a sandwich immunoassay comprising UCNPs, the N protein, and PS microbeads. Following this, the incubated mixture was injected into the designed MFC-assisted chamber, which was then placed into a portable detection device for viral diagnosis. The test results can ultimately be transmitted to a mobile phone via Bluetooth, with the entire process being completed within a fifteen-minute timeframe. Detailed schematic diagrams and the operational mechanism of the MFC-assisted chamber are presented in Figures 13b and 13c.

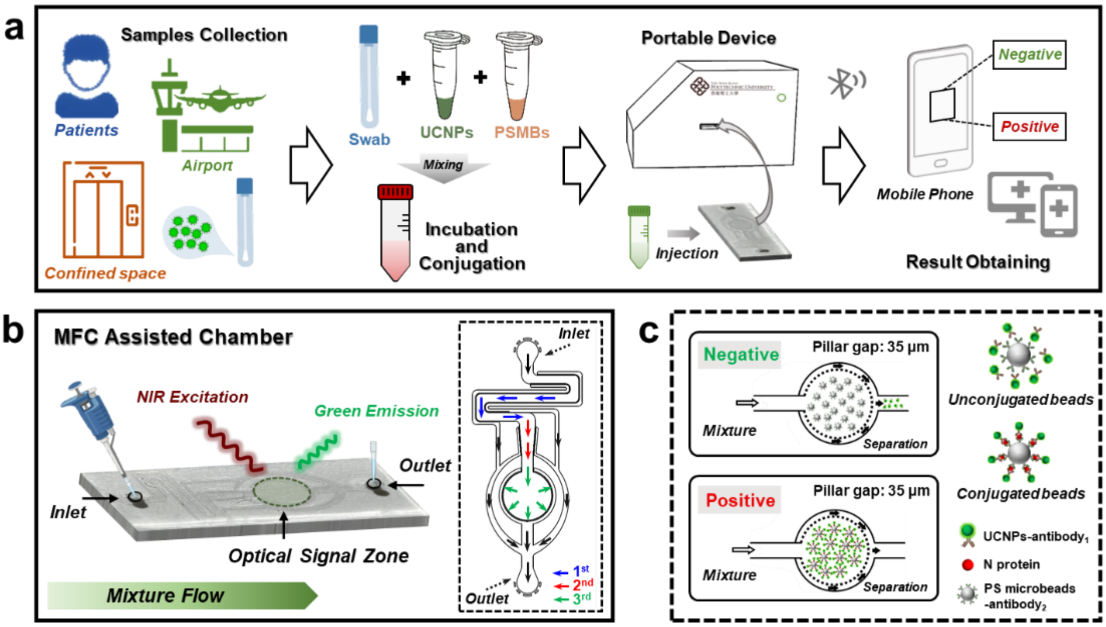

Figure 13. (a) Schematic illustration of biodetection procedures, which includes swabs collection, mixing and incubation for pre-prepared reagents, samples injection, and test result acquiring. (b) The flow of the mixture and the generation of optical signals within the MFC-assisted chamber. (c) The fundamental principle of MFC, which includes separation and concentration functions for detecting viruses (Pillar gap: 35 μm; PS microbeads size: 50 μm).

As depicted in Figure 13b, the incubated mixture was introduced into the biochip's inlet using a pipette, with excess fluid exiting through the outlet. The optical signal zone revealed green emission signals in response to 980 nm near-infrared (NIR) excitation, indicating the presence of the N protein. The accompanying insert on the right illustrates a coordinated three-stage separation system designed for the filtration of unconjugated upconversion nanoparticles (UCNPs) and the concentration of bound sandwich polystyrene (PS) microbeads. Furthermore, Figure 13c elucidates the separation and concentration mechanism employed within the microfluidic chamber. A negative result indicates that the unconjugated beads remain in the filtration zone without exhibiting photoluminescence (PL) signals, whereas a positive result signifies that the conjugated beads display PL signals when subjected to NIR laser excitation. In conclusion, these remarkable properties suggest that this system holds significant potential as a platform for portable virus diagnostics.

3.3.2 Characterizations of related morphology and modification

To investigate the morphology of diagnostic probes, a range of characterization techniques were employed, including transmission electron microscopy (TEM), scanning electron microscopy (SEM), atomic force microscopy (AFM), and zeta potential measurements. As depicted in Figure 14a, the synthesized $NaYF_4:Er^{3+}/Yb^{3+}$ upconversion nanoparticles (UCNPs) exhibited a particle size of approximately 300 nm. The corresponding high-resolution TEM images (Figure 15) and the associated fast Fourier transform (FFT) analysis indicated that the synthesized $NaYF_4:Er^{3+}/Yb^{3+}$ UCNPs possess a well-defined crystalline structure. The relevant Miller indices were calculated and identified as $(\bar{1}1\bar{1})$ and (002), as illustrated in the inset of Figure 14a. Figure 14b presents SEM images of polystyrene (PS) microbeads, both with and without conjugation to N protein.

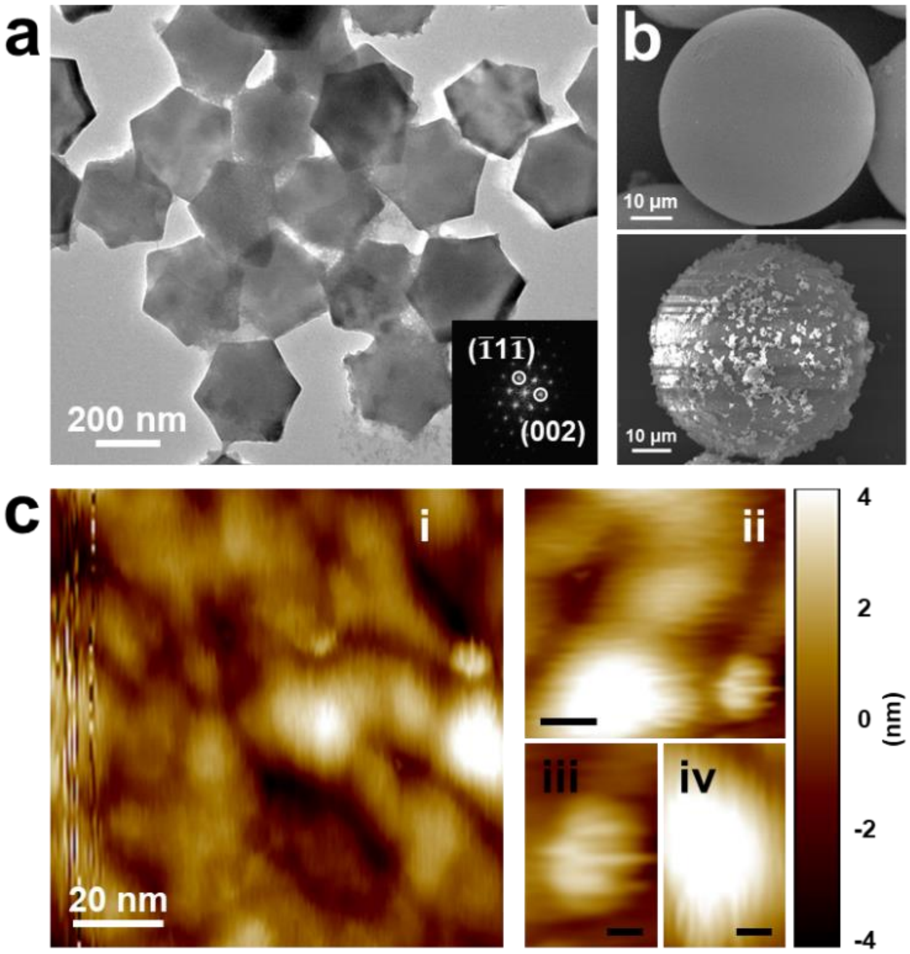

Figure 14. (a) TEM image of $NaYF_4:Er^{3+}/Yb^{3+}$ UCNPs. Related insert presenting the FFT image under the high-resolution TEM. (b) The SEM images of PS microbeads without (top) and with (bottom) N protein. (c) AFM images of the connected antigen and antibody.

The upper portion of Figure 14b illustrates a minimal adherence of upconversion nanoparticles (UCNPs) to the surface of polystyrene (PS) microbeads. In contrast, the lower section of the scanning electron microscopy (SEM) images provides insights into the conjugation dynamics between the PS microbeads and UCNPs. Additionally, due to the significant destructive effects of the electron beam, atomic force microscopy (AFM), which is non-destructive and suitable for biological samples, was employed to characterize the morphology of protein-based objectives, including the N protein antigen, its corresponding antibody, and the conditions of their conjugation. As depicted in Figure 14c, the N protein antigen exhibited effective conjugation with its associated antibody, which facilitated the assembly of a sandwich structure comprising PS microbeads, the N protein antigen, and modified UCNPs.

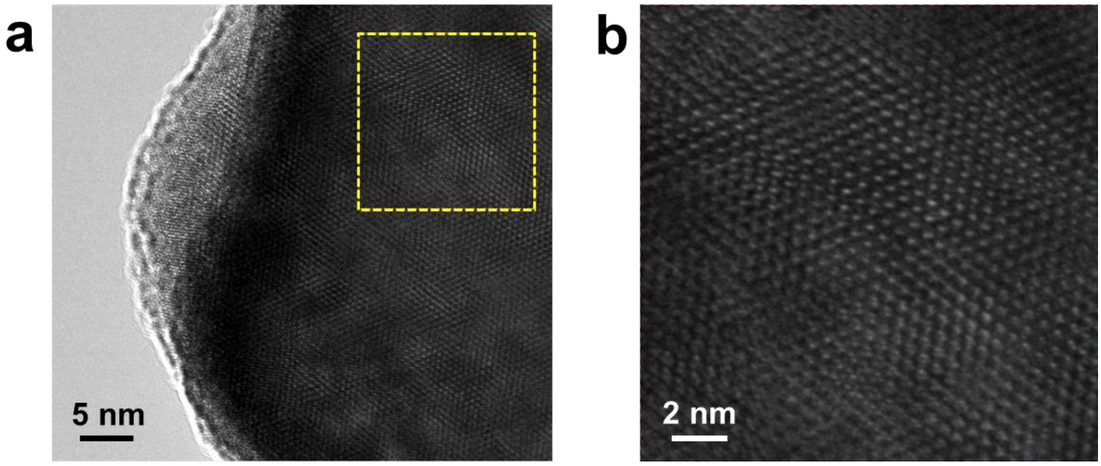

Figure 15. The HR-TEM images of prepared $NaYF_4$:Er^{3+}/Yb^{3+} UCNPs with (a) partial region pattern and (b) its selected area expended scanning image.

For purpose of investigating the surface modification of the synthesized upconversion nanoparticles (UCNPs), Fourier transform infrared spectroscopy was employed, as illustrated in Figure 16. The results indicate that the initial oleic acid ligand was eliminated following acid treatment, and that polyacrylic acid was effectively applied to the UCNPs during the subsequent modification process.

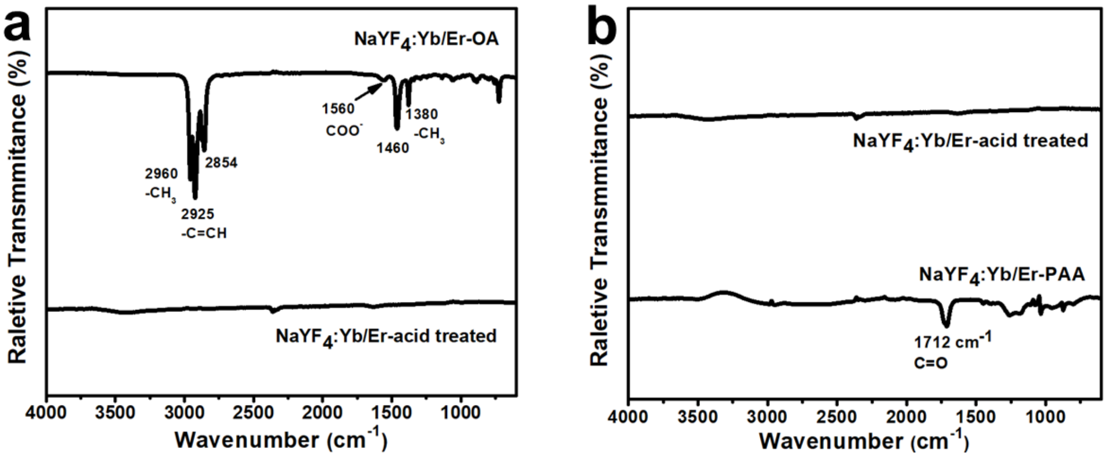

Figure 16. (a) The FTIR spectra of $NaYF_4$:Yb/Er-OA and acid treated $NaYF_4$:Yb/Er nanoparticles. (b) The FTIR spectra of acid treated $NaYF_4$:Yb/Er and modified $NaYF_4$:Yb/Er-PAA nanoparticles.

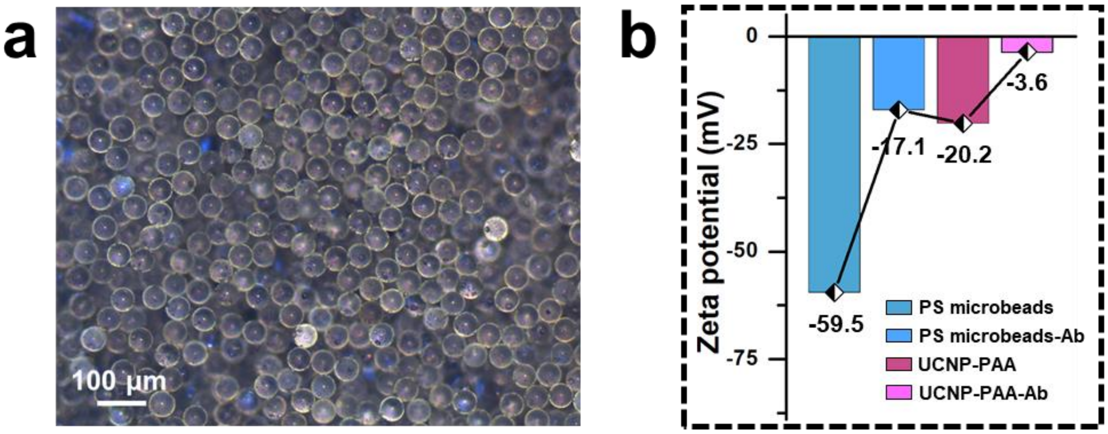

Figure 17. (a) The acquired optical photo of PS microbeads under the reflection and bright field mode. (b) Zeta potential of PS microbeads and UCNPs before and after conjugation with the antibody.

Additionally, the PS microbeads (Figure 17a) displayed excellent transparency, which aids in the acquisition of optical signals within the filtration area of the MFC chamber. As illustrated in Figure 17b, the zeta potential measurements further confirmed the successful modification of antibodies on the surfaces of the PS microbeads and UCNPs. It was noted that the zeta potential of the PS microbeads decreased from -59.5 to -17.1 mV following antibody modification. Similarly, the zeta potential of the UCNPs also dropped from -20.2 to -3.6 mV due to the binding of antibodies. This change in zeta potential indicates that the specific antibodies were effectively conjugated to the surfaces of both the PS microbeads and UCNPs.

3.3.3 PL properties of utilized UCNPs

The UCNPs are utilized as photoluminescent agents for detecting the N protein because they have lower background interference in the near-infrared (NIR) range compared to ultraviolet (UV) excitation. The related photoluminescence properties were studied as shown in Figure 18a. Under NIR (980 nm) excitation, the emissions of Er/Yb co-doped UCNPs present five peaks located at 378, 408, 521, 540, and 654 nm, which resulted from the excited state of $^4G_{11/2}$, $^2H_{9/2}$, $^2H_{11/2}$, $^4S_{3/2}$, and $^4F_{9/2}$ to the ground state of $^4I_{15/2}$, respectively. The highest emission peak was located at 540 nm indicating the optical color of the UCNPs (left inset of Figure 18a) utilized for the later virus diagnosis research.

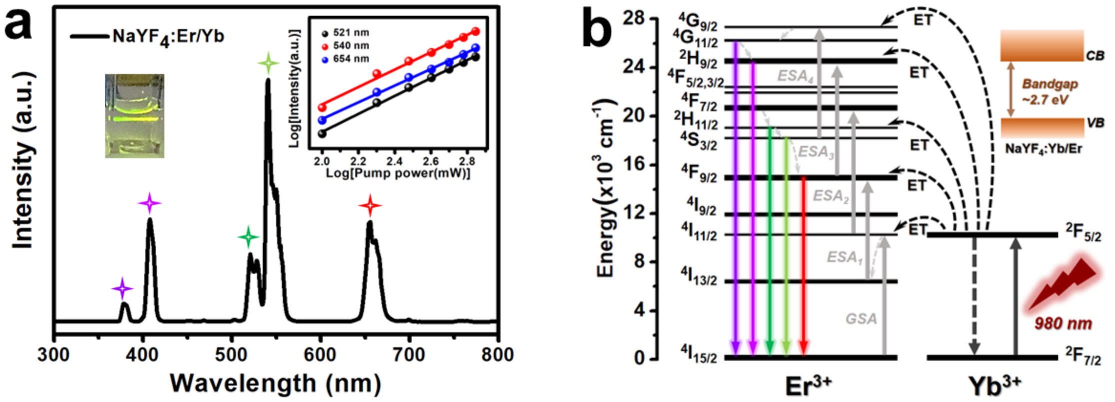

Figure 18. (a) The NaYF4:Er^{3+}/Yb^{3+} UCNPs spectrum from 300 nm to 800 nm. Left inset exhibiting the photo of UCNPs (~1mg/ml) dispersed in cyclohexane under 980 nm excitation. Right inset: the power dependent emission spectra indicating the two-photon upconversion process. (b) Upconversion energy transfer diagram of Er^{3+} and Yb^{3+} ions.

The power dependent emission spectra were examined for the participation of upconversion photons. As illustrated in the inset of Figure 18a, the slopes are 1.98, 1.93, and 1.84 for the emission peaks of 521, 540, and 654 nm, respectively. According to a relationship of $I \propto P^n$, the I stands for the luminescent intensity, P represents the pump power, and n is the average upconversion photons [92-94]. After the logarithmic treatment of pump power and intensity, the data points of logarithmic I and P presents linear relationship, and the slopes were related to the photons. As a result, it can be demonstrated that it takes place a two-photon upconversion process in the $NaYF_4:Er^{3+}/Yb^{3+}$ UCNPs.

The related upconversion energy transfer process of codoped Er^{3+}/Yb^{3+} ions is indicated in Figure 18b. It consists of numerous processes, such as energy transfer (ET), ground state absorption (GSA), and excited state absorption (ESA) for the entire upconversion transitions. The upconversion mechanism of red emission (654 nm) is mainly: Ground state level $^4I_{15/2}$ jumps to $^4I_{11/2}$ level after absorbing 980 nm excitation light. Then, the excited state level of $^4I_{11/2}$ relaxes non-radioactively to the $^4I_{13/2}$ and jumps to $^4F_{9/2}$ due to ESA process. Finally, the radiative relaxation from $^4F_{9/2}$ level to ground state brings the red light (654 nm) emission. For the two green emissions, under a 980 nm excitation, the population of Er^{3+} ions pump to the excited state of $^4I_{11/2}$ from ground state $^4I_{15/2}$ and then transitions to $^4F_{7/2}$ through the ESA process. It happens the non-radioactively process from the $^4F_{7/2}$ to $^2H_{11/2}$ level and $^2H_{11/2}$ to $^4S_{3/2}$ level. Finally, the radiation transitions from the $^2H_{11/2}$ and $^4S_{3/2}$ levels to the ground state level were irradiated to green emission (521 and 540 nm), respectively.

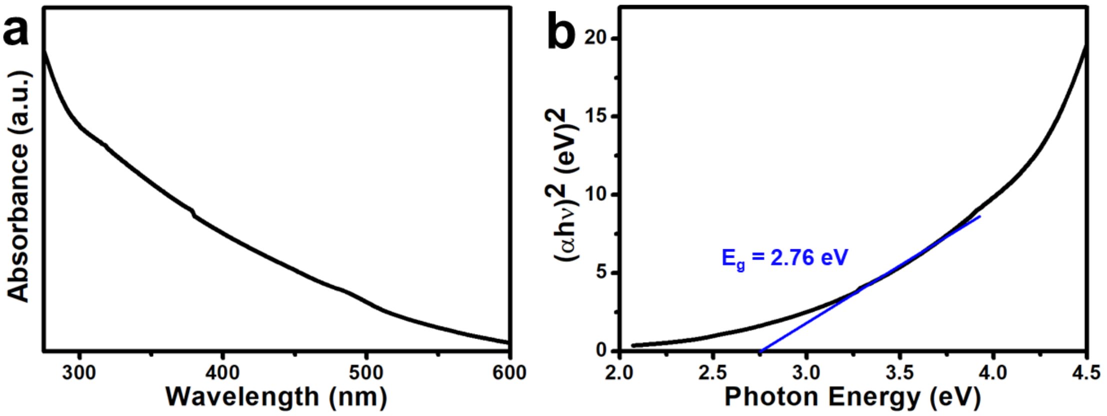

Figure 19. (a) The absorbance spectra and its Tauc-plot (b) of corresponding prepared $NaYF_4$:Er^{3+}/Yb^{3+} UCNPs.

In addition, two violet emissions of 378 and 408 nm are probably originated from the excited state of $^4G_{11/2}$ and $^2H_{9/2}$ transitions to $^4I_{15/2}$ ground stat. Among these, the above emission processes are enhanced due to the doping of the Yb^{3+} ions via the several ET processes. The relevant bandgap value of UCNPs matrix was measured and calculated to about 2.7 eV from the Tauc-plot in Figure 19 [95, 96]. Moreover, the lifetimes are illustrated in Figure 20, where various emission peaks of 378, 408, 521, 540, and 654 nm were also investigated through the photoluminescence decay time, which reveals that the lifetime is 180.6, 207.1, 338.3, 321.1, and 570.7 μs, respectively.

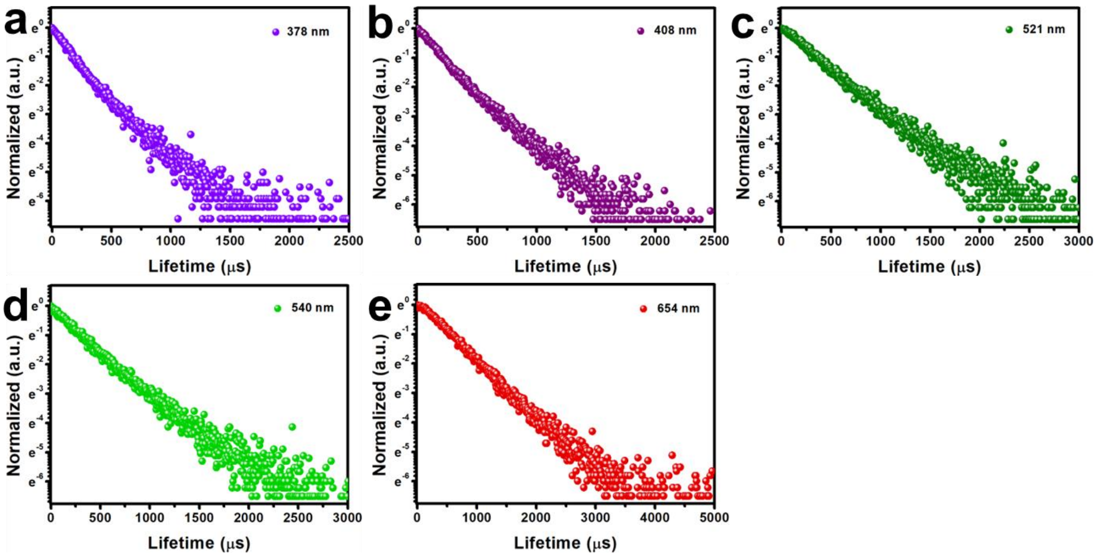

Figure 20. The relevant photoluminescence decay time of upconversion emission at (a) 378 nm, (b) 408 nm, (c) 521 nm, (d) 540 nm, and (e) 654nm.

3.3.4 Separation and concentrating properties of microfluidic biochip

The constructed MFC was used as a sample chamber in a diagnostic platform, with multiple MFC channels designed for separation and concentration purposes. In MFC-1, illustrated in Figure 21, the pillar gap for the first-order filtration system was 25 μm, while the second-order filtration system had a pillar gap of 35 μm.

However, a limitation of this MFC layout was the presence of background noise, likely due to the limited number of separation stages. To address this, a three-order filtration system was developed and created as MFC-2, as depicted in Figure 22. In this MFC, the pillar gaps for the first, second, and third-order filtration systems were 15, 25, and 35 μm, respectively. This MFC configuration demonstrated improved primary separation capabilities compared to MFC-1, but it required a longer operational time and made the cleaning process significantly more cumbersome.

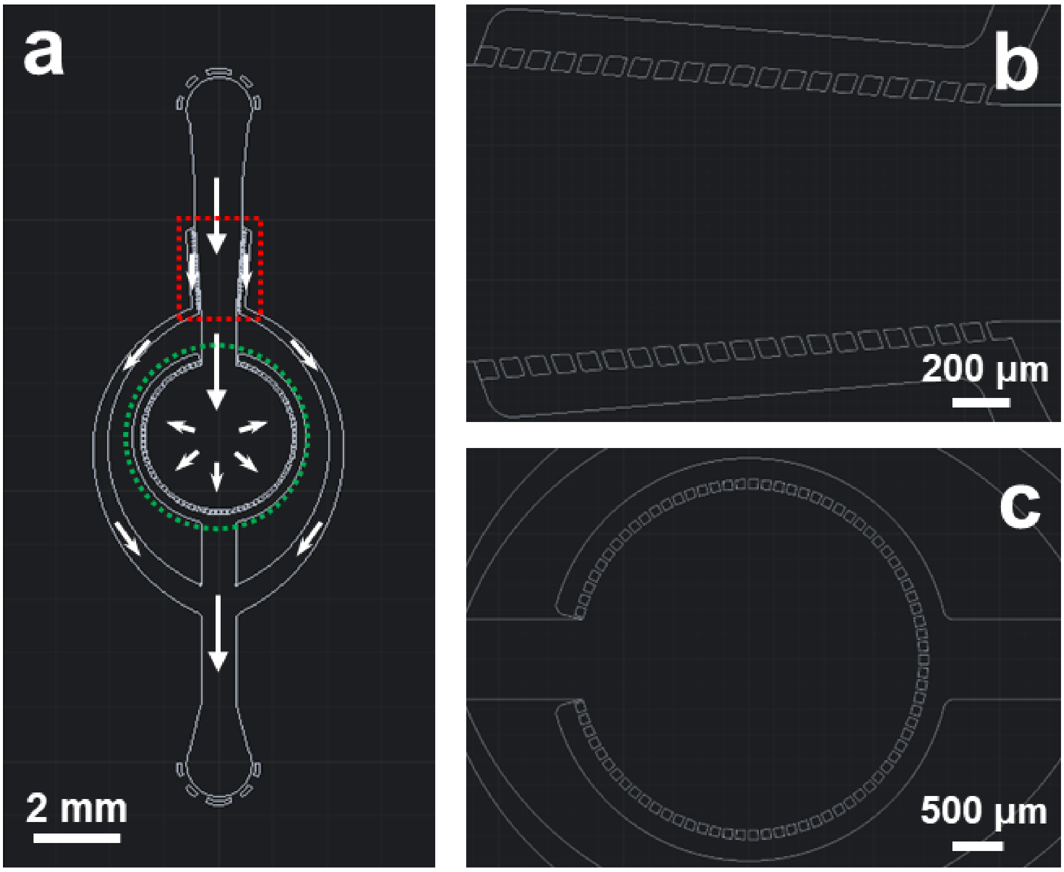

Figure 21. The AutoCAD design and related flow path of MFC-1 with (a) two order filtration system. The distinct channel details of red and green labelled area exhibiting at the (b) and (c), respectively.

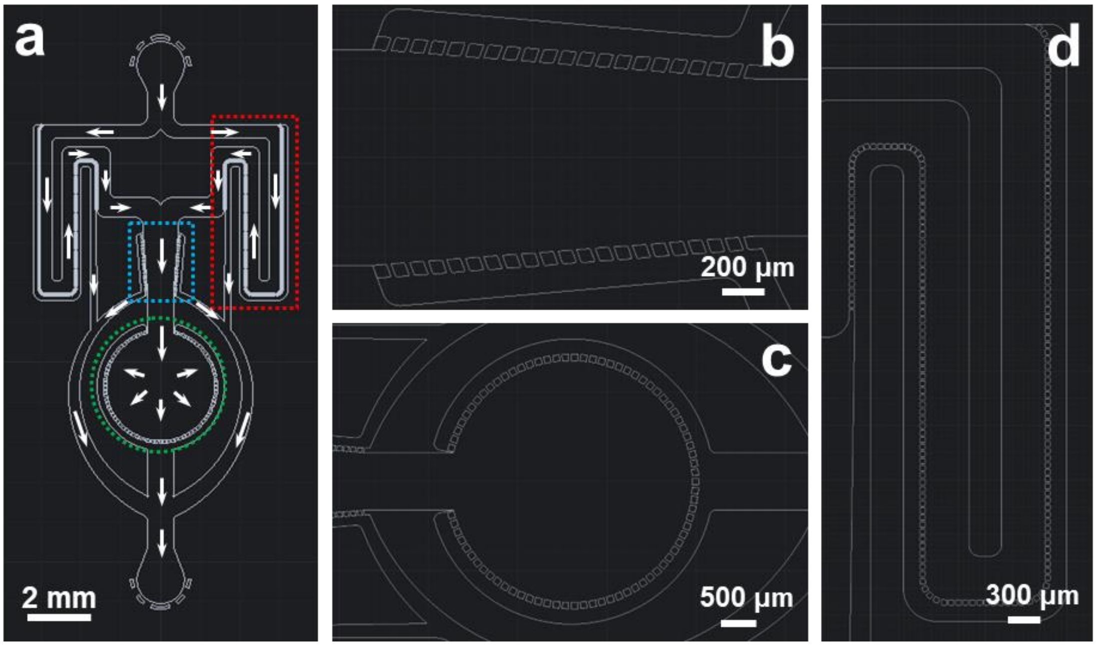

Figure 22. The AutoCAD design pattern and flow path of MFC-2 with (a) three order filtration system. The relevant detailed pattern with blue, green, and red marked area showing at (b-d), respectively.

As a result, the MFC-3, featuring improved channel designs as illustrated in Figure 23a, was chosen as the optimized microfluidic device. This device has a three-stage filtration system with pillar gaps of 15, 25, and 35 μm, as detailed in the AutoCAD design drawing in Figure 24. The lower panels of Figure 23a demonstrate that the fabricated PDMS channels are well-connected to the glass slide due to chemical bonding. The images (i) to (iii) in Figure 24 depict the three-tier separation pillars of the designed MFC, which facilitate the primary and secondary separation of unconjugated UCNPs and the filtration of conjugated PS microbeads, respectively. Furthermore, PDMS and glass were chosen for their high transparency and chemical bonding properties, making them suitable for NIR excitation applications.

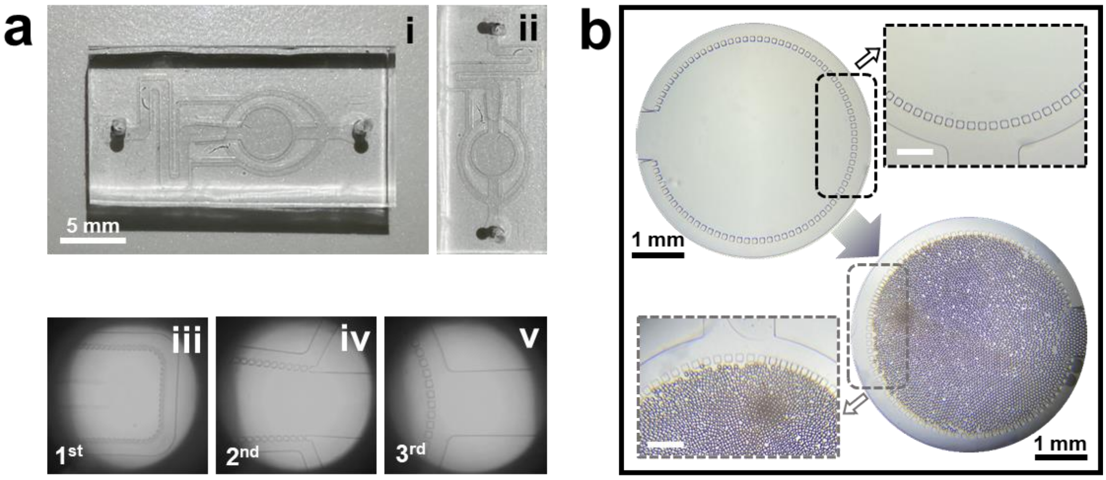

Figure 23. (a) The designed channels of microfluidic biochips and related microscale images. (b) The filtration performance of designed microfluidic biochips.

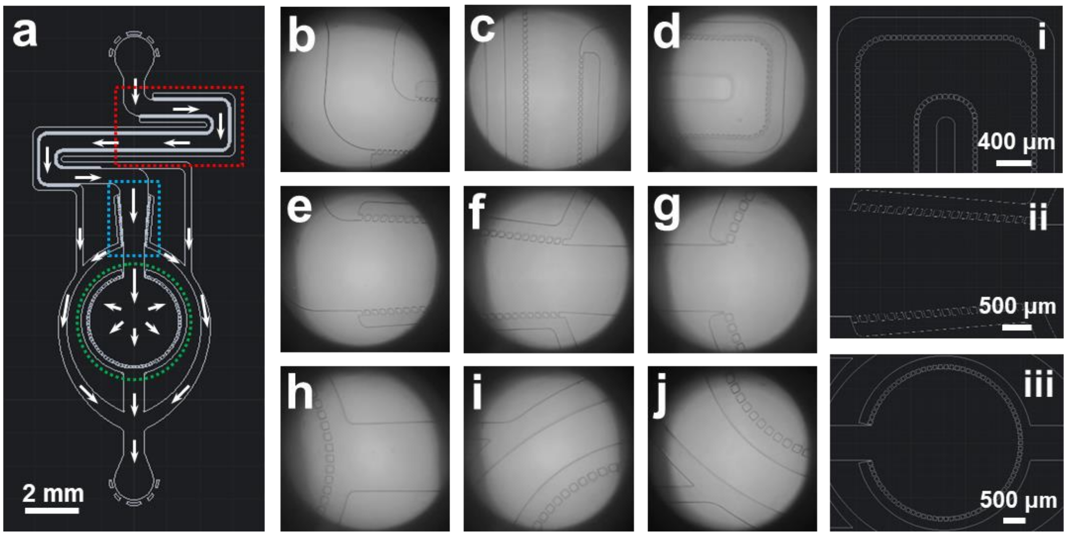

Figure 24. The AutoCAD design pattern and flow path of MFC-3 with (a) three order filtration system. The detailed pattern of three order filtration with red, blue, and green marked region showing at (i-iii), respectively. The related optical photos exhibiting at (b-j), among them, (b-c) representing the first order filtration, (e-g) illustrating the second order filtration, and the (h-j) indicating the third order filtration.

The separation property of these biochips is demonstrated in Figure 23b and Figure 24a. It can be clearly observed that the conjugated PS microbeads were effectively filtered in the circular area, showcasing the excellent dual capabilities of separation and concentration of the microfluidic biochip. Additionally, the cleaning process reveals that this microfluidic biochip has good cleanability, suggesting significant potential for applications in biosensing. Furthermore, the Figure 25 illustrates that the color distribution of the designed MFC, both with and without PS microbeads from the COMSOL simulation, is uniform, indicating a consistent velocity gradient due to the circular design of the filtration pillars.

The images illustrated in Figure 26 demonstrate the concentration capabilities of this microfluidic biochip. A noticeable bright light can be seen in the concentrating area of the MFC, in contrast to the dispersed state of the conjugated PS microbeads under liquid conditions after NIR irradiation. Furthermore, optical images captured by a bright field microscope showed that the PS microbeads emitted a bright green light when conjugated with UCNPs through the N protein, providing additional evidence for the conjugation and concentration of the linked PS microbeads with UCNPs.

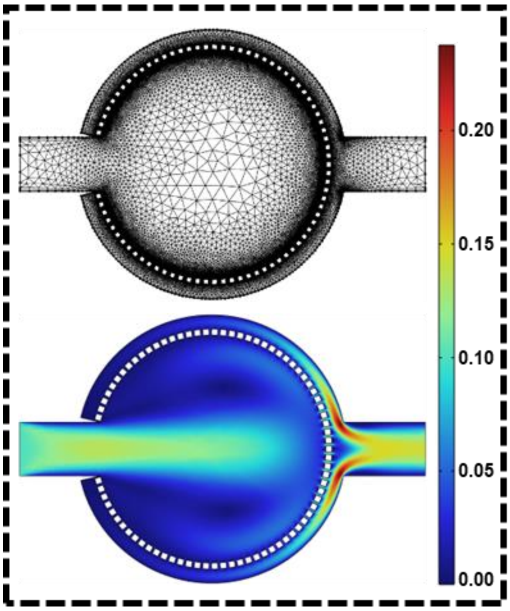

Figure 25. The COMSOL simulation and corresponding mesh calculation.

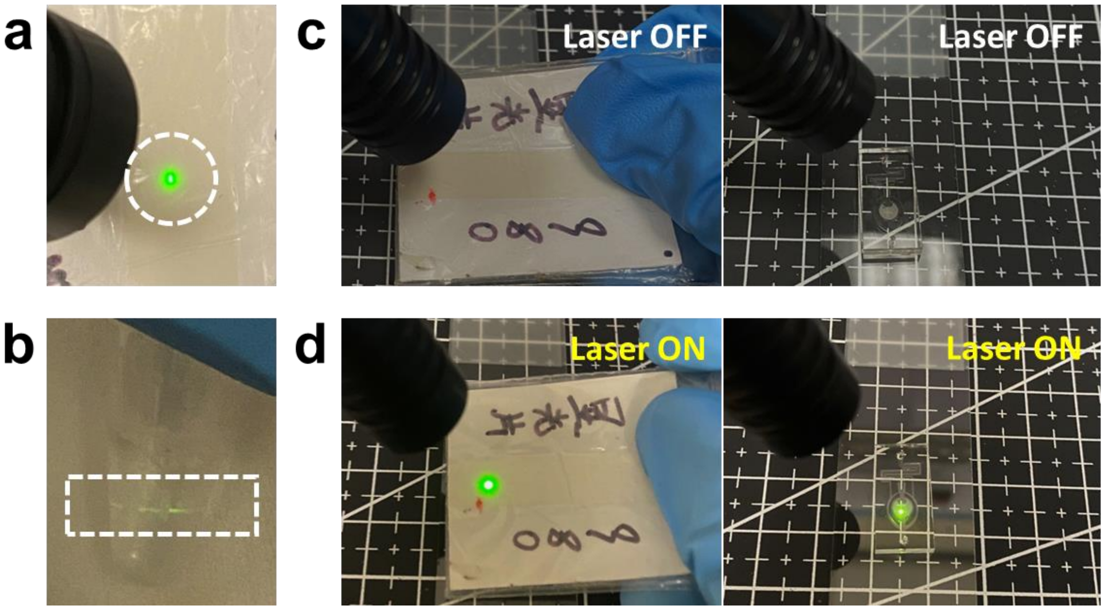

Figure 26. The relevant concentrating ability of the designed microfluidic biochips. (a) Photo of the IR card with green emission. (b) Related picture of the connected PS

microbeads dispersing in liquid environment with little green light. (c) Optical images of IR detection card (left) and concentrated conjugated PS microbeads in central zone of MFC (right) without 980 nm laser excitation. (d) Optical photos of IR detection card (left) and concentrated conjugated PS microbeads in MFC (right) under 980 nm laser irradiation with green emission.

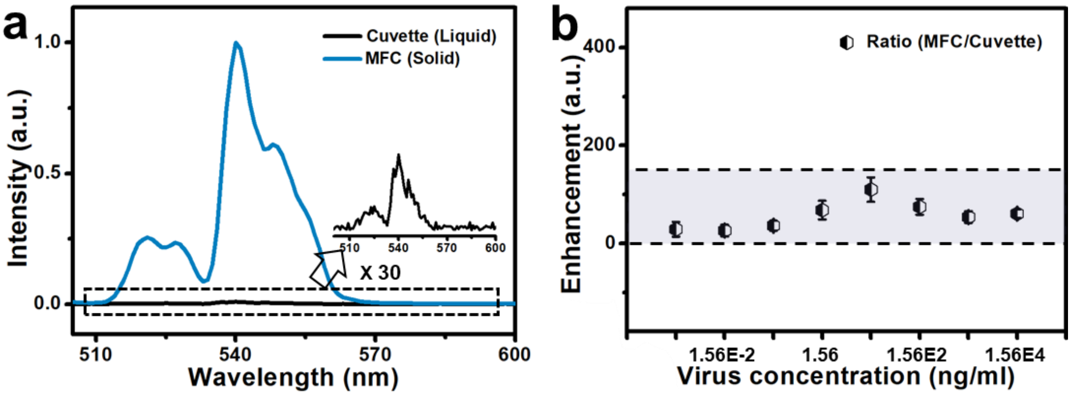

Figure 27. (a) The emission spectra of the connected UCNPs in MFC or cuvette condition. (b) The emission enhancement performance of MFC connected UCNPs with various N protein concentrations.

The use of the MFC chamber resulted in an increased photoluminescence intensity in the emission spectra, as illustrated in Figure 27a. The normalized spectra reveal that the PL intensity can be enhanced by over 100 times when conjugated UCNPs are concentrated on the surface of PS microbeads, compared to the cuvette sample, based on the PL intensity ratio at the emission peak around 540nm. Additionally, varying concentrations of virus conjugation showed improved PL intensities in the MFC mode compared to the cuvette form, as depicted in Figures 27b and 28. This enhancement in PL emission is attributed to the concentration of luminescent PS microbeads in the separation zone of the designed MFC, in contrast to the liquid state of cuvette samples, as shown in Figure 29. The impressive performance of the designed MFC, with its numerous advantages, suggests a promising application for future portable virus diagnostic platforms.

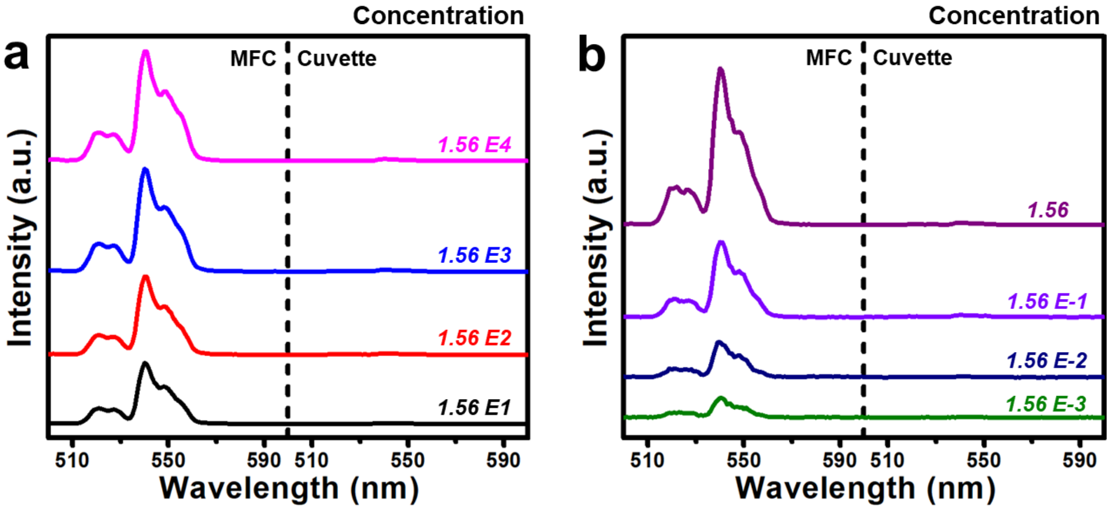

Figure 28. The emission spectra comparison of cuvette and MFC mode with different concentration.

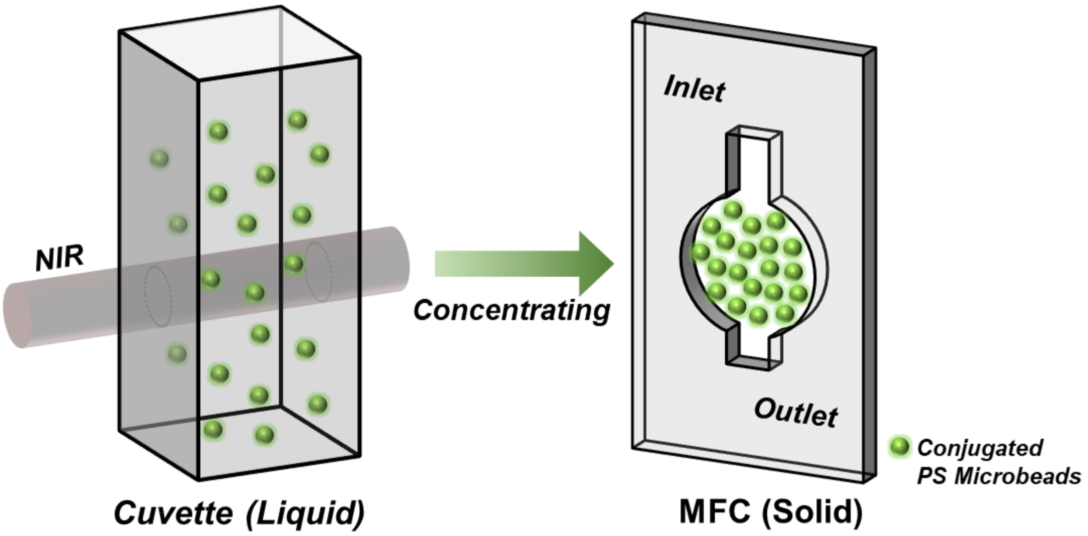

Figure 29. Schematic diagram of MFC concentrating capability from the cuvette with liquid condition to MFC with solid mode.

3.3.5 Detection performance of microfluidic biochip platform

In terms of the virus detection concerning the N protein, the assessment of detection limits and conjugation specificity is critical for determining diagnostic performance [97]. As illustrated in Figure 30a, an increase with the concentration of the N protein correlates with an increase in photoluminescence (PL) intensity, which can be attributed to the accumulation of conjugated upconversion nanoparticles (UCNPs) on the surface of polystyrene (PS) microbeads. Furthermore, it is obvious that the enhancement in PL intensity exhibited a tendency to plateau at elevated protein concentrations. The associated lifetime at the emission peak of 540 nm was analyzed through the decay curve presented in Figure 30b. The results indicate that the lifetime of Er^{3+} ions remained constant before and after the introduction of N proteins, suggesting that the conjugation of UCNPs to the PS microbeads does not influence the luminescent lifetime. This observation also implies the absence of an energy transfer process (Figure 30c) between the UCNPs and PS microbeads. This phenomenon may be explained by the characteristic absorbance wavelength of PS microbeads, which is approximately 260 nm, corresponding to the π-π* electronic transition of the aromatic ring in the styrene monomer, a wavelength that is significantly misaligned with the emission peaks of Er^{3+} ions [98].

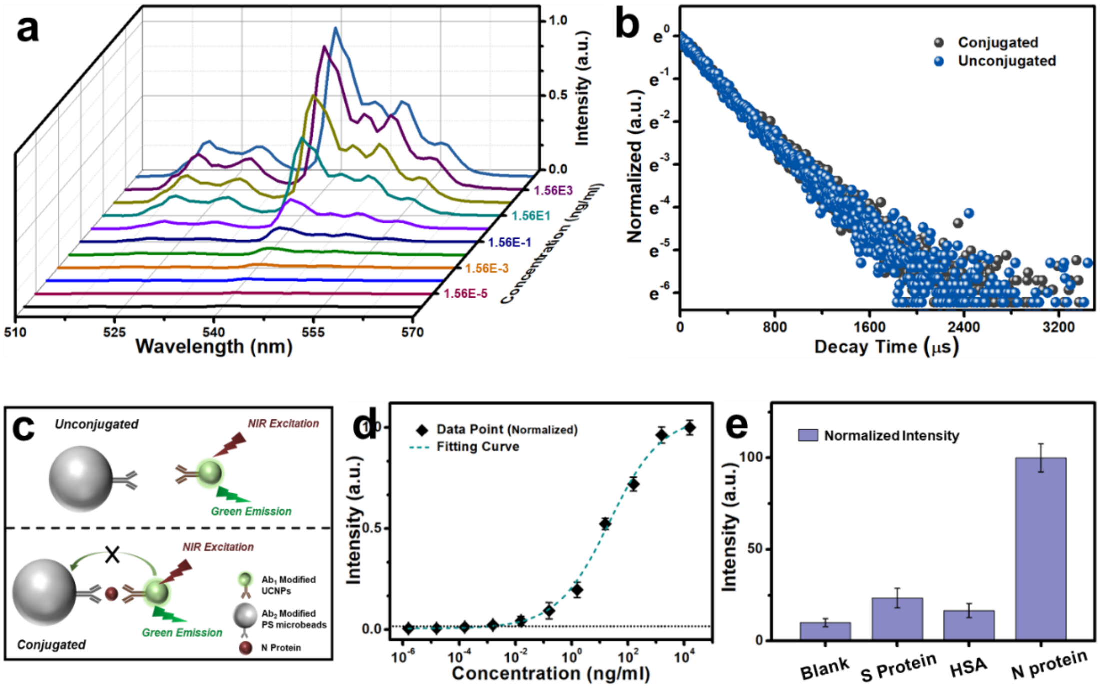

Figure 30. (a) The related emission spectra of utilized PS microbeads with various N protein concentration. (b) The decay time with or without N protein connection. (c) The schematic diagram of probable energy transfer mechanism between the

unconjugated/conjugated PS microbeads and modified UCNPs. (d) Detection limit of MFC concentrated PS microbeads conjugated with N protein. (e) Specificity test N protein detection with PS microbeads and modified UCNPs.

As shown in Figure 30d, it indicates the relationship between the PL intensity at the emission peak of 540 nm and the concentration of UCNPs. The PL intensity values were normalized with the maximum intensity set to 1.0 as a reference. It can be seen that PL intensity increased with the addition of N proteins, showing the trends observed in the emission spectra and optical images. At lower concentrations of N proteins, the increase in PL intensity was gradual, mainly due to the weak PL emissions from the conjugated UCNPs on the surface of PS microbeads. This trend was also noted at higher virus concentrations with additional N protein, primarily due to the saturation of PL intensity from UCNPs attached to the PS microbeads. The detection limit is generally determined by the average values of blank samples plus three times the standard deviation. As shown in Figure 30d, the detection limit was assessed at 1.12 pg/ml level, indicating that the developed platform demonstrated significant detection sensitivity, implying its potential for effective virus diagnosis.

In addition, the investigation of specificity is of great significance, which manifests the recognition capability of virus diagnostic platform for specific target antigens. As shown in Figure 30e, three different antigens including spike protein (S protein), human serum albumin (HSA), and N protein were tested for specificity research. The concentrations of proteins are diluted to around 10 μg/ml from the standard samples of

S protein (1.48 mg/ml), HAS (10 mg/ml), and N protein (1.56 mg/ml). Among them, these error bars manifest the standard deviations of three independent experiments. These results indicated that the N protein target presented higher PL intensity compared with other antigens targets and blank sample, which implied that the designed sandwich immunoassay possessed well virus diagnostic specificity. These investigations of virus detection for N protein performance indicate that this well-designed virus detection system is promising potential application for point-of-care virus diagnostics.

3.3.6 Performance comparison with commercial LFA

To demonstrate the practical detection performance, clinical samples were investigated for our virus diagnostic platform. As shown in Figure 31a, the clinical samples of Omicron variant were obtained via several procedures from the laboratory of the University of Hong Kong. At first, the isolate of Omicron (B.1.1.529) variant was acquired from the confirmed patients in Hong Kong. Next, the collected swabs of nasopharyngeal or oropharyngeal specimens were cultured in typical Vero-E6-TMPRSS2 cells for replication. The cultured Omicron variant was subsequently boiled at 95 °C for 10 minutes for virus inactivation. Ultimately, the N protein of Omicron variant was extracted and acquired for clinical samples. The commercial LFA rapid test strips as shown in Figure 31b were utilized for the N protein detection and verification of the obtained clinical viral samples. With the addition of different concentrations for clinical samples, all of these control lines of LFA strips exhibited a distinct red color indicating that the results of test line were effective for the N protein detection. For relatively quantitative analysis, the optical images of LFA rapid test strips were converted into the grayscale images for investigation.

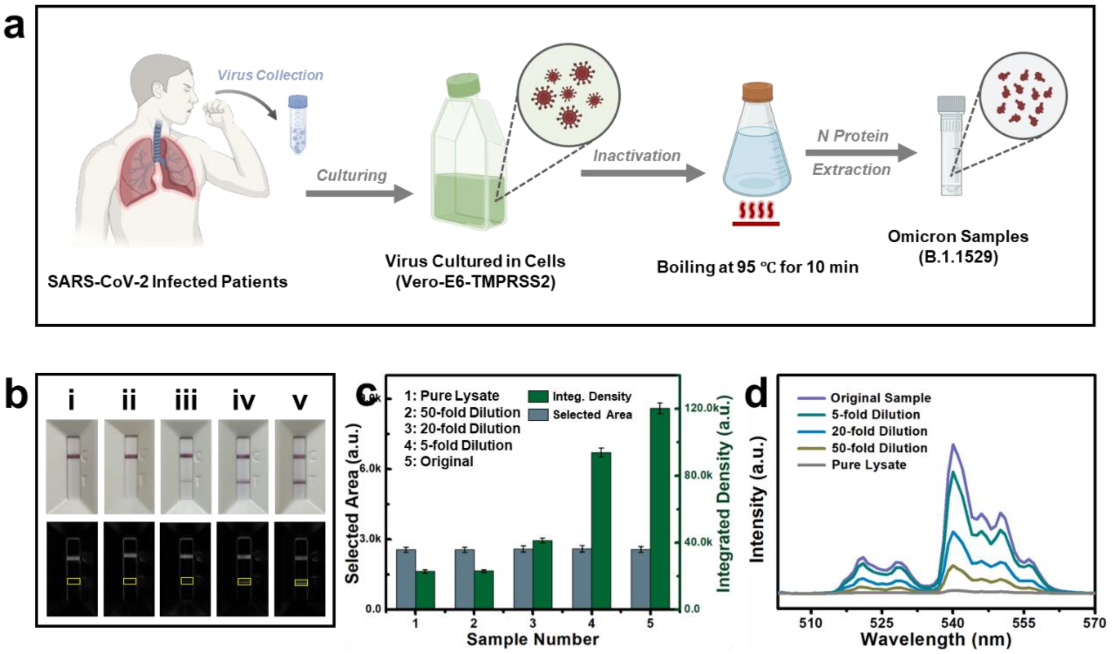

Figure 31. (a) The acquiring procedures of clinical viral samples for B.1.1529 Omicron variant N protein. (b) The optical photos of LFA rapid test strips with pure lysate (i) and different virus concentration injection (ii-v). Half bottom showing the related converted grayscale images. (c) The selected area intensity and integrated density of test line for LFA with various sample concentration and pure lysate via the grayscale images. (d) The upconversion emission spectra of designed MFC diagnostic platform with pure lysate and different concentration clinical samples.

Figure 31c illustrates the selected area and integrated density of the LFA strips test line of clinical samples with diverse dilution concentration. It can be seen that the selected area of the test line was basically same for better comparison. From the original concentration to 50-fold dilution concentration, it can be observed the integrated density tended to decrease visibly. But compared with the 50-fold dilution sample and the pure lysate, the integrated density values were basically similar, which implied that the detection sensitivity cannot reach this dilution viral concentration. Fortunately, the designed MFC assisted N protein diagnostic platform manifested excellent performance compared with the commercial LFA rapid test strips.

As shown in Figure 31d, the emission intensity also exhibited a downtrend from the original concentration to dilution clinical sample. However, instead of the inconspicuous distinguishing of 50-fold dilution sample and pure lysate for commercial LFA rapid test strips, the designed MFC assisted virus diagnostic platform possessed significant detection sensitivity. And the emission intensity of 50-fold dilution clinical sample was distinctly differentiated from the pure lysate compared with commercial LFA strips. This better diagnostic capability may probably attribute to that the targeted antigen conjugated with red color colloidal golds are captured on the test line via lateral flow and observed by naked eye instead of the UCNPs conjugated PS microbeads concentrating in central zone and emission with green light under 980 nm laser excitation. Therefore, these perfect diagnostic performances of MFC-assisted platform imply it a great potential application for virus detection.

3.3.7 Diagnostic performance for point-of-care biosensing platform

Furthermore, in order to achieve the point-of-care virus detection, a portable MFC-assisted diagnostic platform was designed and fabricated as shown in Figure 32. The flow chart of this designed portable virus detection platform is illustrated in Figure 32a involving different device components. The light sensor is one of key components of this portable virus diagnostic platform for the signal transformation from optical to electronic as shown in dashed box via BH-1750 data sheet. The elaborate MFC was utilized as the sample chamber for the point-of-care diagnostic platform as shown in Figure 32b, which consists of NIR incident light from laser source, optical path component, focus lens, MFC chamber component, voltage regulator, integrated light sensor, power supply, integrated microcontroller unit (abbreviating to MCU in the diagram), Bluetooth module, and mobile terminal.

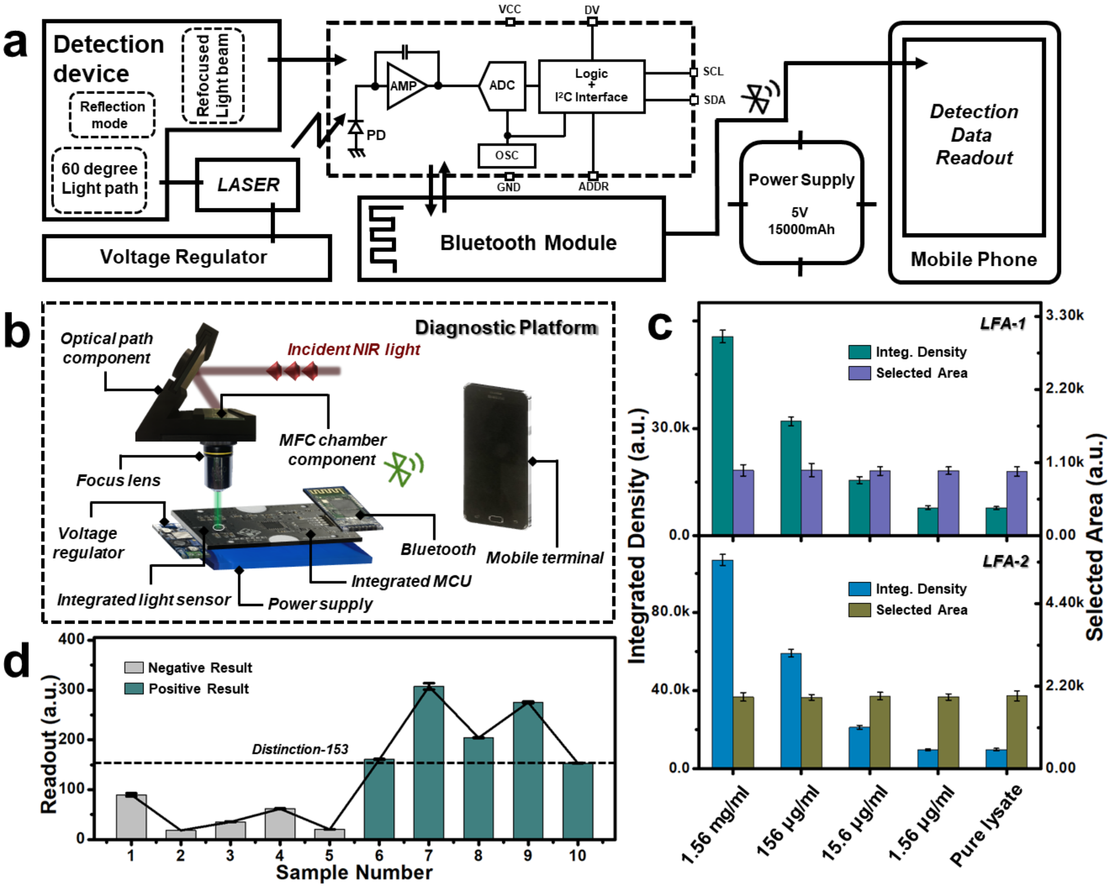

Figure 32. (a) Flow chart of portable virus diagnostic platform. (b) Schematic of diverse components for elaborate portable device. (c) Virus detection property of two different commercial N protein test strips via grey value obtained from selected area. (d) Histogram plot of virus samples detection results with negative or positive for the designed portable device.

In details, the assembled laser component generates a NIR incident light and is reflected to the concentrating zone of MFC via a reflecting mirror supported by the 3D printed holder. The separated PS microbeads conjugated with UCNPs were irradiated to a green light beam and focused to the light sensor by the focus lens. The obtained optical signals were transferred to electric signal and sent to a smartphone through the Bluetooth module. The voltage regulator balanced the voltage of electric components and the power supply with high capacity of 5V/15000mAh was selected for the longer run time of our portable virus detection platform. All of the management of programs, such as signal transition, data coding, and information sending were implemented by the integrated microcontroller unit.

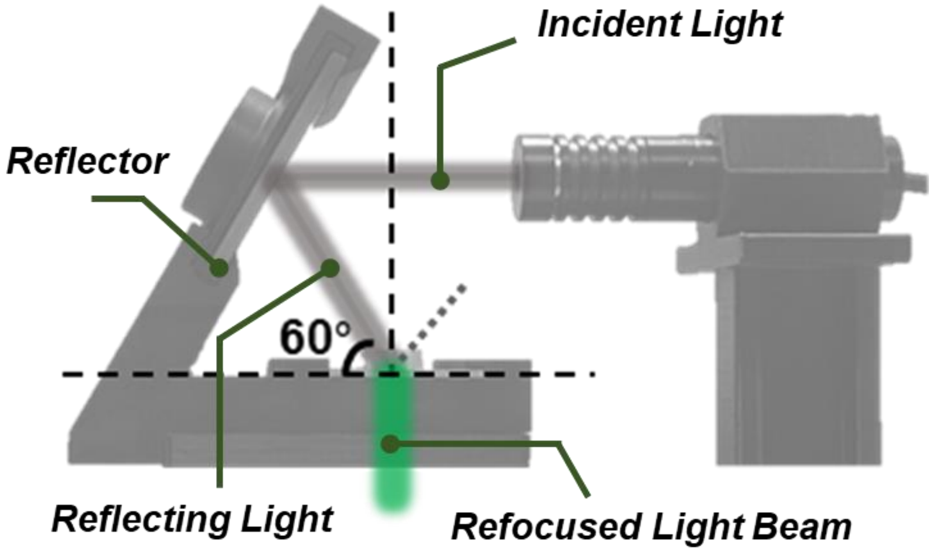

Figure 33. The designed reflected light path involving incident NIR light, reflector, reflecting light, and refocused light beam.

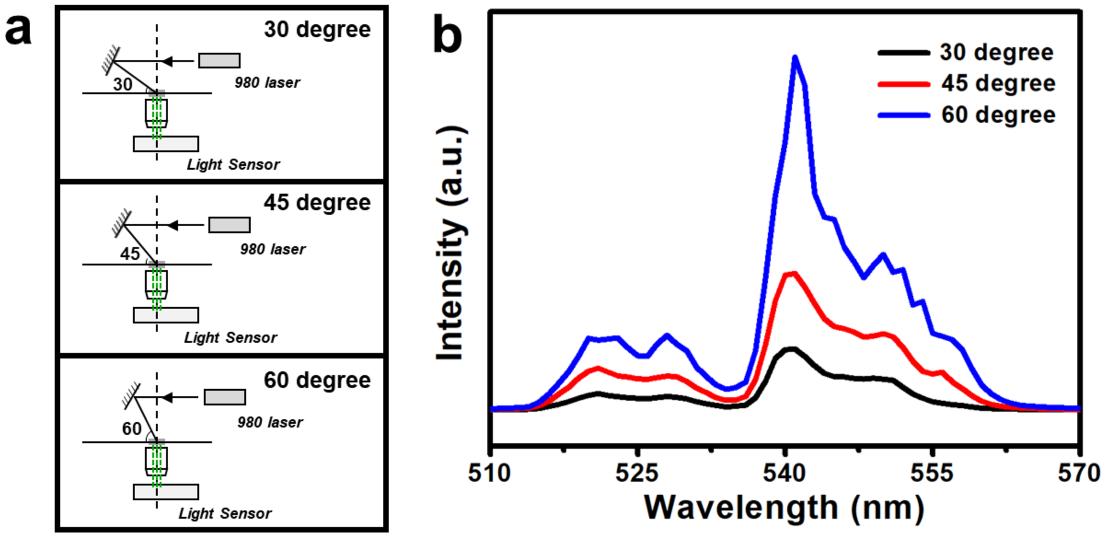

Figure 34. The schematic diagrams (a) of different light path with 30, 45, and 60 degrees. (b) The emission spectra of variant light path angles with 30, 45, and 60 degrees.

Among these components of designed detection device as shown in top left corner of Figure 32b and Figure 33, the angle selection of light path is crucial. It can be obviously observed that the 60-degree light path was selected as the optimized light path. The reason why choose reflectance optical mode is that the influence of excitation is minimized compared with the incident optical path mode. The different angles of the light path will also affect for the emission light intensity of conjugated UCNPs onto the PS microbeads concentrated in the MCF separation zone. Therefore, three typical angles for convenient fabrication of light paths were investigated as shown in Figure 34. From the Figure 34a, the schematic diagrams illustrate the three different light path angles including 30, 45, and 60 degrees. In order to study the effect of the different light paths for the monitored emission intensity, the PL emission spectra were studied as shown in Figure 34b. It can be obviously observed that the emission intensity exhibited increase trend from the 30 to 60-degree optical path. For the 60-degree light path, the emission intensity indicated as the maximum value compared with other reflectance angles, which manifested that the optimized selection of light path was determined to be 60-degree.

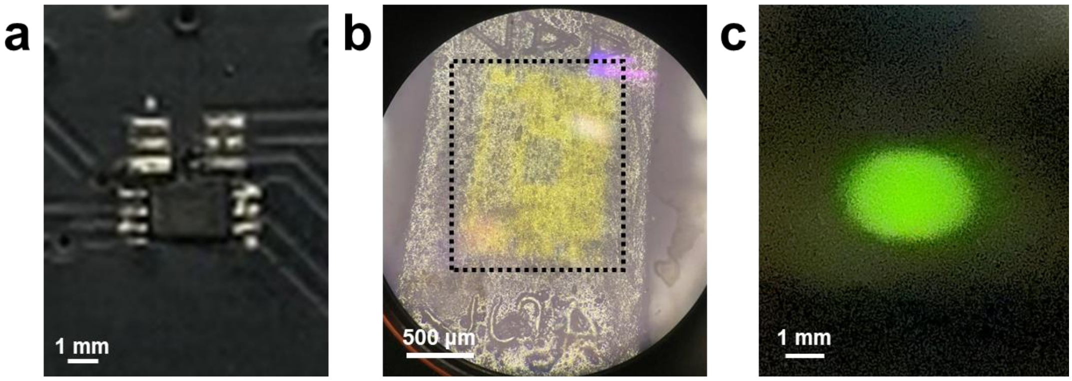

Figure 35. The integrated light sensor photos with (a) optical image of light sensor integrated with MCU. (b) The microscope photo of light sensor unit. (c) The optical spot of refocused emission light beam under the conjugated with N protein.

In addition, the corresponding properties of integrated light sensor were also studied as shown in Figure 35. The incident angle will have effect for the response of light sensors, the best incident angle was determined to be 0 degree from related BH-1750 technical note, which indicated the focused emission light of conjugated UCNPs onto surface of PS microbeads concentrated in the separation zone of MFC should enshroud the acceptance area of integrated light sensor. As shown in Figure 35a and 35b, the detection area of light sensor was determined to be around 1.5 mm^2, which was less than the focus emission light (Figure 35c).

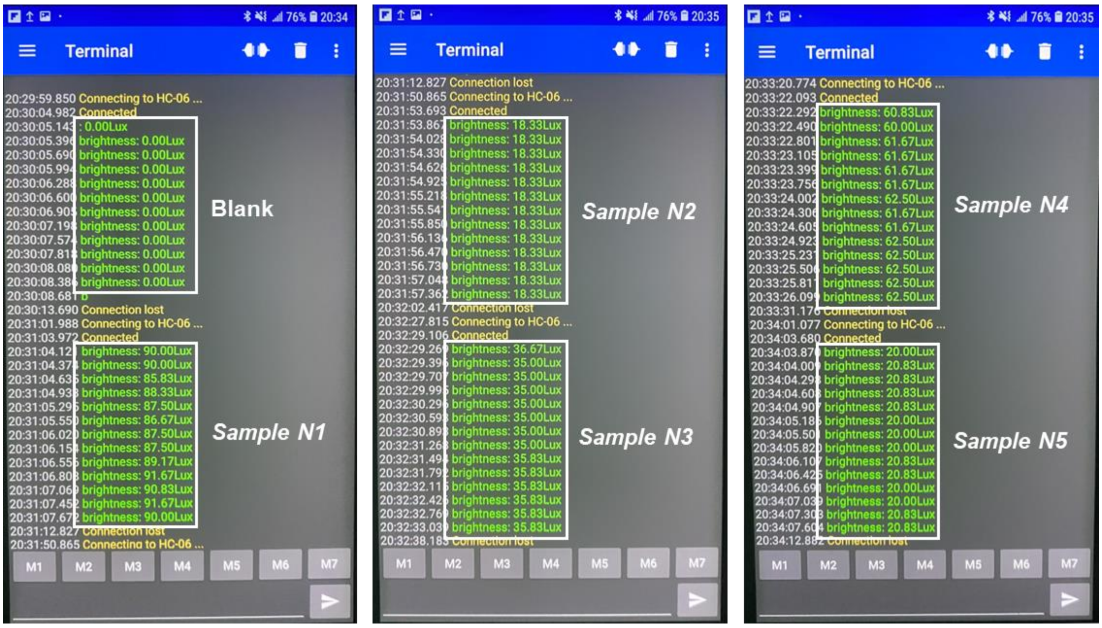

```
20:29:59.850 Connecting to HC-06 ...
20:30:04.982 Connected
20:30:05.14 : 0.00Lux
20:30:05.39 brightness: 0.00Lux
20:30:05.69 brightness: 0.00Lux
20:30:05.99 brightness: 0.00Lux
20:30:06.28 brightness: 0.00Lux
20:30:06.60 brightness: 0.00Lux
20:30:06.90 brightness: 0.00Lux
20:30:07.19 brightness: 0.00Lux
20:30:07.57 brightness: 0.00Lux
20:30:07.81 brightness: 0.00Lux
20:30:08.08 brightness: 0.00Lux
20:30:08.38 brightness: 0.00Lux
20:30:08.681
20:30:13.690 Connection lost
20:31:01.988 Connecting to HC-06 ...
20:31:03.972 Connected
20:31:04.12 brightness: 90.00Lux
20:31:04.37 brightness: 90.00Lux
20:31:04.63 brightness: 85.83Lux
20:31:04.93 brightness: 88.33Lux
20:31:05.29 brightness: 87.50Lux
20:31:05.55 brightness: 86.67Lux
20:31:06.02 brightness: 87.50Lux
20:31:06.15 brightness: 87.50Lux
20:31:06.55 brightness: 89.17Lux
20:31:06.80 brightness: 91.67Lux
20:31:07.06 brightness: 90.83Lux
20:31:07.45 brightness: 91.67Lux
20:31:07.67 brightness: 90.00Lux
20:31:12.827 Connection lost
20:31:50.865 Connecting to HC-06 ...
```

```
20:31:12.827 Connection lost
20:31:50.865 Connecting to HC-06 ...
20:31:53.693 Connected
20:31:53.867 brightness: 18.33Lux
20:31:54.028 brightness: 18.33Lux
20:31:54.330 brightness: 18.33Lux
20:31:54.62 brightness: 18.33Lux
20:31:54.92 brightness: 18.33Lux
20:31:55.218 brightness: 18.33Lux
20:31:55.54 brightness: 18.33Lux
20:31:55.85 brightness: 18.33Lux
20:31:56.13 brightness: 18.33Lux
20:31:56.47 brightness: 18.33Lux
20:31:56.73 brightness: 18.33Lux
20:31:57.04 brightness: 18.33Lux
20:31:57.36 brightness: 18.33Lux
20:32:02.417 Connection lost
20:32:27.815 Connecting to HC-06 ...
20:32:29.106 Connected
20:32:29.26 brightness: 36.67Lux
20:32:29.39 brightness: 35.00Lux
20:32:29.70 brightness: 35.00Lux
20:32:29.99 brightness: 35.00Lux
20:32:30.29 brightness: 35.00Lux
20:32:30.59 brightness: 35.00Lux
20:32:30.89 brightness: 35.00Lux
20:32:31.26 brightness: 35.00Lux
20:32:31.49 brightness: 35.83Lux
20:32:31.79 brightness: 35.83Lux
20:32:32.11 brightness: 35.83Lux
20:32:32.42 brightness: 35.83Lux
20:32:32.76 brightness: 35.83Lux
20:32:33.03 brightness: 35.83Lux
20:32:38.18 Connection lost
```

```
20:33:20.774 Connecting to HC-06 ...
20:33:22.093 Connected
20:33:22.292 brightness: 60.83Lux
20:33:22.490 brightness: 60.00Lux
20:33:22.801 brightness: 61.67Lux
20:33:23.105 brightness: 61.67Lux
20:33:23.399 brightness: 61.67Lux
20:33:23.756 brightness: 61.67Lux
20:33:24.002 brightness: 62.50Lux
20:33:24.306 brightness: 61.67Lux
20:33:24.605 brightness: 61.67Lux
20:33:24.923 brightness: 62.50Lux
20:33:25.231 brightness: 62.50Lux
20:33:25.506 brightness: 62.50Lux
20:33:25.811 brightness: 62.50Lux
20:33:26.099 brightness: 62.50Lux
20:33:31.17 Connection lost
20:34:01.077 Connecting to HC-06 ...
20:34:03.680 Connected
20:34:03.87 brightness: 20.00Lux
20:34:04.00 brightness: 20.83Lux
20:34:04.29 brightness: 20.83Lux
20:34:04.60 brightness: 20.83Lux
20:34:04.90 brightness: 20.83Lux
20:34:05.18 brightness: 20.00Lux
20:34:05.50 brightness: 20.00Lux
20:34:05.82 brightness: 20.00Lux
20:34:06.10 brightness: 20.83Lux
20:34:06.42 brightness: 20.83Lux
20:34:06.69 brightness: 20.00Lux
20:34:07.03 brightness: 20.00Lux
20:34:07.30 brightness: 20.83Lux
20:34:07.60 brightness: 20.83Lux
20:34:12.88 Connection lost
```

Figure 36. The mobile phone screen photos of portable device readout values for one blank test and five negative samples detection.

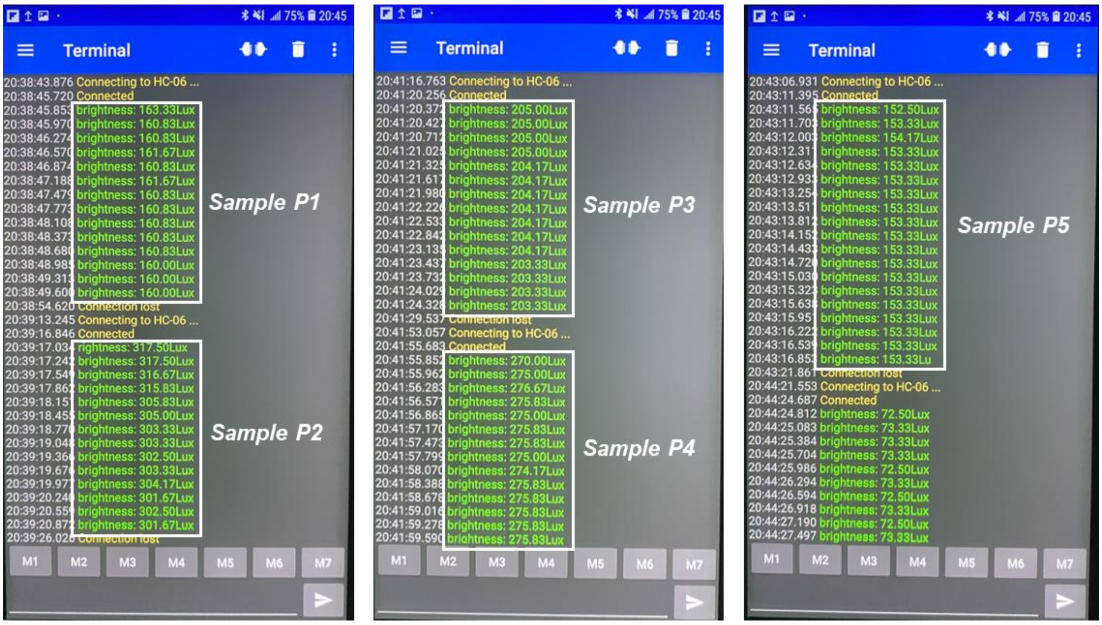

```
20:38:43.876 Connecting to HC-06 ...
20:38:45.720 Connected
20:38:45.853 brightness: 163.33Lux
20:38:45.970 brightness: 160.83Lux
20:38:46.274 brightness: 160.83Lux
20:38:46.570 brightness: 161.67Lux
20:38:46.874 brightness: 160.83Lux
20:38:47.188 brightness: 161.67Lux
20:38:47.479 brightness: 160.83Lux
20:38:47.773 brightness: 160.83Lux
20:38:48.108 brightness: 160.83Lux
20:38:48.373 brightness: 160.83Lux
20:38:48.680 brightness: 160.83Lux
20:38:48.985 brightness: 160.00Lux
20:38:49.313 brightness: 160.00Lux
20:38:49.600 brightness: 160.00Lux
20:38:54.620 Connection lost
20:39:13.245 Connecting to HC-06 ...
20:39:16.846 Connected
20:39:17.034 rightness: 317.50Lux
20:39:17.242 brightness: 317.50Lux
20:39:17.549 brightness: 316.67Lux
20:39:17.862 brightness: 315.83Lux
20:39:18.157 brightness: 305.83Lux
20:39:18.455 brightness: 305.00Lux
20:39:18.770 brightness: 303.33Lux
20:39:19.048 brightness: 303.33Lux
20:39:19.366 brightness: 302.50Lux
20:39:19.676 brightness: 303.33Lux
20:39:19.977 brightness: 304.17Lux
20:39:20.240 brightness: 301.67Lux
20:39:20.559 brightness: 302.50Lux
20:39:20.872 brightness: 301.67Lux
20:39:26.026 Connection lost
```

```
20:41:16.763 Connecting to HC-06 ...
20:41:20.256 Connected
20:41:20.372 brightness: 205.00Lux
20:41:20.427 brightness: 205.00Lux
20:41:20.712 brightness: 205.00Lux
20:41:21.025 brightness: 205.00Lux
20:41:21.325 brightness: 204.17Lux
20:41:21.617 brightness: 204.17Lux
20:41:21.980 brightness: 204.17Lux
20:41:22.226 brightness: 204.17Lux
20:41:22.533 brightness: 204.17Lux
20:41:22.842 brightness: 204.17Lux
20:41:23.135 brightness: 204.17Lux
20:41:23.437 brightness: 203.33Lux
20:41:23.732 brightness: 203.33Lux
20:41:24.029 brightness: 203.33Lux
20:41:24.328 brightness: 203.33Lux
20:41:29.537 Connection lost
20:41:53.057 Connecting to HC-06 ...
20:41:55.683 Connected
20:41:55.852 brightness: 270.00Lux
20:41:55.962 brightness: 275.00Lux
20:41:56.283 brightness: 276.67Lux
20:41:56.571 brightness: 275.83Lux
20:41:56.865 brightness: 275.00Lux
20:41:57.170 brightness: 275.83Lux
20:41:57.473 brightness: 275.83Lux
20:41:57.799 brightness: 275.00Lux
20:41:58.070 brightness: 274.17Lux
20:41:58.388 brightness: 275.83Lux
20:41:58.678 brightness: 275.83Lux
20:41:59.016 brightness: 275.83Lux
20:41:59.278 brightness: 275.83Lux
20:41:59.590 brightness: 275.83Lux
```

```
20:43:06.931 Connecting to HC-06 ...
20:43:11.395 Connected
20:43:11.565 brightness: 152.50Lux
20:43:11.703 brightness: 153.33Lux
20:43:12.003 brightness: 154.17Lux
20:43:12.311 brightness: 153.33Lux
20:43:12.634 brightness: 153.33Lux
20:43:12.933 brightness: 153.33Lux
20:43:13.254 brightness: 153.33Lux
20:43:13.511 brightness: 153.33Lux
20:43:13.812 brightness: 153.33Lux
20:43:14.152 brightness: 153.33Lux
20:43:14.433 brightness: 153.33Lux
20:43:14.720 brightness: 153.33Lux
20:43:15.030 brightness: 153.33Lux
20:43:15.323 brightness: 153.33Lux
20:43:15.638 brightness: 153.33Lux
20:43:15.951 brightness: 153.33Lux
20:43:16.222 brightness: 153.33Lux
20:43:16.539 brightness: 153.33Lux
20:43:16.853 brightness: 153.33Lu
20:43:21.861 Connection lost
20:44:21.553 Connecting to HC-06 ...
20:44:24.687 Connected
20:44:24.812 brightness: 72.50Lux
20:44:25.083 brightness: 73.33Lux
20:44:25.384 brightness: 73.33Lux
20:44:25.704 brightness: 73.33Lux
20:44:25.986 brightness: 72.50Lux
20:44:26.294 brightness: 73.33Lux
20:44:26.594 brightness: 72.50Lux
20:44:26.918 brightness: 73.33Lux
20:44:27.190 brightness: 72.50Lux
20:44:27.497 brightness: 73.33Lux
```

Figure 37. The optical images of portable device readout values in mobile phone for five positive samples detection.

The two commercial LFA rapid test strips were investigated for detection sensitivity via the addition of standard N protein samples. In order to quantitatively analyze the diagnostic performance, these optical photos were converted into the grayscale images as well. As shown in Figure 32c, the selected area of test line of LFA strip was controlled basically as the same value for the better comparison. It can be observed that the integrated density tended to growth as the increased addition of N protein concentration. The tested LFA strips exhibited poor virus detection performance and were estimated as the level of around 1.56 μg/ml, which was similar to commercial LFA strips but well below the sensitivity of our designed MFC assisted virus diagnostic platform [99]. In addition, ten random N protein samples were also studied on the portable virus diagnostic platform for the negative and positive results acquired from the cell phone for the mobile scene application. As shown in the Figure 32d and Figure 36-37, the distinction line between the negative and positive sample was determined to be 153 from the readout of the mobile phone. The two different sample groups of negative or positive indicated significant differences, which possessed well potential application for the diagnostic results distinguishing.

3.4 Summary

In summary, the MFC-assisted portable N protein diagnostic platform was designed and fabricated successfully. The synthesized $NaYF_4:Er^{3+}/Yb^{3+}$ UCNPs with excellent luminescent stability and uniformity were used as the luminescent indicator for sandwich structure immunoassay. The designed MFC was utilized as the detection chamber of the portable virus diagnostic platform, which illustrated outstanding filtration performance for the conjugated PS microbeads. The fabricated MFC possessed excellent luminescence enhancement properties with a maximum of over 100-fold than the cuvette samples. Moreover, the cleanable performance of MFC also implied great potential application for the virus diagnosis field. Compared with the typical commercial LFA rapid test strips for virus detection, the MFC-assisted portable N protein diagnostic platform exhibited a higher biosensing sensitivity of around 1.12 pg/ml. In addition, the clinical samples also manifested that the MFC-assisted virus detection platform possessed better diagnostic sensitivity compared with the usual commercial LFA rapid test strips. These outstanding detection capabilities implied that the designed MFC-assisted portable virus diagnostic platform possessed enormous potential applications for the future unpredictable virus detection area.

Chapter 4 Point-of-care biodetection platform based on QDs and biochip for CEA biomarker diagnosis

4.1 Introduction

As a hard-to-cure disease, the cancer has always affected the health and life of human beings [100-102]. During year 2022, the lung cancer is regarded as a frequently diagnosed and major cause of cancer-relevant death, which results in approximately 1.8 million deaths [103]. Lots of important tumor markers including CYFRA21-1, CA125, and SCC-Ag are common used for the non-small-cell lung cancer detection [104]. Besides, the pancreatic cancer is usually recognized the king of carcinoma, representing highly lethal disease and with great difficulty for therapy, in which the CA 19-9 tumor marker is validated and widely utilized for pancreatic cancer diagnosis [105, 106]. In that case, achieving sensitive and accurate identification of associated tumor markers is crucial for early cancer detection and screening.

For *in-vivo* imaging diagnostics of cancer, radiology methods such as computed tomography and magnetic resonance imaging scans are frequently employed [107]. These techniques have certain limitations that limit their use, such as expensive detection costs, the need for large instruments, and the need for a trained technician to operate them. However, they can also help clinicians get clearer images of diseased parts so that the right therapy can be chosen. However, the related biotoxicity complexity of these functionalized materials still restricts the application prospects. In contrast, some rare earth doped luminous materials are used for in-vivo imaging detection [108, 109]. In that case, the pertinent studies of *in-vitro* tumor marker diagnostics show significant importance for cancer assessment.

As the gold standard for cancer in-vitro diagnostics, tissue biopsies are currently largely indispensable for identifying tumor features. However, this technique will result in traumatogenic sampling and intricate pathological tissue analysis, which limits its potential uses [110]. The enzyme-linked immunosorbent assay (ELISA) is usually treated as a gold standard for proteins detection. Although the ELISA is more practical for the identification of associated tumor marker proteins, its point-of-care application for tumor marker diagnostics is limited by some time-consuming and technical operational drawbacks [111]. Moreover, the lateral flow assay (LFA) strip can be also used for point-of-care tumor marker proteins detection [112]. Its application scenarios are expanded by its exceptional simplicity and convenience, but the issues with relatively poor detection sensitivity still need to be fixed. Although blood samples are frequently utilized for related tests involving the tumor marker protein detections of ELISA and LFA, the process of obtaining blood samples is intrusive and carries some risk of infection. On the other hand, saliva samples are essentially noninvasive and easy to obtain, making them ideal for point-of-care tumor marker testing [113-115]. For example, the Indian Institute of Technology's Kaur et al. discovered a relevant biomarker of IL-6 and IL-8 in saliva samples for the identification of oral cancer [116]. According to earlier studies, spit samples include about 99.5% water, and the quantities of associated tumor markers are significantly lower than those in blood samples. This suggests that saliva is important for high sensitivity tumor marker identification.

With their broad excitation wavelengths, narrow emission profile, better illumination properties, and relatively high photoluminescence quantum yield, the quantum dots (QDs) exhibit exceptional photoluminescence capabilities [117-121]. Because of their notable luminous properties, QDs have been used in the field of in-vitro biomarker identification [83, 122, 123]. For example, Prof. Chan et al. used the modified fluorescent QDs for highly sensitive genetic target detection and multiplexed pathogen biosensing [124]. Additionally, the sandwich structure conjugation fluorescence immunoassay is widely used for the diagnosis of in-vitro biomarkers, where luminous nanoparticles are used for the optical sensing of the targeted biomarkers [125-128]. As a functionalized microdevice, the microfluidic biochip has a variety of designed channels with certain properties that allow the regulated fluids to flow via different micro-channels and create pertinent interactions with external systems beneath the intake and outlet. The flexibility of application, programmable capability, and biology applicability of microfluidic biochips are among their many benefits, which significantly enhance the integrated and convenient performance of the point-of-care biosensing platform [129-132]. In addition, the emerged machine vision technology is considered as one type for the digital technology, which is employed for objective perception and visual performance simulating of human beings [133-135]. As computer science development, the machine vision algorithms can provide relatively rigorous and trustworthy test results under quick programs for processing and analyzing digital images that have been acquired. This is extremely helpful for the development of intelligent point-of-care biosensing platforms [136, 137]. Additionally, the use of robust computing may manage and remove potential outliers or errors in the data collected, greatly enhancing the precision and quantifiable capabilities of the biosensing platform that is being created [137]. In order to realize the integrated, practical, and intelligent point-of-care biosensing platform for in-vitro tumor markers diagnostics, it is crucial to combine these wonderful superiorities and weigh the current benefits and drawbacks.

4.2 Experimental section

4.2.1 The conjugation of QDs carboxylated with antibody

The EDC (3 mg) and NHS (6 mg) were added to QDs (200 μL) and were stirred for 30 min. Then, the QDs were precipitated and redispersed in PBS. 0.1 mg of antibody was added to the suspension and stirred for another 2.5 h to ensure a complete coupling reaction. The antibody conjugated QDs was collected by high-speed centrifugation and washed with water three times.

4.2.2 The conjugation of PS microspheres with antibody

First, 1mg of carboxy group modified PS microbeads were distilled in 1 mL MES. 10 μL of 10 mg/mL EDC/NHS was added, and the solution was stirred for 30 min. Then, the PS microbeads were precipitated and redispersed in PBS, with the addition of 0.3

mg of Antibody in 800 µL PBS. The mixture was incubated for 2.5h. After the reaction, 5mg/mL of BSA was added and incubated for another 1 hour. The resultant antibody-conjugated PS microbeads were washed and resuspended in PBS for further usage.

4.3 Characterization and discussion

4.3.1 The mechanism of *in-vitro* tumor marker biosensing platform

To achieve the point-of-care tumor marker noninvasive detection, an intelligent biosensing platform was designed and fabricated as shown in Figure 38. Briefly, several prepared reagents are mixed and incubated for luminescent QDs conjugation, the captured images of microfluidic biochips are uploaded to the cloud, and test results are acquired in the smartphone via some relevant machine vision algorithms process and analysis. Among them, the excellent luminescent performance of QDs, functionalized microfluidic biochips, and cloud-based machine vision algorithms are of great significance for this elaborate biosensing platform.

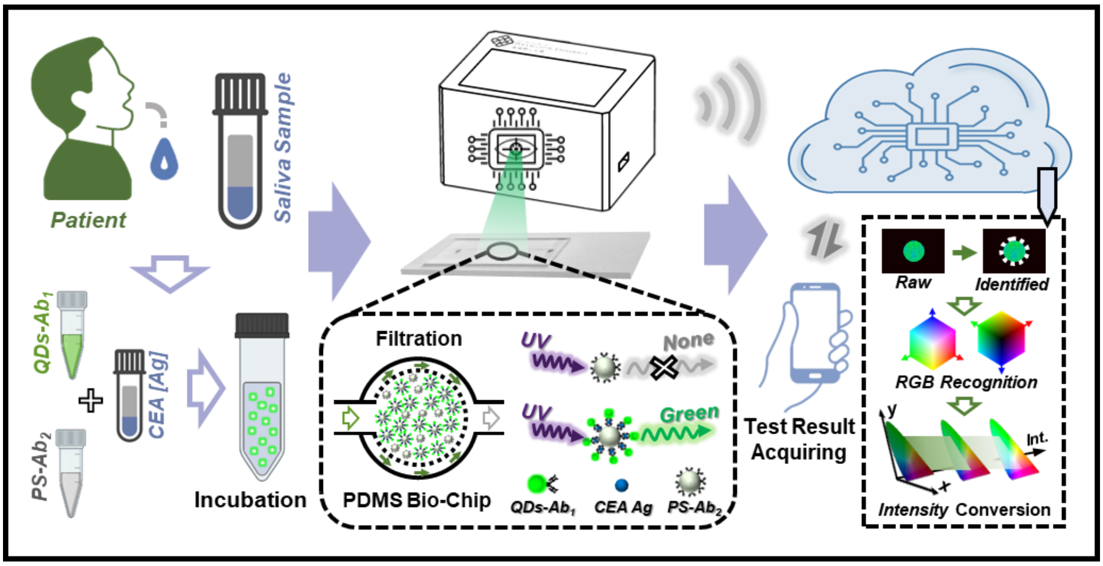

Figure 38. The schematic diagram of tumor marker *in-vitro* detection platform.

In detail, the saliva samples containing tumor markers (CEA) are collected from patients, and mixed with prepared QDs-Ab$_1$ and PS-Ab$_2$ adequately to incubate for conjugation onto the surface of PS microspheres within fifteen minutes. Next, the conjugated PS microspheres are injected into a designed and fabricated PDMS-based microfluidic biochip with separation function. Due to this designed function, unconjugated QDs-Ab$_1$ will flow through the filtration zone of the biochip and PS microspheres will stay and remain in the filtration zone of microfluidic biochip. After the UV light irradiation, unconjugated PS microspheres exhibit non-luminescent properties, however, the QDs conjugated PS microspheres present bright green emission as illustrated in the dashed box of Figure 38. Subsequently, the optical images of microfluidic biochips are captured and uploaded to the cloud through WIFI signal transmission. Then, the related images are recognized and analyzed via some machine vision algorithm for investigation and evaluation of tumor marker. At last, the corresponding test results are acquired in the portable smartphone. Combined with these above capabilities and preponderances, the well-designed intelligent biosensing platform is expected for potential application in point-of-care tumor marker diagnostics fields.

4.3.2 Microscale morphology investigations of QDs and PS microspheres

The transmission electron microscope (TEM) image of CdSe/ZnS QDs is shown in Figure 39a, which illustrates that the QDs possess uniform morphology. As shown in Figure 40a, the average particle size of QDs is around 11 nm from the particle size distribution diagram. The top insets of Figure 39b illustrates the high-resolution transmission electron microscope (HR-TEM) images of CdSe/ZnS QDs. It can be observed the excellent crystallinity of QDs and the lattice fringes are also clear and distinct, which exhibits the visible fast Fourier transform (FFT) patterns. The related scanning transmission electron microscopy (STEM) images with bright field (BF) and dark field (DF) are investigated as exhibited in the bottom insets of Figure 39b, which preliminarily indicates the core-shell structure of CdSe/ZnS QDs.

The crystalline structure investigation of X-ray diffraction spectrum is shown in Figure 40b. These obvious diffraction peaks of XRD indicate the core-shell construction of QDs, which is also similar with some previous research works [138, 139]. Besides, as shown in Figure 41-42, the spectra and mapping of energy dispersive X-ray (EDX) analysis further demonstrate the core-shell form of QDs.

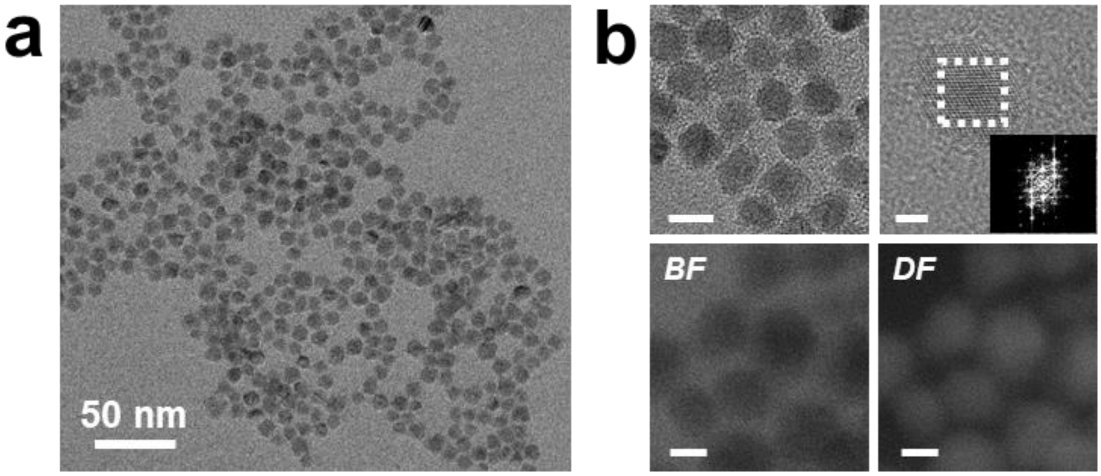

Figure 39. (a) TEM image of core-shell CdSe/ZnS QDs. (b) HR-TEM images (top) of QDs (scale bar: 10 nm) and relevant inset showing the FFT diffraction pattern (scale bar: 3 nm). STEM images (bottom) under the bright or dark field (scale bar: 5 nm).

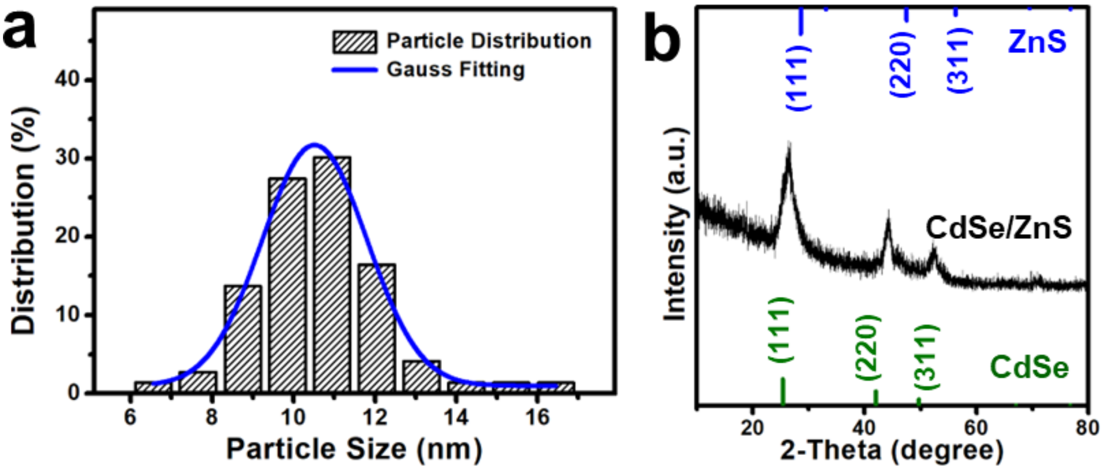

Figure 40. (a) The particle sized distribution histogram of CdSe/ZnS QDs and related Gauss fitted curve. (b) The XRD spectra of core-shell CdSe/ZnS QDs.

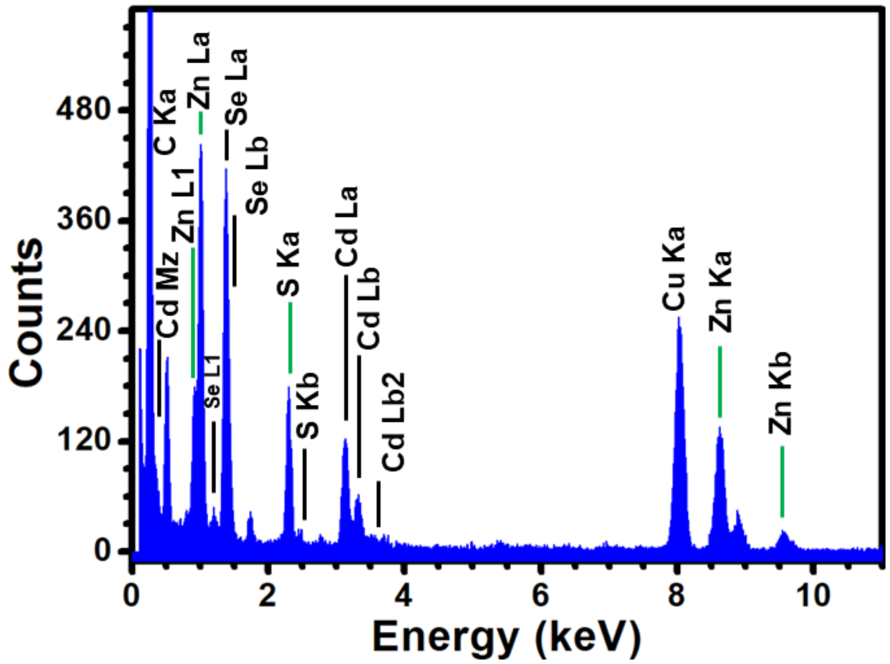

Figure 41. The EDX spectra of core-shell CdSe/ZnS QDs in TEM samples.

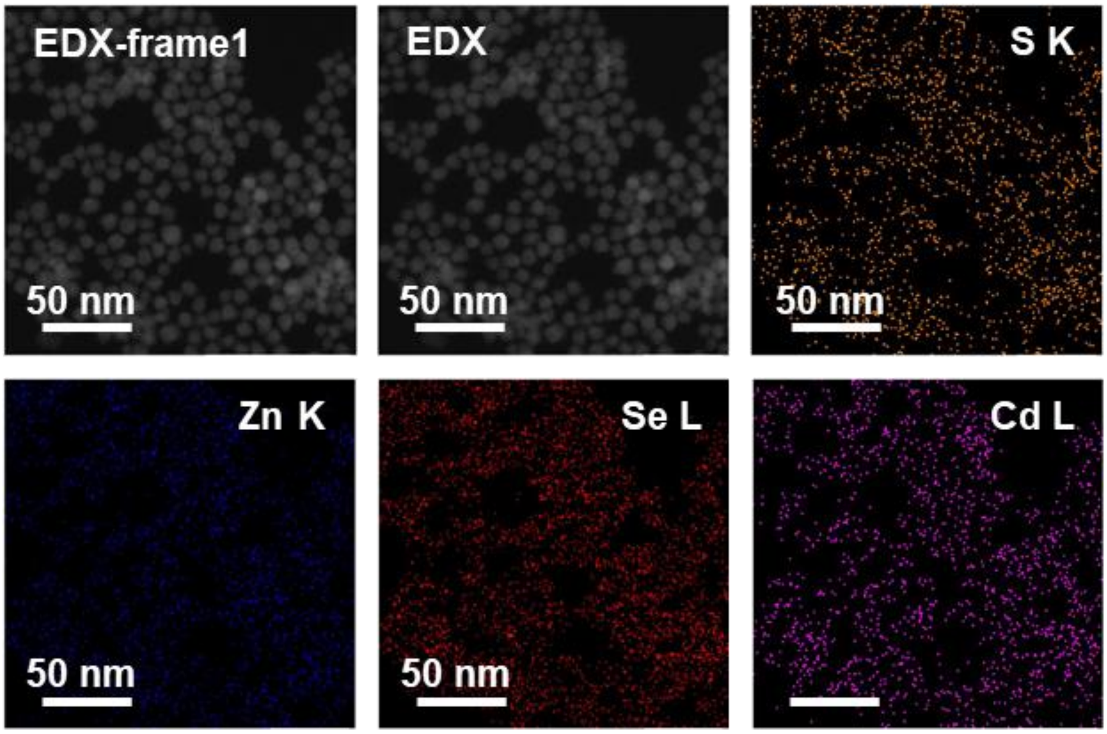

Figure 42. The related EDX elements mapping of CdSe/ZnS core shell QDs.

Moreover, the relevant morphology of PS microspheres is studied in Figure 43 and 44a. The image of PS microspheres as shown in Figure 43 illustrates that the microspheres are evenly distributed with a uniform size of around 50 μm. The scanning electron microscope (SEM) images as shown in Figure 44a further investigate the conjugation situation of QDs onto the surface of PS microspheres with or without CEA tumor markers. It can be observed from the up-insets of Figure 44a that the QDs are connected to the surface of PS microspheres after related CEA tumor markers conjugation.

On the other hand, when there is a bare of CEA tumor markers conjugation, the surface of PS microspheres is relatively clean exhibited in the down-insets of Figure 44a. Due to the destructive effect of electron beams from corresponding electron microscope methods, the atomic force microscope (AFM) with hardly damaging performance for biomedical samples was employed for the morphology investigation of the CEA tumor marker proteins and relevant antibodies as shown in Figure 44b. It can be seen that the CEA proteins connect well with the corresponding antibodies, which is beneficial for the sandwich structure formation of QDs, CEA tumor markers, and PS microspheres.

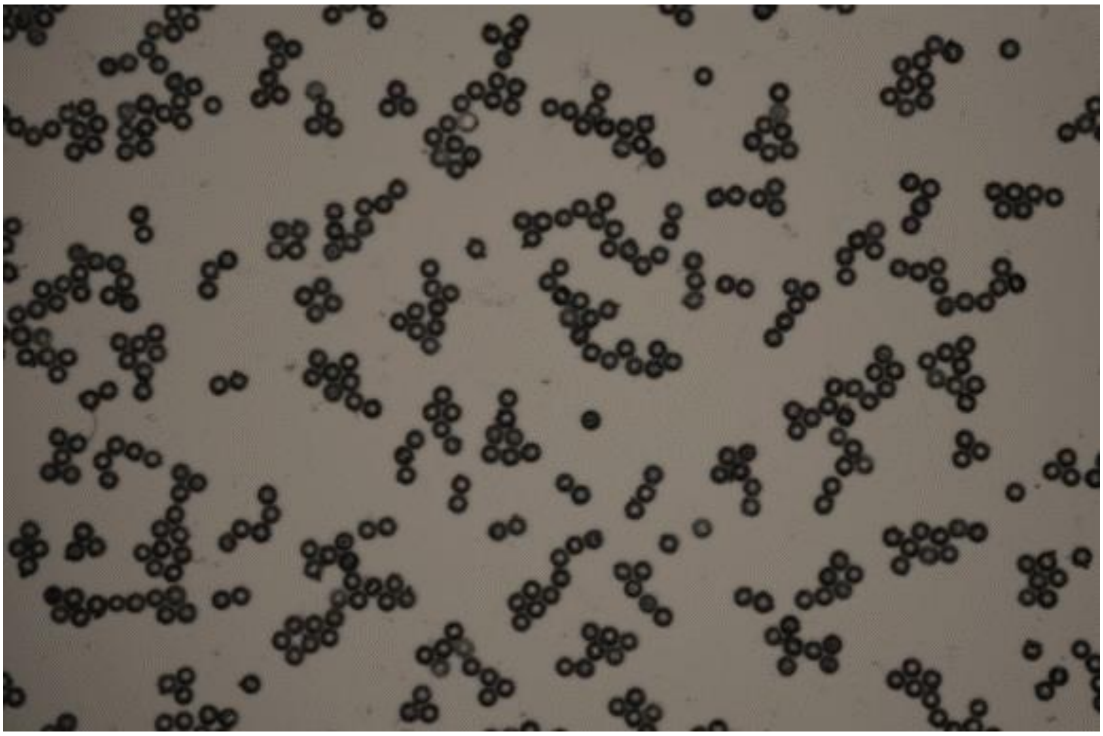

Figure 43. The relevant image of PS microspheres under the reflection mode of light microscope.

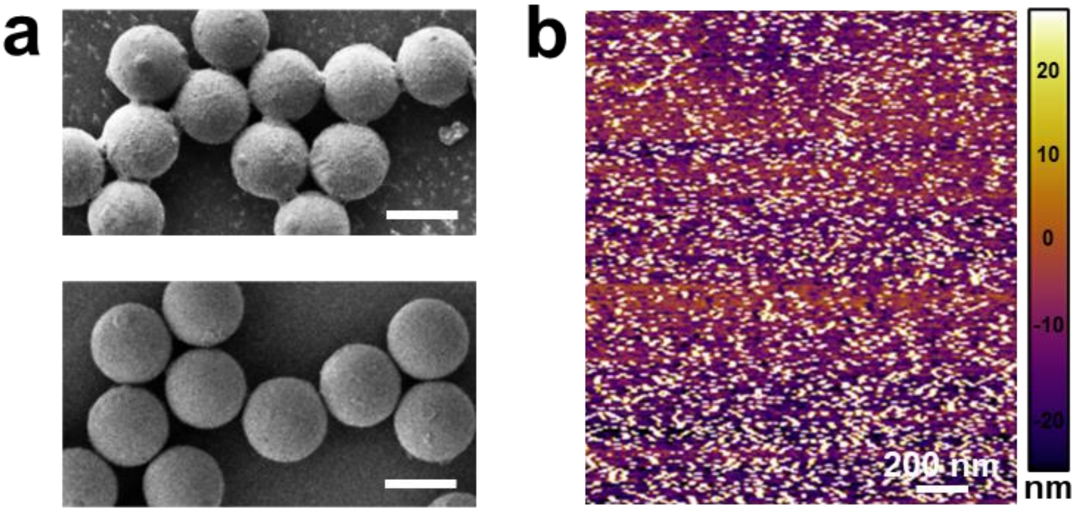

Figure 44. (a) The SEM images of PS microspheres with (up) and without (down) CEA protein conjugation. The scale bar is 50 μm. (b) AFM images of CEA proteins with conjugated antigen and antibody.

4.3.3 Surface modification research and photoluminescence property

As can be observed from Figure 45a, the investigation of zeta potential additionally demonstrates the modification performance of antibodies onto the surface of QDs and PS microspheres. It can be observed that the values of zeta potential for QDs decreased from -25.2 to -8.6 mV after the connection of antibody. And the related zeta potential of PS microspheres also decreases from -60.3 to -20.5 mV because of the antibody modification. The above values variation of zeta potential further indicates that the targeted antibodies are conjugated commendably onto the surface of QDs and PS microspheres.

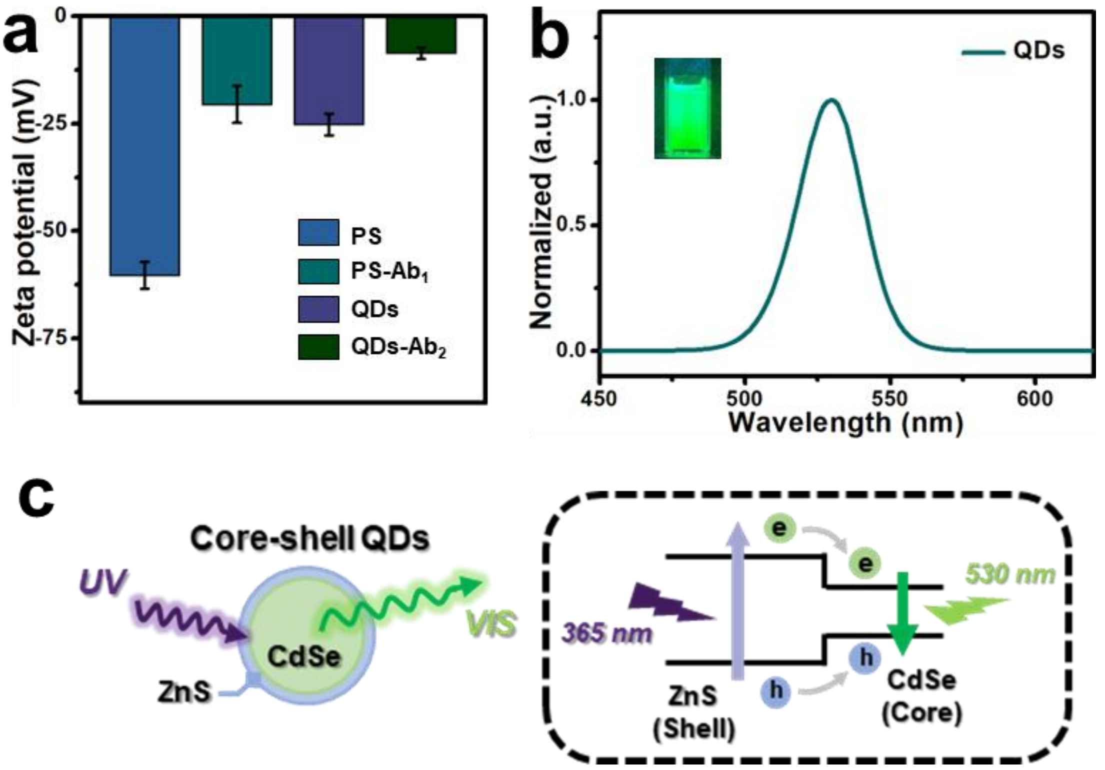

Figure 45. (a) The Zeta potential histogram of PS microspheres and QDs with and without antibody modification. (b) The PL emission spectrum of QDs under UV (365 nm) excitation. The left inset is related optical image of QDs. (c) Schematic illustration of the luminescent processes for core-shell QDs under UV irradiation.

Moreover, the relevant photoluminescence performances of QDs were studied in Figure 45b. Under UV (365 nm) light irradiation, the emission spectrum of CdSe/ZnS QDs is measured at the wavelength range from 450 to 625 nm. It can be observed that the emission peak is located at around 530 nm demonstrating a bright green color emission as exhibited in the inset of Figure 45b, which implies a potential application for posterior CEA tumor marker detection. The schematic illustration of a probable optical process for CdSe/ZnS QDs is presented in Figure 45c. When the UV light is exposed to the core-shell CdSe/ZnS QDs, it will emit photons with visible wavelength as shown in the top inset of Figure 45c. The fundamental optical process starts with the absorption of UV (365 nm) incident photons, in which high energy photons might generate the related electron-hole pairs primarily in the shells of QDs [140]. Subsequently, the created electrons and holes relax fleetly to the band-edge states confining within the core of QDs. Ultimately, the electron-hole pairs recombine radiatively and give rise to the green (530 nm) emission photons [141].

4.3.4 Studies of separating and cleaning abilities for employed biochip

The designed and fabricated microfluidic biochips were employed for separating unconjugated QDs and concentrating the luminescent conjugated PS microspheres, which played a vital role in the well-designed biosensing platform for CEA tumor markers diagnostics. As shown in Figure 46, the AutoCAD design layout of microfluidic biochip indicates that the incubated mixtures will be injected from the inlet and flow to the functional zone subsequently. After that, the unconjugated QDs with the particle size of around 11 nm will be filtrated to the outlet of fabricated microfluidic biochip. On the contrary, the PS microspheres with grain diameter of about 50 μm are retained and concentrated in the separation zone of biochip with filtrated pillar gap of 30 μm.

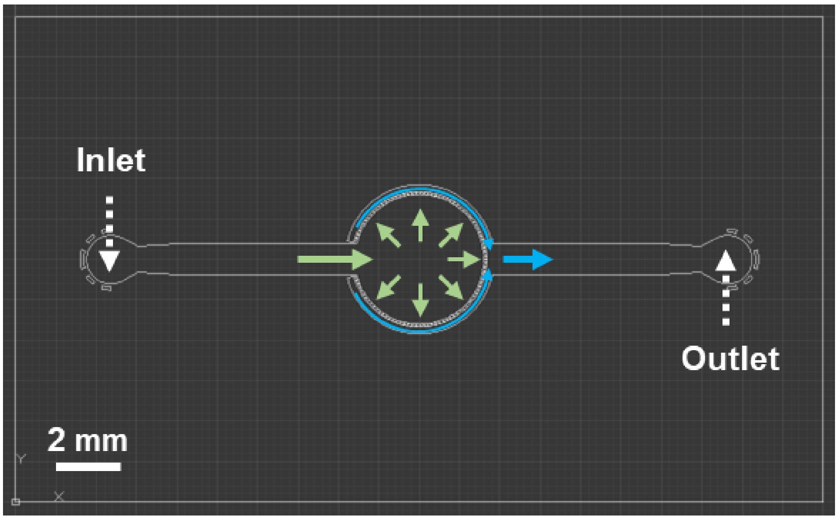

Figure 46. The layout of AutoCAD design for prepared microfluidic biochip and related flow direction.

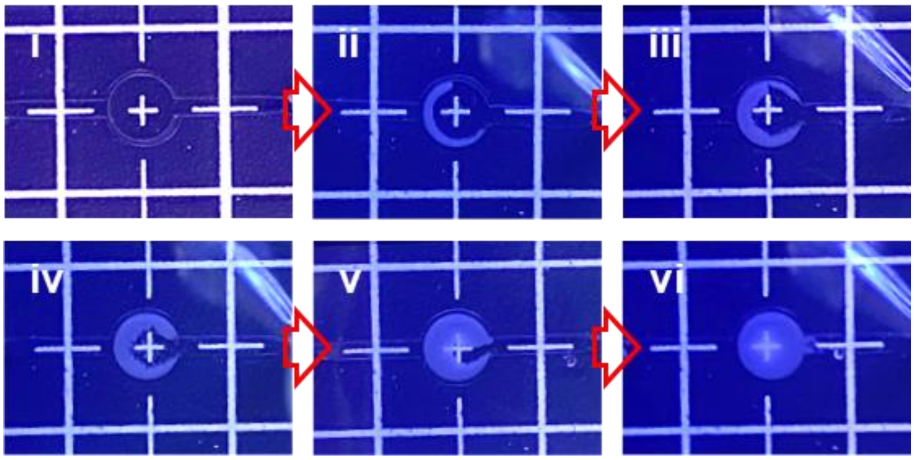

Figure 47. The pictures of microfluidic biochip concentrating property from (i) to (vi) insets.

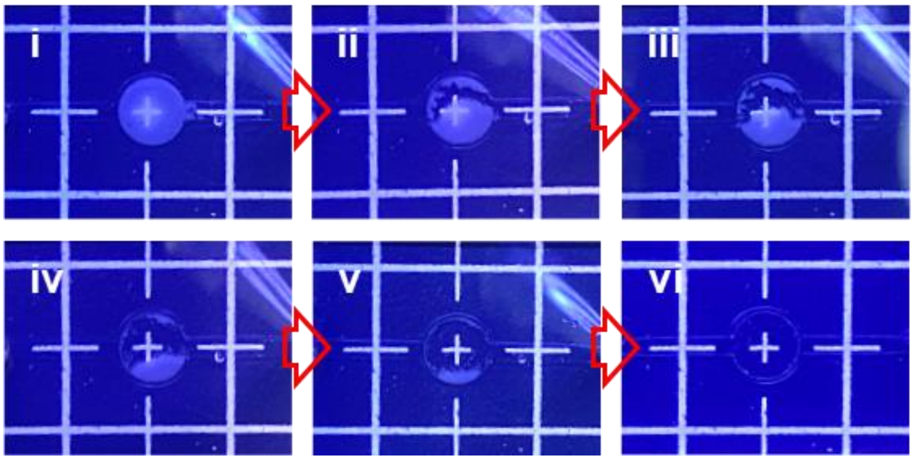

Figure 48. The photos of cleaning performance for microfluidic biochip from (i) to (vi) insets.

Moreover, the designed microfluidic biochip possesses filtration and cleaning performances as shown in Figure 47 and 48. Specifically, the related optical images of separation process are illustrated in Figure 47. It can be seen that the PS microspheres are filtrated and concentrated in the filtration zone of microfluidic biochip gradually. From relevant cleaning process images of biochip as shown in Figure 48, the PS microspheres will be washed via injecting of flushing liquid. The corresponding cleanable performance of designed microfluidic biochip brings about the advantage of cost reduction, which improves the application potential for tumor markers detection area.

In addition, the Figure 49 exhibit the optical images of PS microspheres in the filtration zone of microfluidic biochip with or without CEA tumor markers conjugation. A green luminescence from concentrated PS microspheres can be observed after the CEA conjugation, which further implies the QDs conjugation onto the surface of PS microspheres.

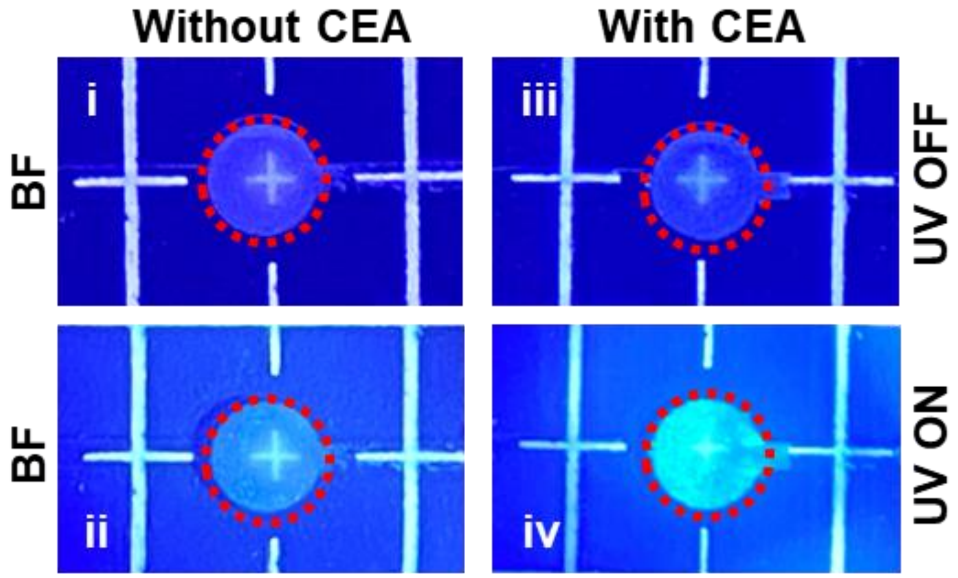

Figure 49. The corresponding optical image for microfluidic biochip with or without CEA conjugation under the UV-on or UV-off in bright field.

4.3.5 Tumor marker diagnostic performance of biodetection platform

As shown in the Figure 50a, it exhibits the normalized PL emission spectra with various concentrations of CEA tumor markers. With the increase of CEA concentration, the PL emissions exhibit a rising tendency, which can be attributed to the increased amount of the QDs conjugated onto the surface of PS microspheres. And it can be also observed that the PL intensity increases tardily at the high CEA concentration region. The variation of normalized peak intensity with different concentrations of CEA tumor markers is illustrated in Figure 50b in the range from 0.01 to 50 ng/mL. The related data points of normalized intensities exhibit a growth trend with the addition of CEA concentration.

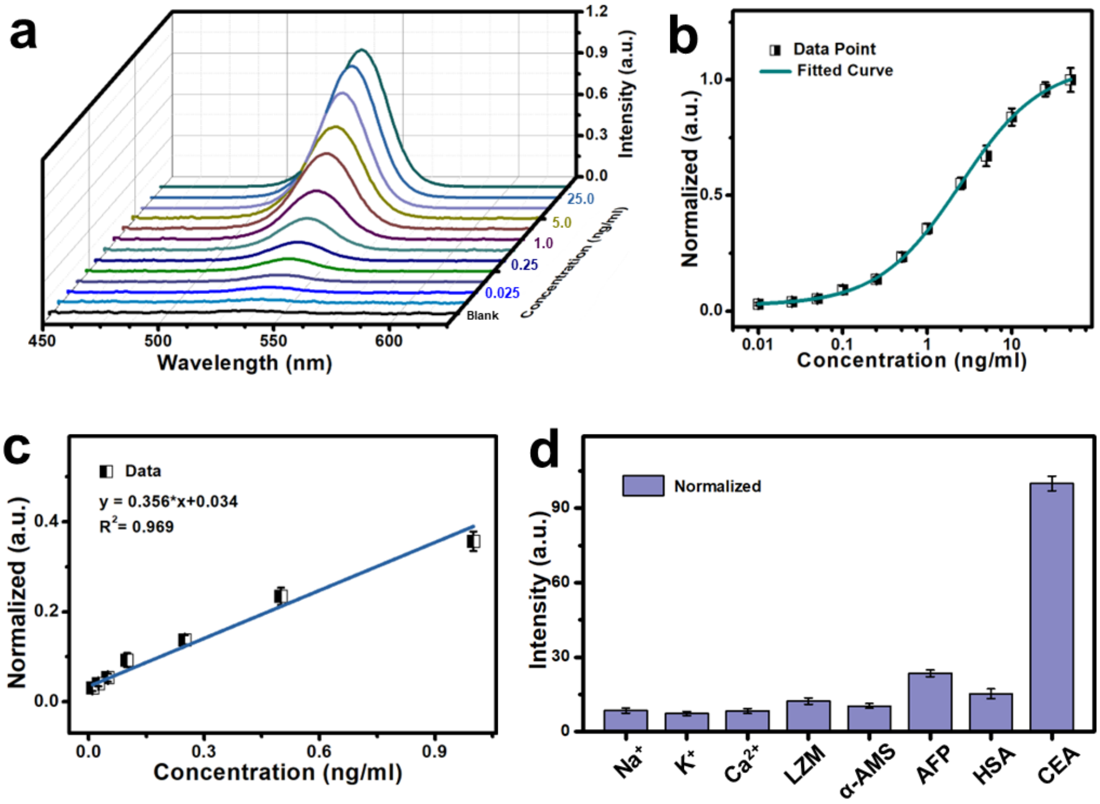

Figure 50. (a) The emission spectra of filtrated PS microspheres connected with QDs with different concentrations of CEA conjugation. (b) Normalized intensity of microfluidic biochip with various CEA connections and related fitting curves. (c) The linear relationship for conjugated and separated PS microspheres in microfluidic biochip for CEA protein detection. (d) Specificity test of CEA detection against related

interfering objects.

Among them, the intensity values are normalized under the maximum intensity set as 1.0 standardly. It can be seen that at a low CEA concentration region, the growth trend of normalized intensities tends to be tardiness, which probably originates from the unspectacular QDs conjugations onto the surface of PS microspheres. At the high CEA concentration range, we can also observe a similar trend as the further increase of CEA tumor markers, which can primarily result from the PL intensity saturation of QDs conjugation. As shown in Figure 50c, the normalized intensity increases linearly as the addition of CEA tumor marker concentration at the range from 0.01 to 1.0 ng/mL. From some previous researches, the detection limitation was assessed via concentration related with blank sample plus three times of standard deviation [142-144]. After corresponding calculation, the detection limitation was determined as 0.021 ng/mL for the fabricated biodetection platform. This excellent detection sensitivity implied an advantageous application potential for the CEA tumor marker diagnostics. Besides, the relevant investigations of specificity are also significant to evaluate the selection capability of biosensing platform for specific objectives [145-147]. As illustrated in Figure 50d, some important targets involving Na^+, K^+, Ca^{2+}, lysozyme (LZM), α-amylase (α-AMS), alpha-fetoprotein (AFP), human serum albumin (HSA), and CEA were tested for specificity study. It can be observed that the normalized intensity of CEA test exhibits higher value compared with other targets, implying a well diagnostic specificity for this designed CEA tumor marker biosensing platform. The corresponding investigations of tumor marker diagnostic properties demonstrate that this elaborately designed biodetection system possesses enormous potentiality for the future tumor marker diagnostic application.

4.3.6 Point-of-care biosensing system and related machine vision algorithm

In order to realize the point-of-care noninvasive tumor marker diagnostics, an intelligent biosensing platform involving QDs luminescence, microfluidic biochip, and machine vision algorithm was designed and manufactured as shown in Figure 51. The related schematic illustration of designed intelligent biosensing platform is exhibited in Figure 51a, which consists of touch screen, portable power supply (PPS), microfluidic biochip, UV (365 nm) LED, black flake, optical lens, light filter, CMOS image sensor, single chip microcomputer (SCM), cloud computing, and smartphone. Among these components of the well-designed biosensing platform, the touch screen was utilized for detection command operation. The PPS with a high battery capacity was selected as the power source for relevant electronic components for a longer running time. The PDMS-based microfluidic biochip was designed and fabricated for separation and concentrating functions. The small accessory of black flake with a circle hole was employed to block some unexpected stray light. The 365 nm UV LED was utilized for incident light providing, which can give rise to a green emission of concentrated and conjugated PS microspheres.

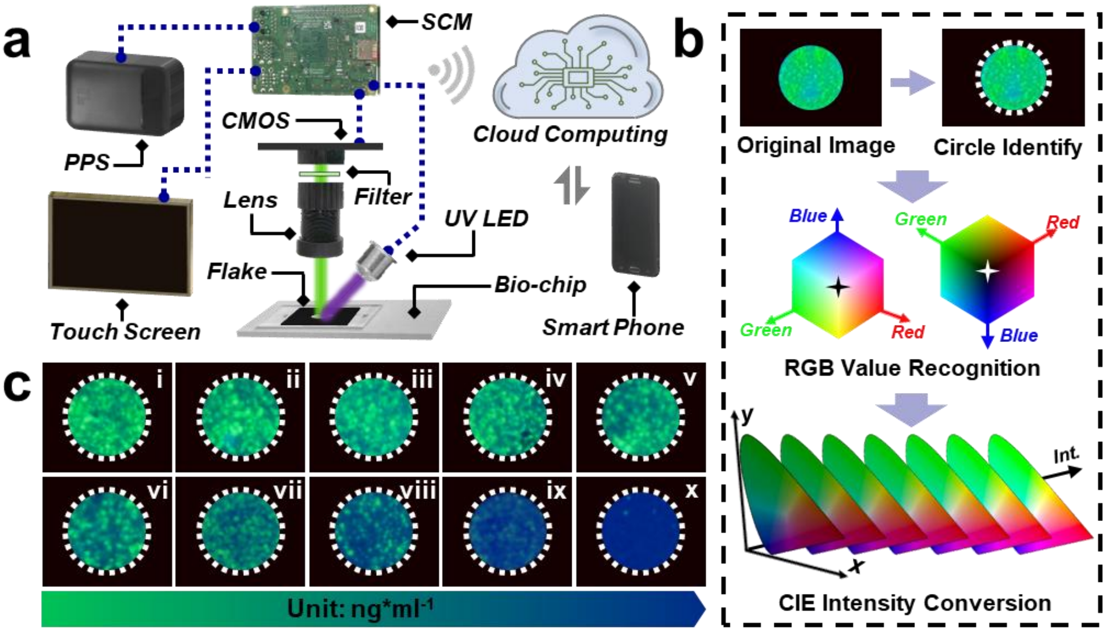

Figure 51. (a) Schematic illustration of point-of-care intelligent biosensing platform with various components. (b) Image recognition workflow of the adopted machine vision algorithm. (c) The optical pictures of microfluidic biochips in separated zones with different CEA concentrations.

In addition, the optical lens and filter were utilized to focus and filter the emission light. The CMOS component was employed for relevant optical image capturing, which possessed several preponderances involving power saving, fast image processing speed, and affordable cost compared with some conventional CCD image sensors. The significant advantage of CMOS image sensor is its power-saving capability over CCD image sensor, which brings about meaningful influence for the application of point-of-care biosensing platform. Besides, the corresponding program management involving data coding, signal processing, and information transmission was carried out in the integrated SCM. The cloud computing was utilized for executing related machine vision algorithms and the corresponding test results of tumor marker diagnostics were obtained via the smartphone mobile terminal.

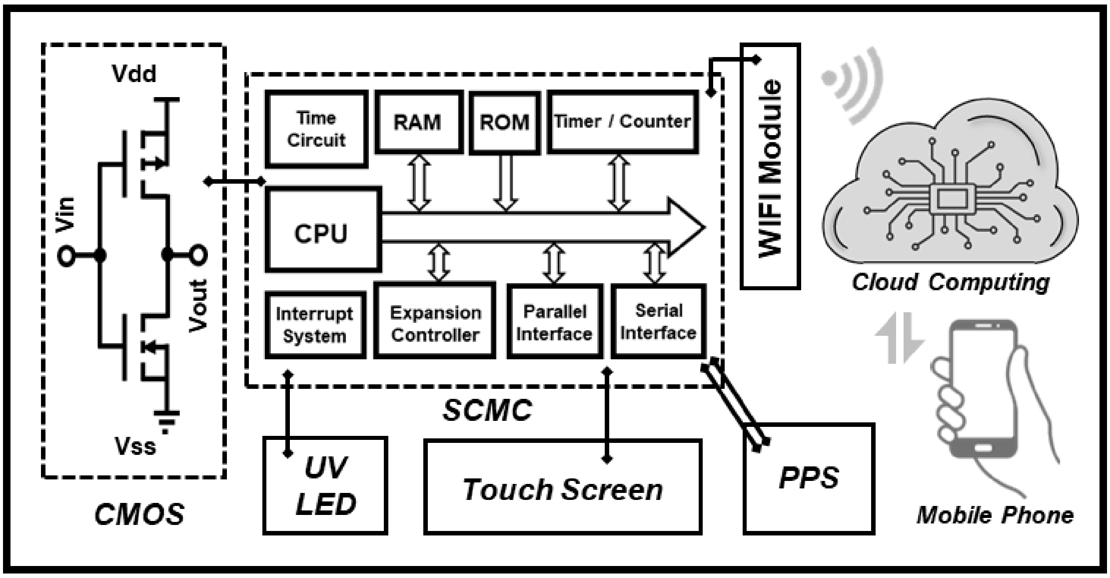

Figure 52. The flow chart of the manufactured biosensing platform for CEA detection combined with cloud computing and mobile phone results obtain.

The workflow chart of this designed intelligent biosensing platform is illustrated in the Figure 52 for CEA tumor marker detection. Meanwhile, the measurement of absorbance spectra for PDMS-based microfluidic biochip, as exhibited in Figure 53, indicates that there is almost no absorption for this fabricated biochip in the wavelength of nearby 365 nm, which implies the appropriate usage of PDMS base material for designed microfluidic biochip. Among these components, the CMOS image sensor is one of the significant components, which converts optical signals to electronic signals. Then these obtained images will be uploaded to the cloud by an integrated WIFI module for further photo processing. The reason for this design is that it can reduce the related cost of portable devices for image processing and analysis because they are relatively expensive for the SCM and corresponding electronic accessories with eminent image processing ability and interaction capability with mobile terminals. On the other hand, it will also take up a large space for biosensing platform, which restricts the point-of-care applications for tumor markers diagnostics. In that case, the crucial procedure of image processing was implemented in the cloud, which will bring about excellent benefits like cost reduction and efficiency improvement.

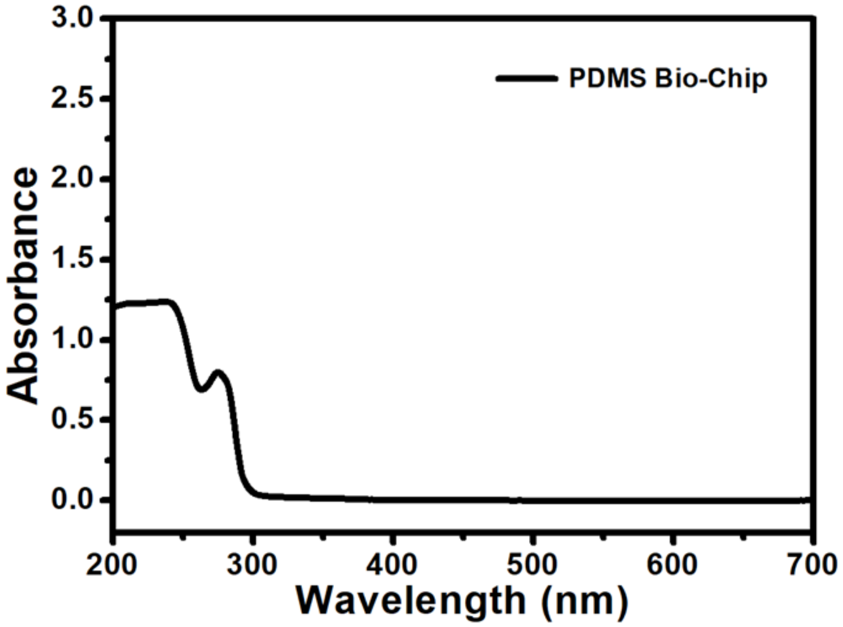

Figure 53. The absorbance spectrum of PDMS-based microfluidic biochip.

For purpose of accomplishing the point-of-care tumor marker diagnostics, the Python-based machine vision algorithm was developed and employed for acquired image recognition and processing. As shown in Figure 51b, the original image was processed for luminescent circle identification via the algorithm. Subsequently, this Python-based machine vision algorithm will automatically recognize and extract the related luminescent points RGB values in the identified circle image. Ultimately, the extracted RGB values in RGB color cubic space will convert into CIE values (x, y, Y) for further image analysis, which manifests that each recognized luminescent circle image corresponds to a data point in the CIE xyY color space. According to previous research works, the luminance and intensity of emission light is relatively equivalent in the CIE xyY color space, and the chromaticity values (x, y) are determined by the emission light wavelength [148]. Due to the independent characteristic for luminance and wavelength of emission light, the CIE-intensity (Y) will not be influenced by the chromaticity values (x, y) of CIE xyY color space [148]. Regarding to this designed QDs luminescence sandwich immunoassay structure for CEA tumor marker detection, the wavelength and intensity of emission spectra is mutually independent, as illustrated in Figure 50a and 50b, the intensity of emission spectra changes with the variation of CEA tumor marker concentrations. In that case, the CIE-intensity (Y) value was employed for evaluating the microfluidic biochip image signal intensity performance.

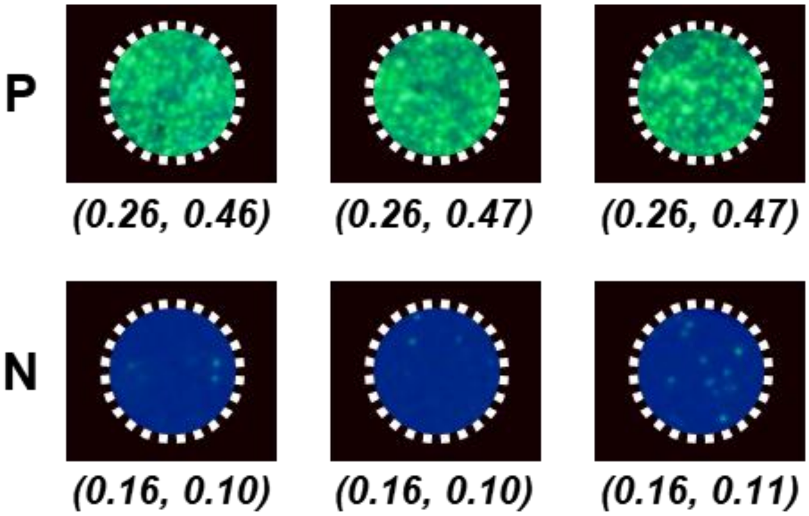

Figure 54. The acquired optical images of CEA tumor marker positive (P) or negative (N) samples and their corresponding average CIE (x, y) values.

The positive (with CEA proteins) samples and negative (without CEA proteins) samples were investigated in this designed intelligent biosensing platform as shown in Figure 54 to 56, and related captured optical images were processed and analyzed via the Python-based machine vision algorithm. As exhibited in Figure 54, it can be observed that negative samples and positive samples were automatically recognized via this machine vision algorithm. The positive samples show bright green emission, nevertheless, the negative samples exhibit unobvious emission light. Besides, the calculated average chromaticity values (x, y) of CIE xyY color space were illustrated, which demonstrates that the positive and negative samples possess disparate chromaticity values. These relevant and thrilling investigations imply that the Python-based machine vision algorithm can be utilized for the intelligent biosensing platform of CEA tumor marker detection.

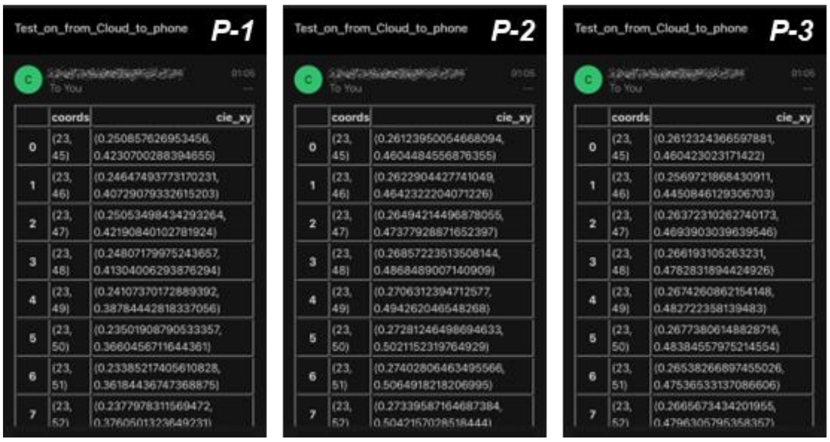

Test_on_from_Cloud_to_phone **P-1**

C [redacted] 01:05
To You

	coords	cie_xy
0	(23, 45)	(0.250857626953456, 0.4230700288394655)
1	(23, 46)	(0.24647493773170231, 0.40729079332615203)
2	(23, 47)	(0.25053498434293264, 0.42190840102781924)
3	(23, 48)	(0.24807179975243657, 0.41304006293876294)
4	(23, 49)	(0.24107370172889392, 0.38784442818337056)
5	(23, 50)	(0.23501908790533357, 0.3660456711644361)
6	(23, 51)	(0.23385217405610828, 0.36184436747368875)
7	(23, 52)	(0.2377978311569472, 0.3760501323649231)

Test_on_from_Cloud_to_phone **P-2**

C [redacted] 01:05
To You

	coords	cie_xy
0	(23, 45)	(0.26123950054668094, 0.4604484556876355)
1	(23, 46)	(0.2622904427741049, 0.4642322204071226)
2	(23, 47)	(0.26494214496878055, 0.47377928871652397)
3	(23, 48)	(0.26857223513508144, 0.4868489007140909)
4	(23, 49)	(0.2706312394712577, 0.494262046548268)
5	(23, 50)	(0.27281246498694633, 0.5021152319764929)
6	(23, 51)	(0.27402806463495566, 0.5064918218206995)
7	(23, 52)	(0.27339587164687384, 0.5042157028518444)

Test_on_from_Cloud_to_phone **P-3**

C [redacted] 01:05
To You

	coords	cie_xy
0	(23, 45)	(0.2612324366597881, 0.460423023171422)
1	(23, 46)	(0.2569721868430911, 0.4450846129306703)
2	(23, 47)	(0.26372310262740173, 0.4693903039639546)
3	(23, 48)	(0.266193105263231, 0.4782831894424926)
4	(23, 49)	(0.2674260862154148, 0.482722358139483)
5	(23, 50)	(0.26773806148828716, 0.48384557975214554)
6	(23, 51)	(0.26538266897455026, 0.47536533137086606)
7	(23, 52)	(0.2665673434201955, 0.4796305795358357)

Figure 55. The smartphone screen pictures of designed biosensing platform for relevant positive (P) samples CIE (x, y) values performance.

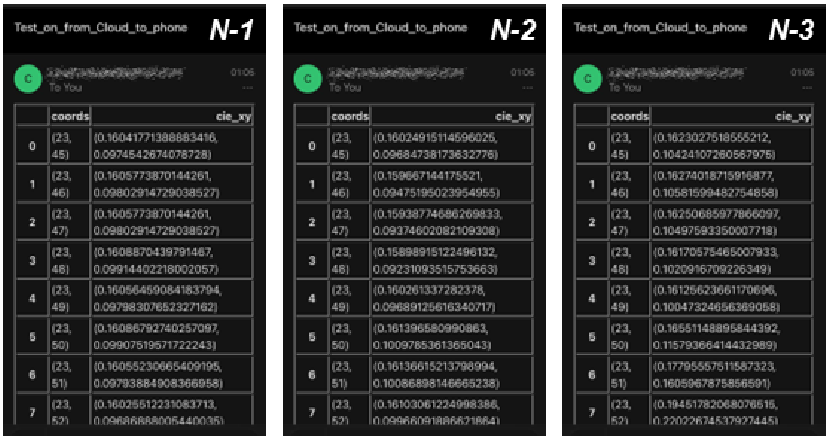

Test_on_from_Cloud_to_phone **N-1**

C [redacted] 01:05
To You

	coords	cie_xy
0	(23, 45)	(0.16041771388883416, 0.0974542674078728)
1	(23, 46)	(0.1605773870144261, 0.09802914729038527)
2	(23, 47)	(0.1605773870144261, 0.09802914729038527)
3	(23, 48)	(0.1608870439791467, 0.09914402218002057)
4	(23, 49)	(0.16056459084183794, 0.09798307652327162)
5	(23, 50)	(0.16086792740257097, 0.09907519571722243)
6	(23, 51)	(0.16055230665409195, 0.09793884908366958)
7	(23, 52)	(0.16025512231083713, 0.09686888005440035)

Test_on_from_Cloud_to_phone **N-2**

C [redacted] 01:05
To You

	coords	cie_xy
0	(23, 45)	(0.16024915114596025, 0.09684738173632776)
1	(23, 46)	(0.159667144175521, 0.09475195023954955)
2	(23, 47)	(0.15938774686269833, 0.09374602082109308)
3	(23, 48)	(0.15898915122496132, 0.09231093515753663)
4	(23, 49)	(0.160261337282378, 0.09689125616340717)
5	(23, 50)	(0.161396580990863, 0.1009785361365043)
6	(23, 51)	(0.16136615213798994, 0.10086898146665238)
7	(23, 52)	(0.16103061224998386, 0.09966091886621864)

Test_on_from_Cloud_to_phone **N-3**

C [redacted] 01:05
To You

	coords	cie_xy
0	(23, 45)	(0.1623027518555212, 0.10424107260567975)
1	(23, 46)	(0.16274018715916877, 0.10581599482754858)
2	(23, 47)	(0.16250685977866097, 0.10497593350007718)
3	(23, 48)	(0.16170575465007933, 0.10209167092226349)
4	(23, 49)	(0.16125623661170696, 0.10047324656369058)
5	(23, 50)	(0.16551148895844392, 0.11579366414432989)
6	(23, 51)	(0.17795557511587323, 0.1605967875856591)
7	(23, 52)	(0.19451782068076515, 0.22022674537927445)

Figure 56. The mobile phone screen photos of designed biosensing platform for related negative (N) samples CIE (x, y) values performance.

Furthermore, a series of microfluidic biochip luminescent images were obtained in the intelligent biosensing platform and processed by the machine vision algorithm for CEA tumor marker diagnostics. As shown in Figure 51c, it can be observed several optical images with different concentration of CEA tumor marker conjugation. With the decrease of concentrations, the luminescence intensity illustrates a decline trend. By means of the Grayscale and RGB color space investigations for these various obtained images, as shown in Figure 57a, the related intensities indicate a growth trend as the addition of CEA tumor marker concentrations. Among them, the corresponding intensities of Grayscale investigation increase relatively tardily as the increase of CEA tumor marker concentrations. The relevant intensities variation trend of G values for RGB color space exhibit better rising tendency but the related linear relationship manifests relatively poor as the growth of CEA tumor marker concentrations. On the other hand, as shown in Figure 57b, the calculated CIE intensities from the machine vision algorithm exhibit a better increase trend and quantitative relationship at the range from blank to 50 ng/mL of CEA tumor marker concentrations. The concentration cut-off value is determined as a relatively low intensity of 0.1 ng/mL, which implies a potential application for CEA tumor marker detection.

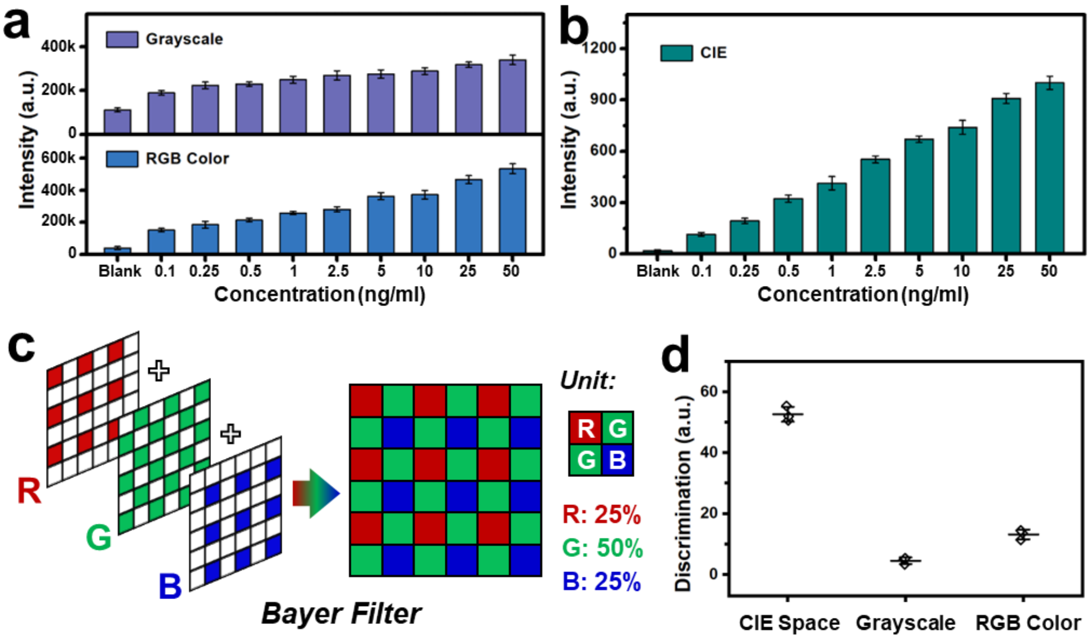

Figure 57. (a) The calculated Grayscale (top) and RGB (bottom) intensity for CEA detection via the intelligent biosensing platform. (b) CIE intensity for this intelligent biosensing system with different CEA concentrations. (c) Schematic diagram of Bayer filter utilized for CMOS electronic components. (d) The discrimination values of image recognition and analysis in various color spaces involving CIE Space, Grayscale, and RGB Color.

Besides, as mentioned above, the CMOS component is significant for the optical images obtained. Among this electronic component, the Bayer filter is commonly used in the commercial CMOS image sensor. The related schematic illustration is presented in Figure 57c, it can be observed that the Bayer filter involves three primary colors of red, green, and blue. The proportion of green color in a unit is 50%, twice than the other colors, which can be attributed the similar color sensitivity with human eye [149, 150]. This is also one of the other reasons for the selection of green emission QDs as a luminescent agent in the intelligent biosensing platform for CEA tumor marker diagnosis. In addition, the discrimination values of three different image analysis were investigated in Figure 57d. The corresponding discrimination values were calculated from the ratio of luminescent intensities with blank samples and highest concentration samples. It can be observed that the relevant discrimination value of this algorithm system is much higher than the Grayscale and RGB color space methods, which implies the suitable adoption for the Python-based machine vision algorithm. Therefore, combining with all these corresponding advantages and performances, this well-designed intelligent biosensing platform is of great importance for the future point-of-care tumor marker diagnostics.

4.3.7 Preparation of artificial saliva samples containing human source CEA

The schematic diagram of procedures for artificial saliva solvent preparation is illustrated in the Figure 58, according to the common method reported by some previous studies [151, 152]. In details, the 5 mL volume of several aqueous solutions involving K_2HPO_4 (25 mM), $KHCO_3$ (1.57 M), Na_2HPO_4 (24 mM), $MgCl_2$ (2 mM), and NaCl (0.1 M) were mixed with 5 mL of $CaCl_2$ (0.15 M) and 3 mL of citric acid (25 mM) adequately. Then, the NaOH and HCl were utilized for adjusting to around 7.0 of the pH value. Next, the volume of mixture aqueous solution was expanded to 50 mL quantitatively. Subsequently, the enlarged mixture solution was sterilized via the autoclaving method. After the sterilized solution reached to a room temperature, 0.5 mL of aqueous solutions including α-AMS (1 g/L) and LZM (0.1 g/L) were added into the sterilized solution and continuous mixing for around half an hour. Ultimately, various concentrations of human source CEA tumor marker proteins were blended with the prepared artificial saliva for further detection performance investigations.

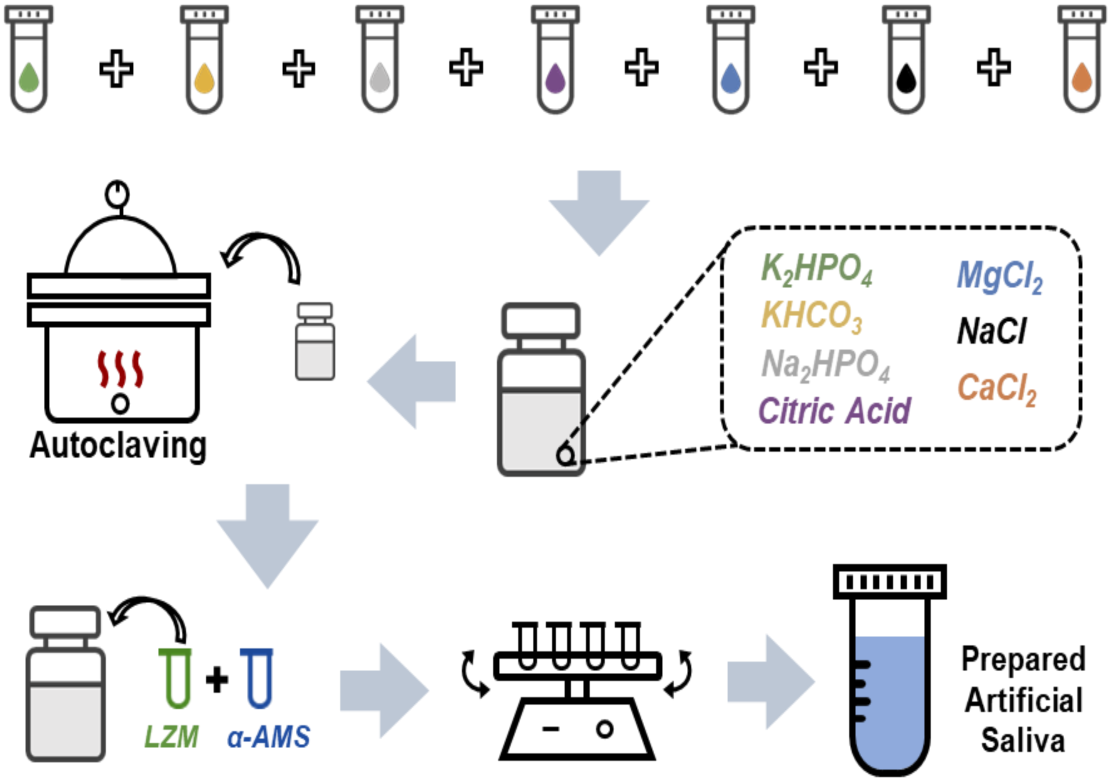

Figure 58. The schematic diagram for artificial saliva preparation.

4.3.8 Detection performance compared with typical LFA strips

Moreover, the potentially practical diagnostic performance was investigated for this designed intelligent point-of-care biosensing platform and a series of test samples involving purified human source CEA proteins and synthetic saliva solvent were employed for detection capabilities evaluation as shown in Figure 59. As shown in Figure 59a, the related optical images for two commercial LFA strips are illustrated with various CEA proteins addition. Among them, the top images exhibit the colorimetric LFA strips (LFA-1) with colloidal gold labeling, and the fluorescent LFA strips (LFA-2) are displayed in the bottom of Figure 59a. It can be observed that the test line of LFA strips present fuzzy and unclear performance with the decrease of CAE proteins concentration from insets of (VI) to (I). Ulteriorly, to further quantitatively analyze the detection properties of commercial LFA strips, the related optical pictures were converted into the corresponding grayscale images. As shown in Figure 59b, the test line selected areas of relevant LFA strips were managed basically at the parallel area values for better comparison of diagnostic capabilities.

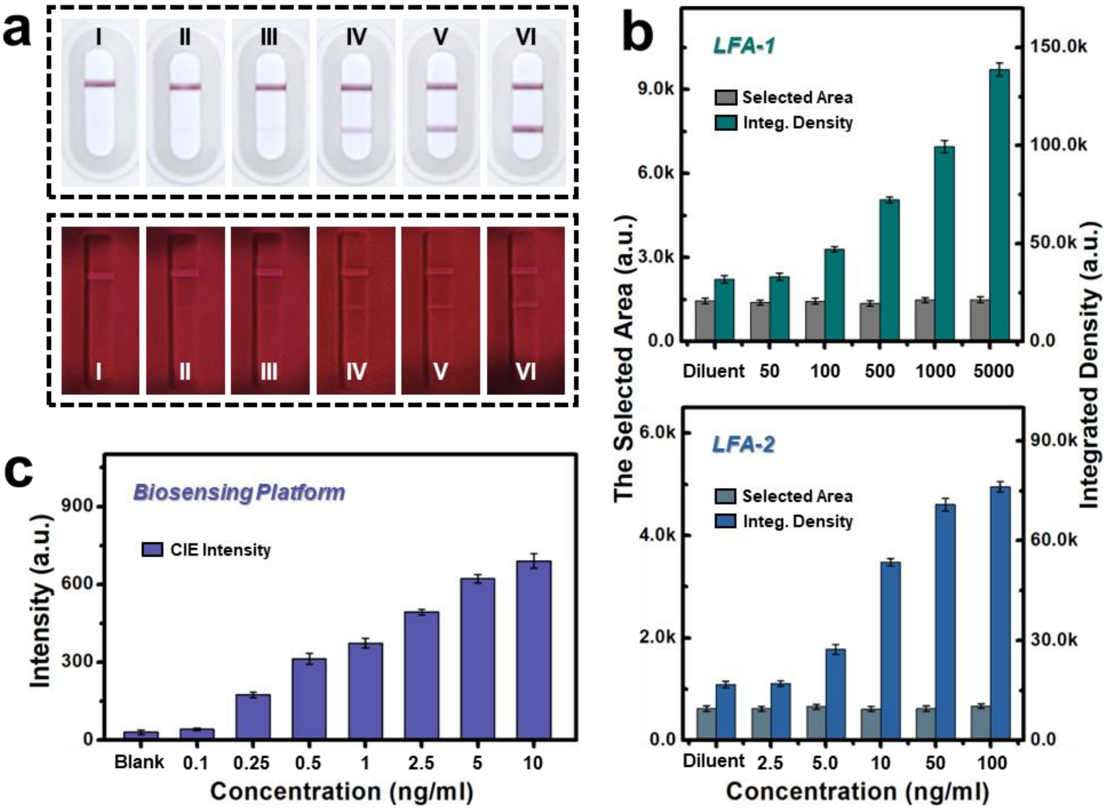

Figure 59. (a) The optical images of two commercial CEA tumor marker test strips including LFA-1 (top) and LFA-2 (bottom). (b) Histogram plot of related commercial test strips with LFA-1 (up) and LFA-2 (down) by gray values calculated from the selected area. (c) The column chart of CIE intensity for designed biosensing platform with diverse CEA tumor marker concentrations.

Regarding to LFA-1 test strips, the values of integrated density tend to descend as the decrease of CEA proteins concentrations. The relevant LFA strips indicate a relatively poor diagnostic property, and the detection cut-off value is estimated at about 100 ng/mL, which is similar to the correlative optical images shown in the top group insets of Figure 59a. In terms of LFA-2 strips, the corresponding values of integrated density indicate decrease trend as the reducing addition of CEA concentrations as well, which demonstrates a diagnostic cut-off value of around 5.0 ng/mL. In addition, as shown in Figure 59c, the designed intelligent biosensing platform was also employed to investigate the relevant CEA tumor marker saliva samples diagnostic performance. Similarly, as the increase of CEA proteins concentrations, the corresponding values of CIE intensity show growth trend. After related machine vision algorithm processing, the cut-off value is assessed about 0.25 ng/mL, which is better than the tested commercial LFA strips for tumor markers point-of-care diagnostics. This well-designed intelligent biosensing platform reveals tremendous advantages, which is expected for thrillingly potential application for point-of-care tumor markers diagnostics in the future.

4.4 Summary

In summary, an intelligent point-of-care biosensing platform based on microfluidic biochip and machine vision algorithm was developed and manufactured for CEA tumor marker detection. The uniform core-shell QDs of CdSe/ZnS with extraordinary luminescent properties were employed for the optical labelling indicator of the designed sandwich structure immunoassay. The elaborate microfluidic biochip with excellent filtrated and cleanable performance was utilized as a functional chamber accessory of the designed CEA tumor marker biosensing platform, which illustrated a prominent diagnostic sensitivity of around 0.021 ng/mL. The Python-based machine vision algorithm was developed and applied as the corresponding images recognition and analysis for expected point-of-care CEA tumor marker detection. Moreover, for the investigation of saliva samples practical application evaluation, the designed intelligent biosensing platform exhibited outstanding detection cut-off value comparing with some common-used commercial CEA tumor marker LFA test strips. As a result, considering of these thrilling and remarkable system design superiority and diagnostic abilities, this well-designed intelligent biosensing platform implies tremendous application potentiality for the future point-of-care tumor marker detection field.

Chapter 5 Hydrophobic SERS biochip based biosensing platform for α-syn protein biomarker detection

5.1 Introduction

Recent years, the emerging neurodegenerative diseases (NDDs) involving Parkinson's disease (PD), dementia with Lewy bodies, Alzheimer's disease (AD), amyotrophic lateral sclerosis (ALS), and Huntington's disease have drawn a great research attention for scientists worldwide [153-155]. These above unexpected NDDs are usually induced by the gradual degradation for nerve cells and abnormal proteins accumulation in the affected area of brain [156]. Owing to the complicated pathogenesis of these NDDs, the effective treatments for slowing or curing these diseases are still absent. Most of the NDDs begin around ten to fifteen years before the clinical symptoms of these diseases, however, there is still missing of some effective detection approaches for early evaluation or monitoring of NDDs. Moreover, as mentioned above, due to the relatively complicated properties including overlapping biomarkers and clinical heterogeneity of NDDs, the occurrence of misdiagnosed are common in practical detection [157].

Although various proteins are involved in the different NDDs, the protein of α-syn misfolding into the fibrillary form is considered as the typical mechanism for lots of NDDs especially for the relevant PD [158-160]. Therefore, it is vital for corresponding detecting of protein aggregation and structure variation to NDDs diagnosis. Besides, the thrilling information is that these proteins can be found in several body fluids of human being consisting of cerebrospinal fluid (CSF), blood fluid, and saliva fluid, which brings about advantages for conventional NDDs biosensing [161-163].

Currently, the related gold standards for NDDs biomarkers detection are mainly mass spectrometry (MS) and enzyme-linked immunosorbent assay (ELISA) methods. These diagnostic approaches are mainly concentrating into the quantifying detection for related proteins, which cannot be utilized for the identifying of different structure of NDDs proteins. Furthermore, the development of MS method like limited proteolysis-based MS is expected for the distinguishing the protein structure difference in some intricate samples [164]. But this arisen method is relatively the early stage and difficult for employing in the clinical areas. On the other hand, the ELISA method is the antibody-based detection approach. The current research for the studying of specific antibodies of different protein structures are full of challenges, which indicates that no existing antibodies can be utilized as for specific connection of different structure of α-syn protein currently [165-167].

The surface enhanced Raman spectroscopy (SERS) is a representative technique, which can be used to improve the Raman signals [168-170]. In details, the Raman signal is originated form the inelastic scattering of the incident laser interactions with the vibration molecular. In terms of the enhanced Raman signal, there are mainly two mechanisms involving electromagnetic enhancement and chemical enhancement, and the electromagnetic enhancement is the relatively typical one [171, 172]. Moreover, owing to these advantages of rapid, economy, and label-free, the SERS-based detection approaches, like SERS based biochip, are expected to be potential methods for the multiple related applications in the point-of-care biosensing area.

5.2 Experimental section

The PDMS based biochip for α-syn protein detection was fabricated via the two steps methods. In details, the first step is to manufacture the PDMS based biochip with pillar array and related hydrophobic performance. The corresponding layout of pillar array was designed via the AutoCAD software. And then the above AutoCAD designed pattern was utilized to fabricate the silicon-based mold by the etching technology using hydrofluoric acid. Ultimately, the PDMS based biochip was acquired through the PDMS thermal curing and demolding. In the second step, the Au nanoparticles coated SERS biochip was fabricated via the UV photoreduction method [173].

In the UV irradiation photoreduction method, the involved chemical reactions of Au nanoparticles formation are illustrated as follows:

$$\mathrm{HAuCl_4} \rightarrow \mathrm{H^+ + (Au^{III}Cl_4)^-}$$

$$\mathrm{(Au^{III}Cl_4)^-} \rightarrow \mathrm{Cl^0 + (Au^{II}Cl_3)^-}\ \text{(under UV irradiation)}$$

$$2(Au^{II}Cl_3)^- \rightarrow (Au^{III}Cl_4)^- + (Au^{I}Cl_2)^-$$

$$(Au^{I}Cl_2)^- \rightarrow Au^0 + Cl^0 + Cl^- \text{ (under UV irradiation)}$$

Specifically, the $HAuCl_4$ will dissociate to H^+ and $(Au^{III}Cl_4)^-$ ions spontaneously in an aqueous solution. Next, under the UV irradiation, the $(Au^{III}Cl_4)^-$ ions will reduce to $(Au^{II}Cl_3)^-$ ions via the photolysis. After that, the $(Au^{II}Cl_3)^-$ ions will further reduce to $(Au^{I}Cl_2)^-$ ions. Finally, the $(Au^{I}Cl_2)^-$ ions will photo-reduce to Au metal under the UV irradiation. Among them, the high surface energy improves these formed Au nanoparticles to assemble to larger structure, in which these nanoparticles cover the surface of the prepared PDMS based biochip and result in the Au coating film formation.

5.3 Characterization and discussion

5.3.1 Schematic illustration for hydrophobic PDMS based biochip

Ideally, the droplet can stay onto a flat surface of solid with a characteristic contact angle. From the classical Young equation, it describes the relationship between the contact angel and related interface [174]. As shown in Figure 60, the droplet is onto the surface of the solid object with a contact angle, the specific equation can be indicated as follows:

$$\cos\theta = (\gamma_{SV} - \gamma_{SL}) / \gamma_{LV}$$

where, the θ is contact angle, γ_{SV} presents the surface tension between solid and vapor, the γ_{SL} and γ_{LV} illustrate the relevant surface tension between solid and liquid, liquid and vapor, respectively. Besides, this equation can be regarded as a simple forces balance of surface tension.

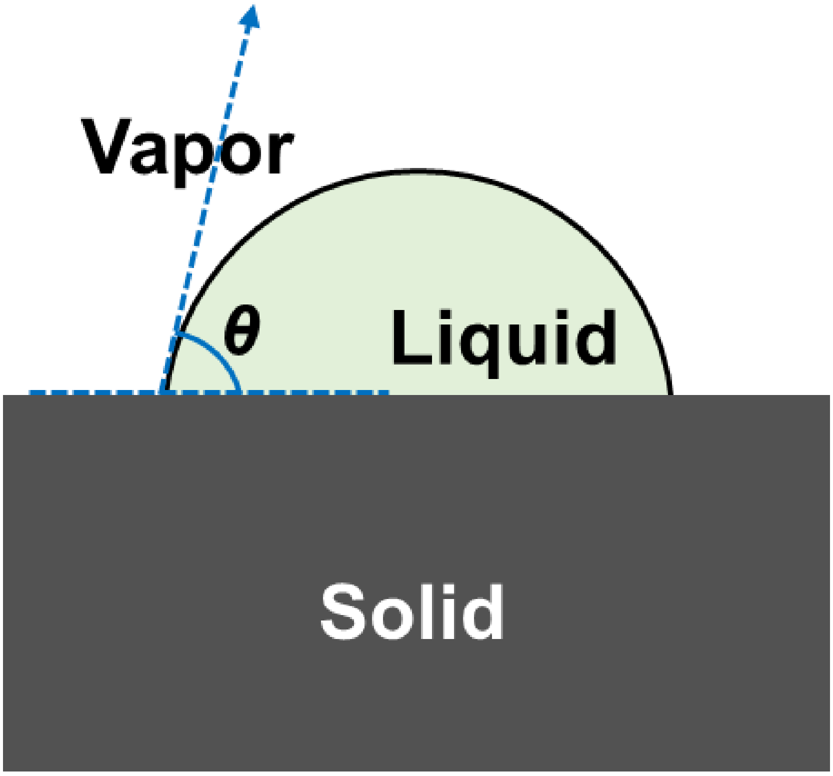

Figure 60. The schematic diagram of liquid connecting with flat solid surface.

On the other hand, as shown in Figure 61, if the surface of solid is rough, the contact between the liquid and solid is in the Wenzel or Cassie-Baxter state [175, 176]. For the first mechanism of Wenzel model, it relies on the contact area increase between the liquid and solid surface owing to the roughness and is affected by the geometric pattern. The relationship between the modified and unmodified contact angle is indicated as follow:

$$\mathrm{Cos}\ \theta_{\mathrm{w}} = r * \mathrm{Cos}\ \theta$$

θ_w is the modified angle in Wenzel state, θ presents the original contact angle. The parameter r is solid roughness, which is defined as the real and projected surface ratio. As a result, the wetting interaction is amplified by the surface roughness. Among them, when θ_w is less than $\pi/2$, the ratio r increases the surface hydrophilicity, and when the ratio θ_w is more than $\pi/2$, the roughness of surface improves the relevant hydrophobicity. In terms of the Cassie-Baxter model, the air might be trapped below the droplet and improve the related hydrophobicity of surface. The corresponding contact angle can be illustrated as:

$$\mathrm{Cos}\ \theta_{\mathrm{C}} = \Phi\ (\mathrm{Cos}\ \theta + 1) - 1$$

where, the Φ presents the contact fraction between the solid and droplet. The less the value of Φ, the larger the contact angle. This model is relatively intuitive and can be utilized for predicting the related contact angle with a droplet onto a patterned surface, which is proportional to the ratio of air contact with a droplet.

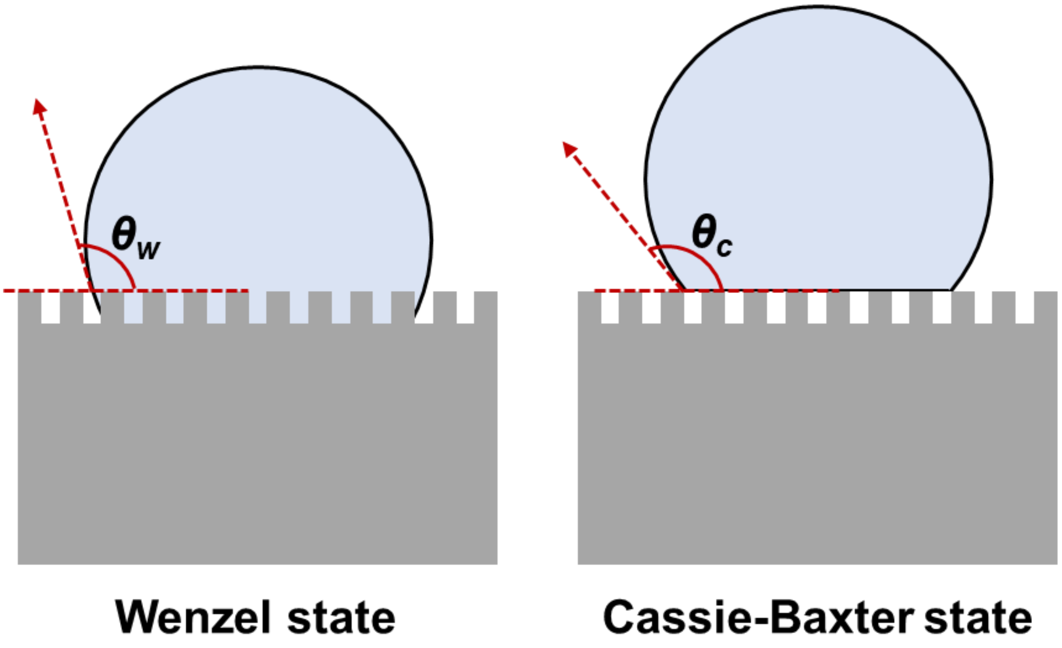

Figure 61. The schematic illustration of Wenzel state and Cassie-Baxter state for liquid contact with rough surface solid.

To achieve the solvent evaporation and the detected protein target concentrating, as shown in Figure 62a, the mechanisms for slow evaporating collapse can be described as two processes. The first one is that the droplet will touch the surface below the designed pillars. And the second mechanism is that the gained surface free energy wins over the lost surface free energy through the contact increase with the hydrophobic pillars. In lots of practical situations, the criterion of energetic argument is widely considered, in which the height of pillars is relatively independent during the hydrophobic evaporation process. Moreover, as illustrated in Figure 62b, the optimized relationship between gap and diameter of pillars is indicated in the shadowed area from the previous research [177]. And a parameter of 20 microns diameter and 45 microns gap is selected for the subsequent hydrophobic biochip manufacturing for α-syn biomarker detection.

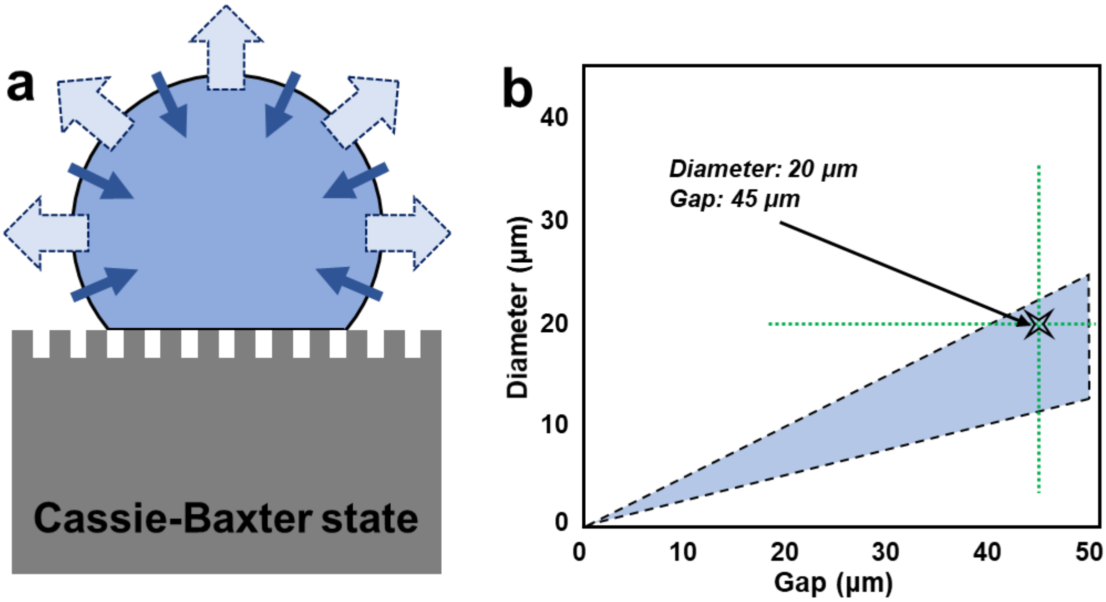

Figure 62. (a) The schematic diagram of evaporation process during the Cassie-Baxter state. (b) The relationship plot between diameter and gap of pillars.

5.3.2 Structure and layout drawing for designed pillars

For purposes of manufacturing the biochip, the AutoCAD software was utilized for designing the pillars pattern. As shown in Figure 63, the size of targeted PDMS based biochip is 1 cm* 1cm with length and width. The layout of hydrophobic pillars for detected proteins concentrating is expanded and illustrated in the right insets of Figure 63. It can be observed that the pillar diameter is 20 microns, and the pillar gap is 45 microns. This design pattern was firstly used as the related PDMS mold fabrication under the etching method, and then demolding for the final PDMS based biochip manufacturing.

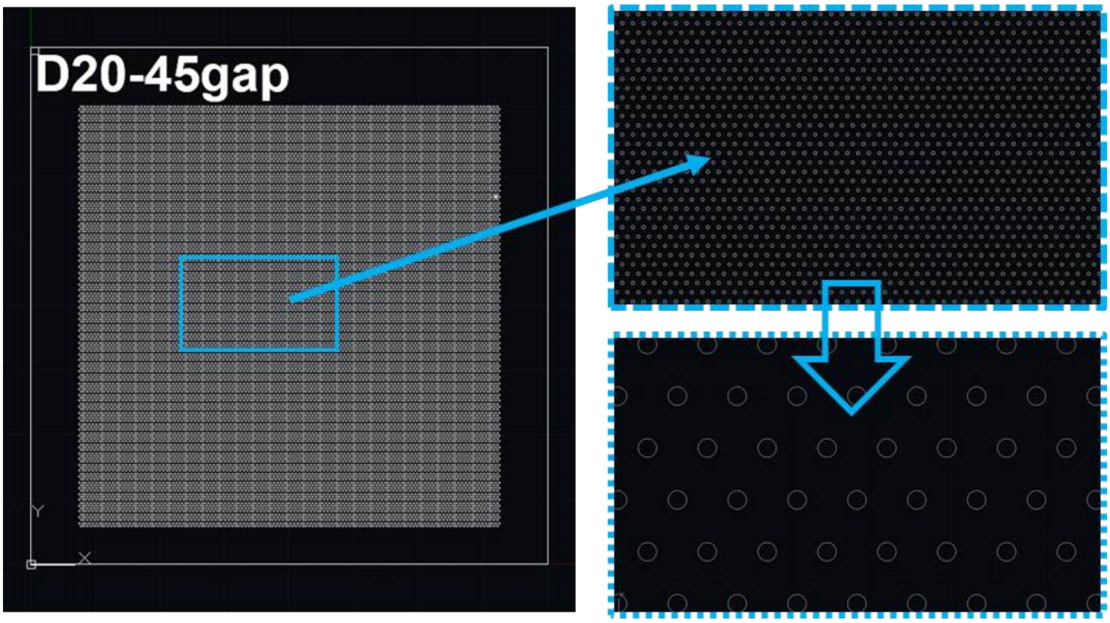

Figure 63. The AutoCAD design drawing of employed biochip and related partial enlarged detail showing at right insets.

5.3.3 Morphology research for utilized biochip

After the fabrication of utilized PDMS based hydrophobic biochip, the related morphology is investigated via the SEM technology as shown in Figure 64. In details, the top view of SEM image is exhibited in Figure 64a. It can be observed that the diameter of the designed and fabricated pillars is uniform with a size of 20 μm. The pillar gap is around 45 μm, which is as same as the designed AutoCAD pattern implying the successful manufacturing for targeted PDMS based biochip. On the other hand, the profile view of fabricated pillars is illustrated in Figure 64b, it can be seen that the height of manufactured pillars is homogeneous with a cylindrical shape, which indicates the successful demolding step for the final PDMS based biochip acquiring. Besides, from the top and side of the pillars, it can be observed the relevant coated dots, which can be attributed to the formation of the targeted Au nanoparticles for the Raman signals improvement as a SERS substrate. The corresponding investigated morphology of manufactured biochip demonstrates that the objective biochip is successfully manufactured and is expected for the further application of α-syn protein biomarker detection.

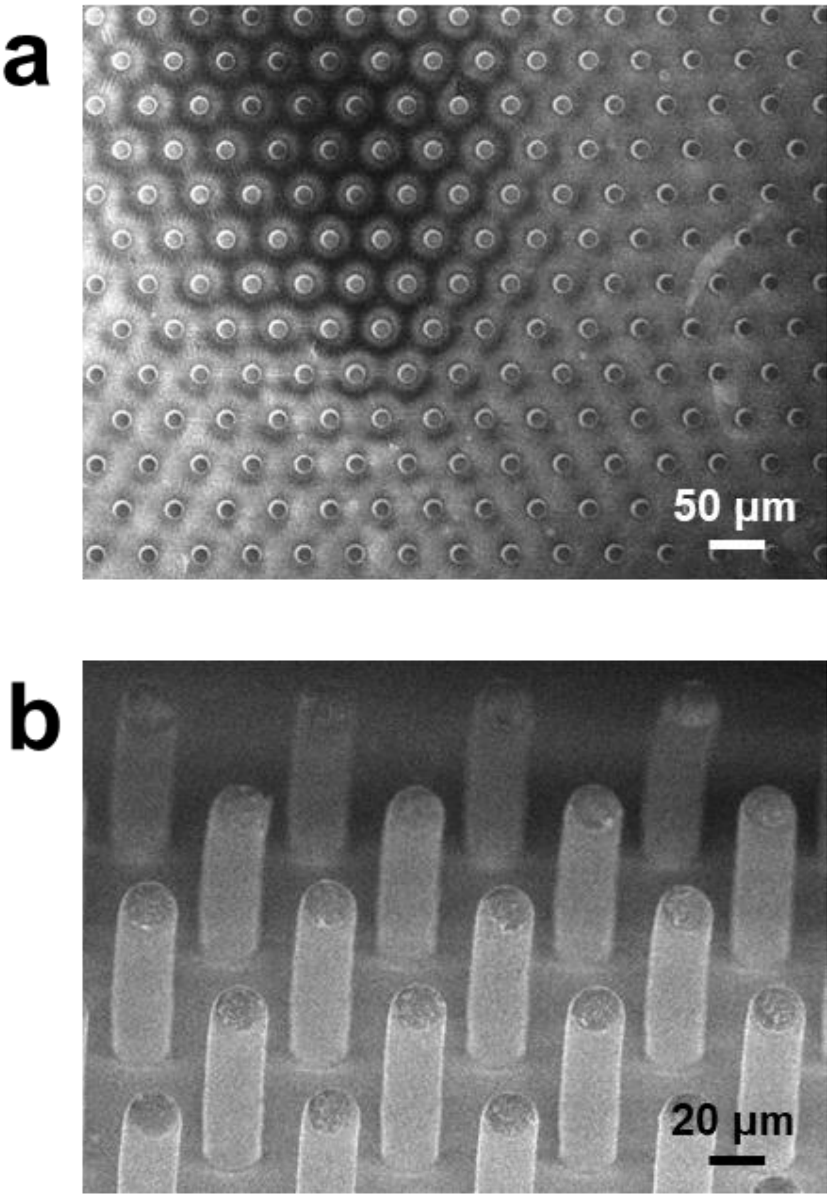

Figure 64. (a) The SEM image of utilized biochip in top view. (b) The SEM image of relevant pillars for biochip at the inclined view.

5.3.4 Investigations for hydrophobic performance

In addition, the relevant hydrophobic performance is also investigated as shown in Figure 65. Specifically, as can be seen for the Figure 65a, several droplets are dropped on the surface of the fabricated PDMS based biochip. Normally, the original PDMS biochip is clean and transparent, the red color for this manufactured hydrophobic biochip is originated from the Au nanoparticles coating onto the surface of the PDMS based biochip. Besides, the side view of the droplets onto the surface of fabricated biochip is exhibited in Figure 65b. Obviously, it can be seen that the contact angle between the droplets and the solid biochip possesses a very large value, which implies that the manufactured biochip can be utilized for the targeted proteins concentrating for improving the detection sensitivity.

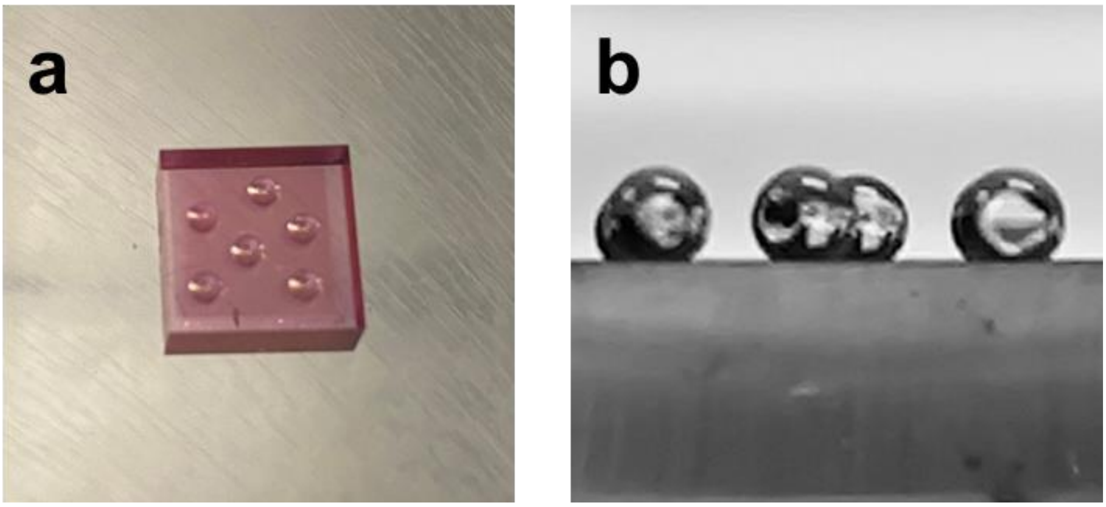

Figure 65. (a) The optical photo of hydrophobic biochip with several droplets. (b) The profile view optical image of biochip with some droplets.

5.3.5 Detection capacity for different forms of α-Syn protein

Furthermore, the related investigation of Raman spectra are illustrated in the Figure 66 and 67 for different forms of α-Syn protein. As can be seen from the Figure 66, it exhibited the unfolded α-Syn protein with several emission peaks. These emission peaks are approximately located at 1150, 1191, 1225, 1332, 1415, 1457, 1598, 1655, and 1690 cm^{-1}, respectively. According to the previous research, these emission peak of 1150, 1191, and 1225 cm^{-1} are mainly corresponding with the related vibration mode of νCC, Tyr/Phe, and Try, respectively [178]. The emission peaks of 1332, 1415, and 1457 cm^{-1} are related with the CH_2 deformation, symmetric νCO_2^-, and CH_2/CH_3 deformation, respectively.

And the emission peaks of 1598, 1655, and 1690 cm^{-1} are relevant with the Phe and amide I vibration mode. Different from the Raman spectra of Figure 66, as exhibited in the Figure 67, it can be observed that an obvious narrowed peak is at 1660 to 1670 cm^{-1} of Raman shift. Combining with the former study, this peak of fibrotic α-Syn protein resulted from the C=O stretch of peptide backbone [179]. Therefore, these excellent test results indicate that the fabricated biochip can be employed for the structure identifying of α-Syn protein, implying a great potential application for the prospective biosensing field.

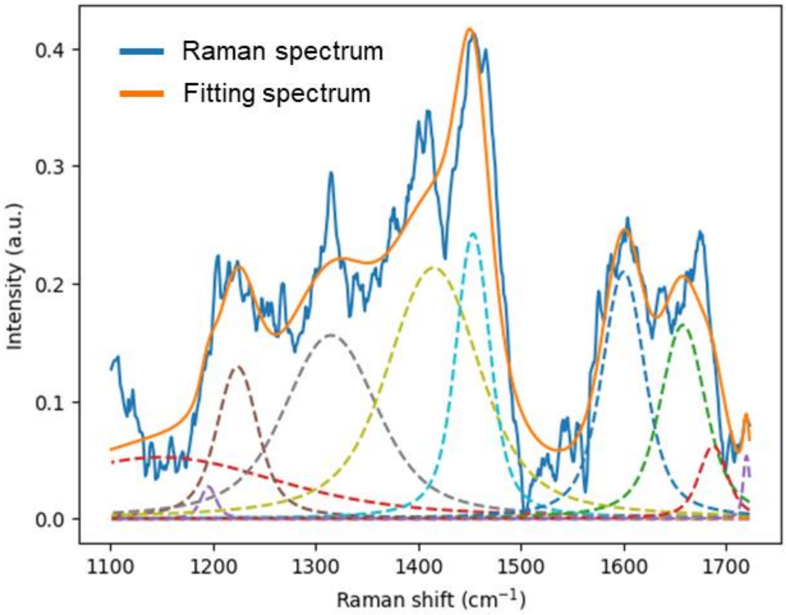

Figure 66. The Raman spectrum of normal α-Syn protein and related fitted curve.

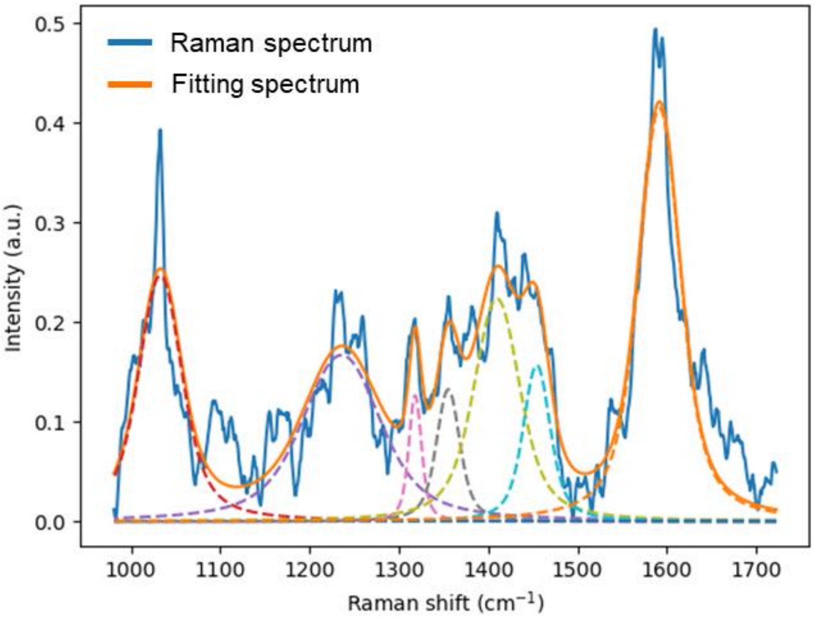

Figure 67. The Raman spectrum of fibrotic α-Syn protein and corresponding curve fitting.

5.4 Summary

In summary, considering of the relevant hydrophobic equations and related research work, the pattern of PDMS based biochip was designed via the AutoCAD software. Through the PDMS demolding and UV irradiation photoreduction methods, the SERS functionalized biochip was successfully fabricated from the corresponding morphology investigations of different view SEM images. Moreover, the captured optical photos further illustrate the great hydrophobic performance of manufacture biochip. Ultimately, the related Raman spectra indicate that the well-designed and fabricated point-of-care biochip can be utilized for the distinguishing the different forms of α-Syn protein, which implies a great potential for the NDDs detection application in the future.

Chapter 6 Conclusions and future work suggestions

The point-of-care biosensing platform based on UCNPs and microfluidic biochip was designed and fabricated for the biomarker of Nucleocapsid protein (N protein) *in-vitro* detection. The $NaYF_4:Er^{3+}/Yb^{3+}$ UCNPs with excellent luminescent stability and uniformity were successfully synthesized and used as the luminescent indicator. The designed microfluidic biochip was utilized as the detection chamber of the portable virus diagnostic platform, which illustrated outstanding filtration performance for the conjugated polystyrene microbeads. The fabricated biochip possessed excellent luminescence enhancement properties with a maximum of over 100-fold than the cuvette samples. Moreover, the cleanable performance of microfluidic biochip also implied great potential application for the virus diagnosis field. Compared with the typical commercial lateral flow assay (LFA) rapid test strips for virus detection, this point-of-care biosensing platform exhibited a higher biosensing sensitivity of around 1.12 pg/ml for N protein detection. In addition, the clinical samples also manifested that the designed point-of-care virus detection platform possessed better diagnostic sensitivity compared with the usual commercial LFA rapid test strips. These outstanding detection capabilities implied that the designed microfluidic biochip assisted portable virus diagnostic platform possessed enormous potential applications for the future unpredictable virus detection area.

Moreover, the developed point-of-care biosensing platform based on quantum dots (QDs) luminescence and microfluidic biochip with machine vision algorithm analysis was well-designed and manufactured for the carcinoembryonic antigen (CEA) tumor marker *in-vitro* diagnostics. The uniform core-shell QDs of CdSe/ZnS nanoparticles with extraordinary luminescent properties were employed for the optical labelling indicator of the designed sandwich structure immunoassay. The microfluidic biochip with excellent filtrated and cleanable performance was utilized as a functional chamber accessory of the designed CEA tumor marker biosensing platform, which illustrated a prominent diagnostic sensitivity of around 0.021 ng/ml. The Python-based machine vision algorithm was developed and applied as the corresponding images recognition and analysis for expected point-of-care CEA tumor marker detection. Moreover, for the investigation of saliva samples practical application evaluation, the designed intelligent biosensing platform exhibited outstanding detection cut-off value comparing with some common-used commercial CEA tumor marker LFA test strips. As a result, considering of these thrilling and remarkable system design superiority and diagnostic abilities, this well-designed intelligent biosensing platform implies tremendous application potentiality for the future point-of-care tumor marker detection field.

In addition, as the of neurodegenerative disease emerging, considering of the relevant hydrophobic theories and studies, the pattern of PDMS based biochip was designed via the AutoCAD software. Through the PDMS demolding and UV irradiation photoreduction methods, the SERS functionalized biochip was successfully fabricated from the corresponding morphology investigations of different view SEM images. Moreover, the captured optical photos further illustrate the great hydrophobic performance of manufacture biochip. Finally, the related Raman spectra indicate that the well-designed and fabricated point-of-care biochip can be utilized for the distinguishing the different forms of α-Syn protein, which implies a great potential for the neurodegenerative disease detection application in the future.

Although we design and investigate some novel point-of-care biosensing platforms based on the nanoparticles and biochips, the corresponding problems still have to be worked out for the real practical applications. For instance, it still possesses some difficulties for the stable and mass production of these utilized antibodies conjugated photoluminescent nanoparticles and PS microbeads. The conformance and consistency rate of biochip products also need to improve via the development of fabrication technology. Furthermore, in terms of the collaboration between the hardware and software of the biosensing platform need to promote through the assistance from professional researchers in computer science fields.

References

(1) Clarke, P.; Tyler, K. L. Apoptosis in animal models of virus-induced disease. *Nat Rev Microbiol* **2009**, *7* (2), 144-155.

(2) Carmeliet, P.; Jain, R. K. Angiogenesis in cancer and other diseases. *Nature* **2000**, *407* (6801), 249-257.

(3) Hansson, O. Biomarkers for neurodegenerative diseases. *Nat Med* **2021**, *27* (6), 954-963.

(4) Koonin, E. V.; Senkevich, T. G.; Dolja, V. V. The ancient Virus World and evolution of cells. *Biol Direct* **2006**, *1*, 29.

(5) Sankaran, N. On the historical significance of Beijerinck and his contagium vivum fluidum for modern virology. *Hist Philos Life Sci* **2018**, *40* (3), 41.

(6) Zhu, W.; Banadyga, L.; Emeterio, K.; Wong, G.; Qiu, X. The Roles of Ebola Virus Soluble Glycoprotein in Replication, Pathogenesis, and Countermeasure Development. *Viruses* **2019**, *11* (11).

(7) Ravina; Manjeet; Mohan, H.; Narang, J.; Pundir, S.; Pundir, C. S. A changing trend in diagnostic methods of Influenza A (H3N2) virus in human: a review. *3 Biotech* **2021**, *11* (2), 87.

(8) Pizzato, M.; Baraldi, C.; Boscato Sopetto, G.; Finozzi, D.; Gentile, C.; Gentile, M. D.; Marconi, R.; Paladino, D.; Raoss, A.; Riedmiller, I.; et al. SARS-CoV-2 and the Host Cell: A Tale of Interactions. *Frontiers in Virology* **2022**, *1*, 815388.

(9) Hu, B.; Guo, H.; Zhou, P.; Shi, Z. L. Characteristics of SARS-CoV-2 and COVID-

19. *Nat Rev Microbiol* **2021**, *19* (3), 141-154.

(10) Li, J.; Lai, S.; Gao, G. F.; Shi, W. The emergence, genomic diversity and global spread of SARS-CoV-2. *Nature* **2021**, *600* (7889), 408-418.

(11) Hadi, J.; Dunowska, M.; Wu, S.; Brightwell, G. Control Measures for SARS-CoV-2: A Review on Light-Based Inactivation of Single-Stranded RNA Viruses. *Pathogens* **2020**, *9* (9).

(12) Minna, J. D.; Roth, J. A.; Gazdar, A. F. Focus on lung cancer. *Cancer cell* **2002**, *1* (1), 49-52.

(13) Kamisawa, T.; Wood, L. D.; Itoi, T.; Takaori, K. Pancreatic cancer. *Lancet* **2016**, *388* (10039), 73-85.

(14) Li, J.; Chen, Y.; Wang, X.; Wang, C.; Xiao, M. The value of combined detection of CEA, CYFRA21-1, SCC-Ag, and pro-GRP in the differential diagnosis of lung cancer. *Transl Cancer Res* **2021**, *10* (4), 1900-1906.

(15) Poruk, K. E.; Gay, D. Z.; Brown, K.; Mulvihill, J. D.; Boucher, K. M.; Scaife, C. L.; Firpo, M. A.; Mulvihill, S. J. The Clinical Utility of CA 19-9 in Pancreatic Adenocarcinoma: Diagnostic and Prognostic Updates. *Current molecular medicine* **2013**, *13* (3), 340-351.

(16) Goedert, M. Alpha-synuclein and neurodegenerative diseases. *Nat Rev Neurosci* **2001**, *2* (7), 492-501.

(17) Cookson, M. R. The role of leucine-rich repeat kinase 2 (LRRK2) in Parkinson's disease. *Nat Rev Neurosci* **2010**, *11* (12), 791-797.

(18) Guo, T.; Noble, W.; Hanger, D. P. Roles of tau protein in health and disease. *Acta Neuropathol* **2017**, *133* (5), 665-704.

(19) Janelidze, S.; Zetterberg, H.; Mattsson, N.; Palmqvist, S.; Vanderstichele, H.; Lindberg, O.; van Westen, D.; Stomrud, E.; Minthon, L.; Blennow, K.; et al. CSF Abeta42/Abeta40 and Abeta42/Abeta38 ratios: better diagnostic markers of Alzheimer disease. *Ann Clin Transl Neurol* **2016**, *3* (3), 154-165.

(20) Mielke, M. M.; Dage, J. L.; Frank, R. D.; Algeciras-Schimnich, A.; Knopman, D. S.; Lowe, V. J.; Bu, G.; Vemuri, P.; Graff-Radford, J.; Jack, C. R., Jr.; et al. Performance of plasma phosphorylated tau 181 and 217 in the community. *Nat Med* **2022**, *28* (7), 1398-1405.

(21) Lewczuk, P.; Ermann, N.; Andreasson, U.; Schultheis, C.; Podhorna, J.; Spitzer, P.; Maler, J. M.; Kornhuber, J.; Blennow, K.; Zetterberg, H. Plasma neurofilament light as a potential biomarker of neurodegeneration in Alzheimer's disease. *Alzheimers Res Ther* **2018**, *10* (1), 71.

(22) Draz, M. S.; Shafiee, H. Applications of gold nanoparticles in virus detection. *Theranostics* **2018**, *8* (7), 1985-2017. DOI: 10.7150/thno.23856 From NLM Medline.

(23) Pabla, S. S.; Pabla, S. S. Real-time polymerase chain reaction: A revolution in diagnostics. *Resonance* **2008**, *13*, 369-377.

(24) Macedo, F.; Antônio, H.; Roberto, M.; Marcel, R. D.; Helio, R. H.; Ricardo, V. Computer-aided detection system for lung cancer in computed tomography scans: review and future prospects. *Biomedical engineering online* **2014**, *13*, 1-16.

(25) Thompson, J.; Lawrentschuk, N.; Frydenberg, M.; Thompson, L.; Stricker, P.; Usanz. The role of magnetic resonance imaging in the diagnosis and management of prostate cancer. *BJU Int* **2013**, *112 Suppl 2*, 6-20.

(26) Zubor, P.; Kubatka, P.; Kajo, K.; Dankova, Z.; Polacek, H.; Bielik, T.; Kudela, E.; Samec, M.; Liskova, A.; Vlcakova, D.; et al. Why the Gold Standard Approach by Mammography Demands Extension by Multiomics? Application of Liquid Biopsy miRNA Profiles to Breast Cancer Disease Management. *Int J Mol Sci* **2019**, *20* (12).

(27) Wu, J.; Wang, T.; Uckermann, O.; Galli, R.; Schackert, G.; Cao, L.; Czarske, J.; Kuschmierz, R. Learned end-to-end high-resolution lensless fiber imaging towards real-time cancer diagnosis. *Scientific Reports* **2022**, *12* (1), 18846.

(28) Agosta, F.; Galantucci, S.; Filippi, M. Advanced magnetic resonance imaging of neurodegenerative diseases. *Neurol Sci* **2017**, *38* (1), 41-51.

(29) Barc, K.; Kuzma-Kozakiewicz, M. Positron emission tomography neuroimaging in neurodegenerative diseases: Alzheimer's disease, Parkinson's disease, and amyotrophic lateral sclerosis. *Neurol Neurochir Pol* **2019**, *53* (2), 99-112.

(30) Seino, Y.; Nakamura, T.; Kawarabayashi, T.; Hirohata, M.; Narita, S.; Wakasaya, Y.; Kaito, K.; Ueda, T.; Harigaya, Y.; Shoji, M. Cerebrospinal Fluid and Plasma Biomarkers in Neurodegenerative Diseases. *J Alzheimers Dis* **2019**, *68* (1), 395-404.

(31) Costa, A.; Bak, T.; Caffarra, P.; Caltagirone, C.; Ceccaldi, M.; Collette, F.; Crutch, S.; Della Sala, S.; Demonet, J. F.; Dubois, B.; et al. The need for harmonisation and innovation of neuropsychological assessment in neurodegenerative dementias in

Europe: consensus document of the Joint Program for Neurodegenerative Diseases Working Group. *Alzheimers Res Ther* **2017**, *9* (1), 27.

(32) Luan, H.; Wang, X.; Cai, Z. Mass spectrometry-based metabolomics: Targeting the crosstalk between gut microbiota and brain in neurodegenerative disorders. *Mass Spectrom Rev* **2019**, *38* (1), 22-33. DOI: 10.1002/mas.21553 From NLM Medline.

(33) Choi, J. R.; Hu, J.; Tang, R.; Gong, Y.; Feng, S.; Ren, H. An integrated paper-based sample-to-answer biosensor for nucleic acid testing at the point of care. *Lab on a Chip* **2016**, *16* (3), 611-621.

(34) Zhang, L.; Yang, W.; Yang, Y.; Liu, H.; Gu, Z. Smartphone-based point-of-care testing of salivary alpha-amylase for personal psychological measurement. *Analyst* **2015**, *140* (21), 7399-7406.

(35) Thiha, A.; Ibrahim, F. A Colorimetric Enzyme-Linked Immunosorbent Assay (ELISA) Detection Platform for a Point-of-Care Dengue Detection System on a Lab-on-Compact-Disc. *Sensors (Basel)* **2015**, *15* (5), 11431-11441.

(36) Kehoe, E.; Penn, R. L. Introducing Colorimetric Analysis with Camera Phones and Digital Cameras: An Activity for High School or General Chemistry. *Journal of Chemical Education* **2013**, *90* (9), 1191-1195.

(37) Zarei, M. Portable biosensing devices for point-of-care diagnostics: Recent developments and applications. *TrAC Trends in Analytical Chemistry* **2017**, *91*, 26-41.

(38) Kim, J.-H.; Joo, H.-G.; Kim, T.-H.; Ju, Y.-G. A smartphone-based fluorescence microscope utilizing an external phone camera lens module. *BioChip Journal* **2015**, *9*

(4), 285-292.

(39) Petryayeva, E.; Algar, W. R. <45-error.pdf>. *Analyst* **2015**, *140* (12), 4037-4045.

(40) Liu, Y.; Liu, Q.; Chen, S.; Cheng, F.; Wang, H.; Peng, W. Surface Plasmon Resonance Biosensor Based on Smart Phone Platforms. *Sci Rep* **2015**, *5*, 12864.

(41) Bai, G.; Tsang, M. K.; Hao, J. Luminescent Ions in Advanced Composite Materials for Multifunctional Applications. *Advanced Functional Materials* **2016**, *26* (35), 6330-6350.

(42) Jiang, C.; Xu, W. Theoretical Model of Yb3+-Er3+-Tm3+-Codoped System for White Light Generation. *Journal of Display Technology* **2009**, *5* (8), 312-318.

(43) Heer, S.; Kömpe, K.; Güdel, H. U.; Haase, M. Highly Efficient Multicolour Upconversion Emission in Transparent Colloids of Lanthanide - Doped NaYF4 Nanocrystals. *Advanced Materials* **2004**, *16* (23-24), 2102-2105.

(44) Yi, G.; Lu, H.; Zhao, S.; Ge, Y.; Yang, W.; Chen, D.; Guo, L. H. Synthesis, characterization, and biological application of size-controlled nanocrystalline NaYF4: Yb, Er infrared-to-visible up-conversion phosphors. *Nano letters* **2004**, *4* (11), 2191-2196.

(45) Wang, F.; Fan, X.; Pi, D.; Wang, Z.; Wang, M. Hydrothermal synthesis and luminescence behavior of rare-earth-doped NaLa(WO4)2 powders. *Journal of Solid State Chemistry* **2005**, *178* (3), 825-830.

(46) Luo, W.; Li, R.; Chen, X. Host-Sensitized Luminescence of Nd3+ and Sm3+ Ions Incorporated in Anatase Titania Nanocrystals. *The Journal of Physical Chemistry C*

2009, *113* (20), 8772-8777.

(47) Wong, H. T.; Chan, H. L. W.; Hao, J. H. Magnetic and luminescent properties of multifunctional GdF3:Eu3+ nanoparticles. *Applied physics letters* **2009**, *95* (2).

(48) Wang, F.; Liu, X. Upconversion Multicolor Fine-Tuning: Visible to Near-Infrared Emission from Lanthanide-Doped NaYF4 Nanoparticles. *Journal of the American Chemical Society* **2008**, *130* (17), 5642-5643.

(49) Yang, J.; Zhang, C.; Peng, C.; Li, C.; Wang, L.; Chai, R.; Lin, J. Controllable red, green, blue (RGB) and bright white upconversion luminescence of Lu2O3:Yb3+/Er3+/Tm3+ nanocrystals through single laser excitation at 980 nm. *Chemistry* **2009**, *15* (18), 4649-4655.

(50) Wang, F.; Banerjee, D.; Liu, Y.; Chen, X.; Liu, X. Upconversion nanoparticles in biological labeling, imaging, and therapy. *Analyst* **2010**, *135* (8), 1839-1854.

(51) Michalet, X.; Pinaud, F. F.; Bentolila, L. A.; Tsay, J. M.; Doose, S.; Li, J. J. Quantum Dots for Live Cells, in Vivo Imaging, and Diagnostics. *Science* **2005**, *307* (5709), 538-544.

(52) Peng, H.; Zhang, L.; Kjällman, T. H.; Soeller, C.; Travas-Sejdic, J. DNA Hybridization Detection with Blue Luminescent Quantum Dots and Dye-Labeled Single-Stranded DNA. *Journal of the American Chemical Society* **2007**, *129* (11), 3048-3049.

(53) Ge, C.; Xu, M.; Liu, J.; Lei, J.; Ju, H. Facile synthesis and application of highly luminescent CdTe quantum dots with an electrogenerated precursor. *Chem Commun*

(Camb) **2008**, (4), 450-452.

(54) Han, M.; Gao, X.; Su, J. Z.; Nie, S. Quantum-dot-tagged microbeads for multiplexed optical coding of biomolecules. *Nat Biotechnol* **2001**, *19* (7), 631-635.

(55) Resch-Genger, U.; Grabolle, M.; Cavaliere-Jaricot, S.; Nitschke, R.; Nann, T. Quantum dots versus organic dyes as fluorescent labels. *Nat Methods* **2008**, *5* (9), 763-775.

(56) Wen, L.; Qiu, L.; Wu, Y.; Hu, X.; Zhang, X. Aptamer-Modified Semiconductor Quantum Dots for Biosensing Applications. *Sensors* **2017**, *17* (8), 1736.

(57) Fruncillo, S.; Su, X.; Liu, H.; Wong, L. S. Lithographic Processes for the Scalable Fabrication of Micro- and Nanostructures for Biochips and Biosensors. *ACS Sens* **2021**, *6* (6), 2002-2024.

(58) Ferreira, D. A.; Rothbauer, M.; Conde, J. P.; Ertl, P.; Oliveira, C.; Granja, P. L. A Fast Alternative to Soft Lithography for the Fabrication of Organ-on-a-Chip Elastomeric-Based Devices and Microactuators. *Adv Sci (Weinh)* **2021**, *8* (8), 2003273.

(59) Monia Kabandana, G. K.; Zhang, T.; Chen, C. Emerging 3D printing technologies and methodologies for microfluidic development. *Anal Methods* **2022**, *14* (30), 2885-2906.

(60) Cui, P.; Wang, S. Application of microfluidic chip technology in pharmaceutical analysis: A review. *J Pharm Anal* **2019**, *9* (4), 238-247.

(61) Yafia, M.; Ymbern, O.; Olanrewaju, A. O.; Parandakh, A.; Sohrabi Kashani, A.; Renault, J.; Jin, Z.; Kim, G.; Ng, A.; Juncker, D. Microfluidic chain reaction of

structurally programmed capillary flow events. *Nature* **2022**, *605* (7910), 464-469.

(62) Butt, M. A.; Kazanskiy, N. L.; Khonina, S. N. Advances in Waveguide Bragg Grating Structures, Platforms, and Applications: An Up-to-Date Appraisal. *Biosensors (Basel)* **2022**, *12* (7).

(63) Esposito, J. J.; Sammons, S. A.; Frace, A. M.; Osborne, J. D.; Olsen-Rasmussen, M.; Zhang, M. Genome Sequence Diversity and Clues to the Evolution of Variola (Smallpox) Virus. *Science* **2006**, *313* (5788), 807-812.

(64) Patrono, L. V.; Vrancken, B.; Budt, M.; Dux, A.; Lequime, S.; Boral, S.; Gilbert, M. T. P.; Gogarten, J. F.; Hoffmann, L.; Horst, D.; et al. Archival influenza virus genomes from Europe reveal genomic variability during the 1918 pandemic. *Nat Commun* **2022**, *13* (1), 2314.

(65) Jacob, S. T.; Crozier, I.; Fischer, W. A., 2nd; Hewlett, A.; Kraft, C. S.; Vega, M. A.; Soka, M. J.; Wahl, V.; Griffiths, A.; Bollinger, L.; et al. Ebola virus disease. *Nat Rev Dis Primers* **2020**, *6* (1), 13.

(66) Katzelnick, L. C.; Narvaez, C.; Arguello, S.; Lopez Mercado, B.; Collado, D.; Ampie, O. Zika virus infection enhances future risk of severe dengue disease. *Science* **2020**, *369* (6507), 1123-1128.

(67) Wolff Sagy, Y.; Zucker, R.; Hammerman, A.; Markovits, H.; Arieh, N. G.; Abu Ahmad, W.; Battat, E.; Ramot, N.; Carmeli, G.; Mark-Amir, A.; et al. Real-world effectiveness of a single dose of mpox vaccine in males. *Nat Med* **2023**, *29* (3), 748-752.

(68) Ma, Y.; Song, M.; Li, L.; Lao, X.; Wong, M. C.; Hao, J. Advances in upconversion luminescence nanomaterial-based biosensor for virus diagnosis. *Exploration (Beijing)* **2022**, *2* (6), 20210216.

(69) Sounderajah, V.; Ashrafian, H.; Aggarwal, R.; De Fauw, J.; Denniston, A. K.; Greaves, F.; Karthikesalingam, A.; King, D.; Liu, X.; Markar, S. R.; et al. Developing specific reporting guidelines for diagnostic accuracy studies assessing AI interventions: The STARD-AI Steering Group. *Nat Med* **2020**, *26* (6), 807-808.

(70) Yin, Z.; Ramshani, Z.; Waggoner, J. J.; Pinsky, B. A.; Senapati, S.; Chang, H.-C. A non-optical multiplexed PCR diagnostic platform for serotype-specific detection of dengue virus. *Sensors and Actuators B: Chemical* **2020**, *310.*

(71) Choi, D. H.; Lee, S. K.; Oh, Y. K.; Bae, B. W.; Lee, S. D.; Kim, S.; Shin, Y. B.; Kim, M. G. A dual gold nanoparticle conjugate-based lateral flow assay (LFA) method for the analysis of troponin I. *Biosens Bioelectron* **2010**, *25* (8), 1999-2002.

(72) Masoumeh Ghorbanpour, S.; Wen, S.; Kaitu'u-Lino, T. J.; Hannan, N. J.; Jin, D.; McClements, L. Quantitative Point of Care Tests for Timely Diagnosis of Early-Onset Preeclampsia with High Sensitivity and Specificity. *Angew Chem Int Ed Engl* **2023**, *62* (26), e202301193.

(73) Teengam, P.; Nisab, N.; Chuaypen, N.; Tangkijvanich, P.; Vilaivan, T.; Chailapakul, O. Fluorescent paper-based DNA sensor using pyrrolidinyl peptide nucleic acids for hepatitis C virus detection. *Biosens Bioelectron* **2021**, *189*, 113381.

(74) Tsang, M. K.; Ye, W.; Wang, G.; Li, J.; Yang, M.; Hao, J. Ultrasensitive Detection

of Ebola Virus Oligonucleotide Based on Upconversion Nanoprobe/Nanoporous Membrane System. *ACS Nano* **2016**, *10* (1), 598-605.

(75) Tsang, M. K.; Wong, Y. T.; Tsoi, T. H.; Wong, W. T.; Hao, J. Upconversion Luminescence Sandwich Assay For Detection of Influenza H7 Subtype. *Adv Healthc Mater* **2019**, *8* (18), e1900575.

(76) Song, M.; Wong, M. C.; Li, L.; Guo, F.; Liu, Y.; Ma, Y.; Lao, X.; Wang, P.; Chen, H.; Yang, M.; et al. Rapid point-of-care detection of SARS-CoV-2 RNA with smartphone-based upconversion luminescence diagnostics. *Biosens Bioelectron* **2023**, *222*, 114987.

(77) Lin, H.; Yu, W.; K, A. S.; Bogumil, M.; Zhao, Y.; Hambalek, J.; Lin, S.; Chandrasekaran, S.; Garner, O.; Di Carlo, D.; et al. Ferrobotic swarms enable accessible and adaptable automated viral testing. *Nature* **2022**, *611* (7936), 570-577.

(78) Zhang, Z.; Ma, P.; Ahmed, R.; Wang, J.; Akin, D.; Soto, F.; Liu, B. F.; Li, P.; Demirci, U. Advanced Point-of-Care Testing Technologies for Human Acute Respiratory Virus Detection. *Adv Mater* **2022**, *34* (1), e2103646.

(79) Lee, K.; Kim, S. E.; Doh, J.; Kim, K.; Chung, W. K. User-friendly image-activated microfluidic cell sorting technique using an optimized, fast deep learning algorithm. *Lab Chip* **2021**, *21* (9), 1798-1810.

(80) Scandurra, C.; Björkström, K.; Sarcina, L.; Imbriano, A.; Di Franco, C.; Österbacka, R.; Bollella, P.; Scamarcio, G.; Torsi, L.; Macchia, E. Single Molecule with a Large Transistor – SiMoT cytokine IL‐6 Detection Benchmarked against a

Chemiluminescent Ultrasensitive Immunoassay Array. *Advanced Materials Technologies* **2023**, *8* (11).

(81) He, L.; Tessier, D. R.; Briggs, K.; Tsangaris, M.; Charron, M.; McConnell, E. M.; Lomovtsev, D.; Tabard-Cossa, V. Digital immunoassay for biomarker concentration quantification using solid-state nanopores. *Nat Commun* **2021**, *12* (1), 5348.

(82) Heggestad, J. T.; Fontes, C. M.; Joh, D. Y.; Hucknall, A. M.; Chilkoti, A. In Pursuit of Zero 2.0: Recent Developments in Nonfouling Polymer Brushes for Immunoassays. *Adv Mater* **2020**, *32* (2), e1903285.

(83) Poudineh, M.; Maikawa, C. L.; Ma, E. Y.; Pan, J.; Mamerow, D.; Hang, Y.; Baker, S. W.; Beirami, A.; Yoshikawa, A.; Eisenstein, M.; et al. A fluorescence sandwich immunoassay for the real-time continuous detection of glucose and insulin in live animals. *Nat Biomed Eng* **2021**, *5* (1), 53-63.

(84) Huang, K.; Green, K. K.; Huang, L.; Hallen, H.; Han, G.; Lim, S. F. Room-temperature upconverted superfluorescence. *Nature Photonics* **2022**, *16* (10), 737-742.

(85) Peng, C.; Chen, X.; Suh, Y. D.; Liu, X. Binary Ligand-Mediated Photochromic Tuning of Lanthanide - Doped Upconversion Nanoparticle Conjugates. *Advanced Optical Materials* **2022**, *10* (22).

(86) Ren, W.; Lin, G.; Clarke, C.; Zhou, J.; Jin, D. Optical Nanomaterials and Enabling Technologies for High-Security-Level Anticounterfeiting. *Adv Mater* **2020**, *32* (18), e1901430.

(87) Sun, M.; Qu, A.; Hao, C.; Wu, X.; Xu, L.; Xu, C.; Kuang, H. Chiral Upconversion

Heterodimers for Quantitative Analysis and Bioimaging of Antibiotic-Resistant Bacteria In Vivo. *Adv Mater* **2018**, *30* (50), e1804241.

(88) Qu, A.; Wu, X.; Li, S.; Sun, M.; Xu, L.; Kuang, H.; Xu, C. An NIR-Responsive DNA-Mediated Nanotetrahedron Enhances the Clearance of Senescent Cells. *Adv Mater* **2020**, *32* (14), e2000184.

(89) Liu, Y.; Hu, P.; Zheng, Z.; Zhong, D.; Xie, W.; Tang, Z.; Pan, B.; Luo, J.; Zhang, W.; Wang, X. Photoresponsive Vaccine-Like CAR-M System with High-Efficiency Central Immune Regulation for Inflammation-Related Depression. *Adv Mater* **2022**, *34* (11), e2108525.

(90) Quesada-Gonzalez, D.; Merkoci, A. Nanomaterial-based devices for point-of-care diagnostic applications. *Chem Soc Rev* **2018**, *47* (13), 4697-4709.

(91) Huang, C. H.; Park, Y. I.; Lin, H. Y.; Pathania, D.; Park, K. S.; Avila-Wallace, M.; Castro, C. M.; Weissleder, R.; Lee, H. Compact and Filter-Free Luminescence Biosensor for Mobile in Vitro Diagnoses. *ACS Nano* **2019**, *13* (10), 11698-11706.

(92) Song, Y.; Lu, M.; Xie, Y.; Sun, G.; Chen, J.; Zhang, H.; Liu, X.; Zhang, F.; Sun, L. Deep Learning Fluorescence Imaging of Visible to NIR‐II Based on Modulated Multimode Emissions Lanthanide Nanocrystals. *Advanced Functional Materials* **2022**, *32* (45).

(93) Liu, Y.; Bai, G.; Pan, E.; Hua, Y.; Chen, L.; Xu, S. Upconversion fluorescence property of Er3+/Yb3+ codoped lanthanum titanate microcrystals for optical thermometry. *Journal of Alloys and Compounds* **2020**, *822*.

(94) Liu, Y.; Bai, G.; Lyu, Y.; Hua, Y.; Ye, R.; Zhang, J.; Chen, L.; Xu, S.; Hao, J. Ultrabroadband Tuning and Fine Structure of Emission Spectra in Lanthanide Er-Doped ZnSe Nanosheets for Display and Temperature Sensing. *ACS Nano* **2020**, *14* (11), 16003-16012.

(95) Peeples, C. A.; Kober, D.; Schmitt, F. J.; Tholen, P.; Siemensmeyer, K.; Halldorson, Q.; Çoşut, B.; Gurlo, A.; Yazaydin, A. O.; Hanna, G.; et al. A 3D Cu‐Naphthalene‐Phosphonate Metal–Organic Framework with Ultra‐High Electrical Conductivity. *Advanced Functional Materials* **2020**, *31* (3).

(96) Sando, D.; Carrétéro, C.; Grisolia, M. N.; Barthélémy, A.; Nagarajan, V.; Bibes, M. Revisiting the Optical Band Gap in Epitaxial BiFeO3 Thin Films. *Advanced Optical Materials* **2017**, *6* (2).

(97) Iannacone, M.; Guidotti, L. G. Immunobiology and pathogenesis of hepatitis B virus infection. *Nat Rev Immunol* **2022**, *22* (1), 19-32.

(98) Li, T.; Zhou, C.; Jiang, M. UV absorption spectra of polystyrene. *Polymer Bulletin* **1991**, *25*, 211-216.

(99) Dobrynin, D.; Polischuk, I.; Pokroy, B. A Comparison Study of the Detection Limit of Omicron SARS-CoV-2 Nucleocapsid by Various Rapid Antigen Tests. *Biosensors (Basel)* **2022**, *12* (12).

(100) Huntington, N. D.; Cursons, J.; Rautela, J. The cancer-natural killer cell immunity cycle. *Nat Rev Cancer* **2020**, *20* (8), 437-454.

(101) Vitale, I.; Shema, E.; Loi, S.; Galluzzi, L. Intratumoral heterogeneity in cancer

progression and response to immunotherapy. *Nat Med* **2021**, *27* (2), 212-224.

(102) Visvader, J. E. Cells of origin in cancer. *Nature* **2011**, *469* (7330), 314-322.

(103) Bray, F.; Laversanne, M.; Sung, H.; Ferlay, J.; Siegel, R. L.; Soerjomataram, I.; Jemal, A. Global cancer statistics 2022: GLOBOCAN estimates of incidence and mortality worldwide for 36 cancers in 185 countries. *CA Cancer J Clin* **2024**, *74* (3), 229-263.

(104) Gridelli, C.; Rossi, A.; Carbone, D. P.; Guarize, J.; Karachaliou, N.; Mok, T.; Petrella, F.; Spaggiari, L.; Rosell, R. Non-small-cell lung cancer. *Nat Rev Dis Primers* **2015**, *1*, 15009.

(105) Mizrahi, J. D.; Surana, R.; Valle, J. W.; Shroff, R. T. Pancreatic cancer. *Lancet* **2020**, *395* (10242), 2008-2020.

(106) Duffy, M. J.; Sturgeon, C.; Lamerz, R.; Haglund, C.; Holubec, V. L.; Klapdor, R.; Nicolini, A.; Topolcan, O.; Heinemann, V. Tumor markers in pancreatic cancer: a European Group on Tumor Markers (EGTM) status report. *Ann Oncol* **2010**, *21* (3), 441-447.

(107) Leveridge, M. J.; Bostrom, P. J.; Koulouris, G.; Finelli, A.; Lawrentschuk, N. Imaging renal cell carcinoma with ultrasonography, CT and MRI. *Nat Rev Urol* **2010**, *7* (6), 311-325.

(108) Bouzigues, C.; Gacoin, T.; Alexandrou, A. Biological Applications of Rare-Earth Based Nanoparticles. *ACS nano* **2011**, *5* (11), 8488-8505.

(109) Jain, A.; Fournier, P. G. J.; Mendoza-Lavaniegos, V.; Sengar, P.; Guerra-Olvera,

F. M.; Iniguez, E.; Kretzschmar, T. G.; Hirata, G. A.; Juarez, P. Functionalized rare earth-doped nanoparticles for breast cancer nanodiagnostic using fluorescence and CT imaging. *J Nanobiotechnology* **2018**, *16* (1), 26.

(110) Cheng, F.; Su, L.; Qian, C. Circulating tumor DNA: a promising biomarker in the liquid biopsy of cancer. *Oncotarget* **2016**, *7* (30), 48832.

(111) Lubin, R.; Zalcman, G.; Bouchet, L.; Trédaniel, J.; Legros, Y.; Cazals, D. Serum p53 antibodies as early markers of lung cancer. *Nature medicine* **1995**, *1* (7), 701-702.

(112) Yonet-Tanyeri, N.; Ahlmark, B. Z.; Little, S. R. Advances in Multiplexed Paper-Based Analytical Devices for Cancer Diagnosis: A Review of Technological Developments. *Adv Mater Technol* **2021**, *6* (8).

(113) Yaari, Z.; Yang, Y.; Apfelbaum, E.; Cupo, C.; Settle, A. H.; Cullen, Q.; Heller, D. A. A perception-based nanosensor platform to detect cancer biomarkers. *Science Advances* **2021**, *7* (47), eabj0852.

(114) Kumar, N.; Sorna, G.; Raju Khan, V.; Ranjan, P.; Abubakar Sadique, M.; Yadav, S.; Singhal, A.; Mishra, A.; Murali, S. Efficiency of Nanomaterials for Electrochemical Diagnostics based Point-of-Care Detection of Non-Invasive Oral Cancer Biomarkers. *Advanced Materials Letters* **2021**, *12* (8), 1-20.

(115) Li, W.; Wang, H.; Zhao, Z.; Gao, H.; Liu, C.; Zhu, L.; Wang, C.; Yang, Y. Emerging Nanotechnologies for Liquid Biopsy: The Detection of Circulating Tumor Cells and Extracellular Vesicles. *Adv Mater* **2019**, *31* (45), e1805344.

(116) Kaur, J.; Preethi, M.; Srivastava, R.; Borse, V. Role of IL-6 and IL-8 biomarkers

for optical and electrochemical based point-of-care detection of oral cancer. *Biosensors and Bioelectronics: X* **2022**, *11*.

(117) Garcia de Arquer, F. P.; Talapin, D. V.; Klimov, V. I.; Arakawa, Y.; Bayer, M.; Sargent, E. H. Semiconductor quantum dots: Technological progress and future challenges. *Science* **2021**, *373* (6555).

(118) Hennessy, K.; Badolato, A.; Winger, M.; Gerace, D.; Atature, M.; Gulde, S.; Falt, S.; Hu, E. L.; Imamoglu, A. Quantum nature of a strongly coupled single quantum dot-cavity system. *Nature* **2007**, *445* (7130), 896-899.

(119) Lim, S. Y.; Shen, W.; Gao, Z. Carbon quantum dots and their applications. *Chem Soc Rev* **2015**, *44* (1), 362-381.

(120) Chan, W. C.; Nie, S. Quantum dot bioconjugates for ultrasensitive nonisotopic detection. *Science* **1998**, *281* (5385), 2016-2018.

(121) Lee, T.; Kim, B. J.; Lee, H.; Hahm, D.; Bae, W. K.; Lim, J.; Kwak, J. Bright and Stable Quantum Dot Light-Emitting Diodes. *Adv Mater* **2022**, *34* (4), e2106276.

(122) Liu, X.; Wu, W.; Cui, D.; Chen, X.; Li, W. Functional Micro-/Nanomaterials for Multiplexed Biodetection. *Adv Mater* **2021**, *33* (30), e2004734.

(123) Grazon, C.; Baer, R. C.; Kuzmanovic, U.; Nguyen, T.; Chen, M.; Zamani, M.; Chern, M.; Aquino, P.; Zhang, X.; Lecommandoux, S.; et al. A progesterone biosensor derived from microbial screening. *Nat Commun* **2020**, *11* (1), 1276.

(124) Chen, K.; Chou, L. Y. T.; Song, F.; Chan, W. C. W. Fabrication of metal nanoshell quantum-dot barcodes for biomolecular detection. *Nano Today* **2013**, *8* (3), 228-234.

(125) Pei, X.; Zhang, B.; Tang, J.; Liu, B.; Lai, W.; Tang, D. Sandwich-type immunosensors and immunoassays exploiting nanostructure labels: A review. *Anal Chim Acta* **2013**, *758*, 1-18.

(126) Baniukevic, J.; Hakki Boyaci, I.; Goktug Bozkurt, A.; Tamer, U.; Ramanavicius, A.; Ramanaviciene, A. Magnetic gold nanoparticles in SERS-based sandwich immunoassay for antigen detection by well oriented antibodies. *Biosens Bioelectron* **2013**, *43*, 281-288.

(127) Ueda, H.; Tsumoto, K.; Kubota, K.; Suzuki, E.; Nagamune, T.; Nishimura, H.; Mahoney, W. C. Open sandwich ELISA: A novel itntnunoassay based on the interchain interaction of antibody variable region. *Nature Biotechnology* **1996**, *14* (13), 1714-1718.

(128) Zhang, Q.; Dong, Z.; Dong, X.; Duan, Q.; Ji, J.; Liu, Y.; Pei, Z.; Ji, C.; Sang, S. Double-Side-Coated Grid-Type Mechanical Membrane Biosensor Based on AuNPs Self-assembly and 3D Printing. *Advanced Materials Interfaces* **2021**, *9* (3).

(129) Xiong, Q.; Lim, C. Y.; Ren, J.; Zhou, J.; Pu, K.; Chan-Park, M. B.; Mao, H.; Lam, Y. C.; Duan, H. Magnetic nanochain integrated microfluidic biochips. *Nat Commun* **2018**, *9* (1), 1743.

(130) Dong, R.; Liu, Y.; Mou, L.; Deng, J.; Jiang, X. Microfluidics-Based Biomaterials and Biodevices. *Adv Mater* **2019**, *31* (45), e1805033.

(131) Mou, L.; Jiang, X. Materials for Microfluidic Immunoassays: A Review. *Adv Healthc Mater* **2017**, *6* (15).

(132) Hassan, U.; Ghonge, T.; Reddy, B., Jr.; Patel, M.; Rappleye, M.; Taneja, I.; Tanna,

A.; Healey, R.; Manusry, N.; Price, Z.; et al. A point-of-care microfluidic biochip for quantification of CD64 expression from whole blood for sepsis stratification. *Nat Commun* **2017**, *8*, 15949.

(133) Lee, J. W. A Machine Vision System for Lane-Departure Detection. *Computer Vision and Image Understanding* **2002**, *86* (1), 52-78. DOI: 10.1006/cviu.2002.0958.

(134) Wu, Y.; Lu, Y. An intelligent machine vision system for detecting surface defects on packing boxes based on support vector machine. *Measurement and Control* **2019**, *52* (7-8), 1102-1110.

(135) Kong, W.; Zhou, L.; Wang, Y.; Zhang, J.; Liu, J.; Gao, S. A System of Driving Fatigue Detection Based on Machine Vision and Its Application on Smart Device. *Journal of Sensors* **2015**, *2015*, 1-11.

(136) Zhou, J.; Lin, P. T. Midinfrared Multispectral Detection for Real-Time and Noninvasive Analysis of the Structure and Composition of Materials. *ACS Sens* **2018**, *3* (7), 1322-1328.

(137) Patel, A. K.; Chatterjee, S.; Gorai, A. K. Development of machine vision-based ore classification model using support vector machine (SVM) algorithm. *Arabian Journal of Geosciences* **2017**, *10* (5).

(138) Hao, J.; Liu, H.; Miao, J.; Lu, R.; Zhou, Z.; Zhao, B.; Xie, B.; Cheng, J.; Wang, K.; Delville, M. H. A facile route to synthesize CdSe/ZnS thick-shell quantum dots with precisely controlled green emission properties: towards QDs based LED applications. *Sci Rep* **2019**, *9* (1), 12048.

(139) Vo, N. T.; Ngo, H. D.; Do Thi, N. P.; Nguyen Thi, K. P.; Duong, A. P.; Lam, V. Stability Investigation of Ligand-Exchanged CdSe/ZnS-Y (Y = 3-Mercaptopropionic Acid or Mercaptosuccinic Acid) through Zeta Potential Measurements. *Journal of Nanomaterials* **2016**, *2016*, 1-8.

(140) Lee, D. U.; Kim, D. H.; Choi, D. H.; Kim, S. W.; Lee, H. S.; Yoo, K. H.; Kim, T. W. Microstructural and optical properties of CdSe/CdS/ZnS core-shell-shell quantum dots. *Opt Express* **2016**, *24* (2), A350-357.

(141) Coropceanu, I.; Bawendi, M. G. Core/shell quantum dot based luminescent solar concentrators with reduced reabsorption and enhanced efficiency. *Nano Lett* **2014**, *14* (7), 4097-4101.

(142) Song, M.; Yang, M.; Hao, J. Pathogenic Virus Detection by Optical Nanobiosensors. *Cell Rep Phys Sci* **2021**, *2* (1), 100288.

(143) Chowdhury, A. D.; Takemura, K.; Li, T. C.; Suzuki, T.; Park, E. Y. Electrical pulse-induced electrochemical biosensor for hepatitis E virus detection. *Nat Commun* **2019**, *10* (1), 3737.

(144) Zhou, S.; Tu, D.; Liu, Y.; You, W.; Zhang, Y.; Zheng, W.; Chen, X. Ultrasensitive Point-of-Care Test for Tumor Marker in Human Saliva Based on Luminescence-Amplification Strategy of Lanthanide Nanoprobes. *Adv Sci (Weinh)* **2021**, *8* (5), 2002657.

(145) Shi, S.; Chen, J.; Wang, X.; Xiao, M.; Chandrasekaran, A. R.; Li, L.; Yi, C.; Pei, H. Biointerface Engineering with Nucleic Acid Materials for Biosensing Applications.

Advanced Functional Materials **2022**, *32* (37).

(146) Gao, P.; Wang, D.; Che, C.; Ma, Q.; Wu, X.; Chen, Y.; Xu, H.; Li, X.; Lin, Y.; Ding, D.; et al. Regional and functional division of functional elements of solid-state nanochannels for enhanced sensitivity and specificity of biosensing in complex matrices. *Nat Protoc* **2021**, *16* (9), 4201-4226.

(147) Kabay, G.; DeCastro, J.; Altay, A.; Smith, K.; Lu, H. W.; Capossela, A. M.; Moarefian, M.; Aran, K.; Dincer, C. Emerging Biosensing Technologies for the Diagnostics of Viral Infectious Diseases. *Adv Mater* **2022**, *34* (30), e2201085.

(148) Liu, H.; Li, Z.; Shen, R.; Li, Z.; Yang, Y.; Yuan, Q. Point-of-Care Pathogen Testing Using Photonic Crystals and Machine Vision for Diagnosis of Urinary Tract Infections. *Nano Lett* **2021**, *21* (7), 2854-2860.

(149) Catrysse, P. B.; Zhao, N.; Jin, W.; Fan, S. Subwavelength Bayer RGB color routers with perfect optical efficiency. *Nanophotonics* **2022**, *11* (10), 2381-2387.

(150) Menser, J.; Schneider, F.; Dreier, T.; Kaiser, S. A. Multi-pulse shadowgraphic RGB illumination and detection for flow tracking. *Experiments in Fluids* **2018**, *59* (6).

(151) Soderholm, K. J.; Mukherjee, R.; Longmate, J. Filler leachability of composites stored in distilled water or artificial saliva. *J Dent Res* **1996**, *75* (9), 1692-1699.

(152) Naim, F.; Messier, S.; Saucier, L.; Piette, G. Postprocessing in vitro digestion challenge to evaluate survival of Escherichia coli O157:H7 in fermented dry sausages. *Appl Environ Microbiol* **2004**, *70* (11), 6637-6642. 6642.2004.

(153) Outeiro, T. F.; Koss, D. J.; Erskine, D.; Walker, L.; Kurzawa-Akanbi, M.; Burn,

D.; Donaghy, P.; Morris, C.; Taylor, J. P.; Thomas, A.; et al. Dementia with Lewy bodies: an update and outlook. *Mol Neurodegener* **2019**, *14* (1), 5.

(154) Grad, L. I.; Rouleau, G. A.; Ravits, J.; Cashman, N. R. Clinical Spectrum of Amyotrophic Lateral Sclerosis (ALS). *Cold Spring Harb Perspect Med* **2017**, *7* (8).

(155) McAllister, B.; Gusella, J. F.; Landwehrmeyer, G. B.; Lee, J. M.; MacDonald, M. E.; Orth, M.; Rosser, A. E.; Williams, N. M.; Holmans, P.; Jones, L.; et al. Timing and Impact of Psychiatric, Cognitive, and Motor Abnormalities in Huntington Disease. *Neurology* **2021**, *96* (19), e2395-e2406.

(156) Ross, C. A.; Poirier, M. A. Protein aggregation and neurodegenerative disease. *Nat Med* **2004**, *10 Suppl*, S10-17.

(157) Foguem, C.; Manckoundia, P. Lewy Body Disease: Clinical and Pathological "Overlap Syndrome" Between Synucleinopathies (Parkinson Disease) and Tauopathies (Alzheimer Disease). *Curr Neurol Neurosci Rep* **2018**, *18* (5), 24.

(158) Braak, H.; Del Tredici, K.; Rub, U.; de Vos, R. A.; Jansen Steur, E. N.; Braak, E. Staging of brain pathology related to sporadic Parkinson's disease. *Neurobiol Aging* **2003**, *24* (2), 197-211.

(159) Moore, D. J.; West, A. B.; Dawson, V. L.; Dawson, T. M. Molecular pathophysiology of Parkinson's disease. *Annu Rev Neurosci* **2005**, *28*, 57-87.

(160) Mahul-Mellier, A. L.; Burtscher, J.; Maharjan, N.; Weerens, L.; Croisier, M.; Kuttler, F.; Leleu, M.; Knott, G. W.; Lashuel, H. A. The process of Lewy body formation, rather than simply alpha-synuclein fibrillization, is one of the major drivers of

neurodegeneration. *Proc Natl Acad Sci U S A* **2020**, *117* (9), 4971-4982.

(161) Mollenhauer, B.; Locascio, J. J.; Schulz-Schaeffer, W.; Sixel-Doring, F.; Trenkwalder, C.; Schlossmacher, M. G. alpha-Synuclein and tau concentrations in cerebrospinal fluid of patients presenting with parkinsonism: a cohort study. *Lancet Neurol* **2011**, *10* (3), 230-240.

(162) Shaw, L. M.; Vanderstichele, H.; Knapik-Czajka, M.; Clark, C. M.; Aisen, P. S.; Petersen, R. C.; Blennow, K.; Soares, H.; Simon, A.; Lewczuk, P.; et al. Cerebrospinal fluid biomarker signature in Alzheimer's disease neuroimaging initiative subjects. *Ann Neurol* **2009**, *65* (4), 403-413.

(163) Nakamura, A.; Kaneko, N.; Villemagne, V. L.; Kato, T.; Doecke, J.; Dore, V.; Fowler, C.; Li, Q. X.; Martins, R.; Rowe, C.; et al. High performance plasma amyloid-beta biomarkers for Alzheimer's disease. *Nature* **2018**, *554* (7691), 249-254.

(164) Mackmull, M. T.; Nagel, L.; Sesterhenn, F.; Muntel, J.; Grossbach, J.; Stalder, P.; Bruderer, R.; Reiter, L.; van de Berg, W. D. J.; de Souza, N.; et al. Global, in situ analysis of the structural proteome in individuals with Parkinson's disease to identify a new class of biomarker. *Nat Struct Mol Biol* **2022**, *29* (10), 978-989.

(165) Vaikath, N. N.; Majbour, N. K.; Paleologou, K. E.; Ardah, M. T.; van Dam, E.; van de Berg, W. D.; Forrest, S. L.; Parkkinen, L.; Gai, W. P.; Hattori, N.; et al. Generation and characterization of novel conformation-specific monoclonal antibodies for alpha-synuclein pathology. *Neurobiol Dis* **2015**, *79*, 81-99.

(166) Kovacs, G. G.; Wagner, U.; Dumont, B.; Pikkarainen, M.; Osman, A. A.;

Streichenberger, N.; Leisser, I.; Verchere, J.; Baron, T.; Alafuzoff, I.; et al. An antibody with high reactivity for disease-associated alpha-synuclein reveals extensive brain pathology. *Acta Neuropathol* **2012**, *124* (1), 37-50.

(167) Kumar, S. T.; Jagannath, S.; Francois, C.; Vanderstichele, H.; Stoops, E.; Lashuel, H. A. How specific are the conformation-specific alpha-synuclein antibodies? Characterization and validation of 16 alpha-synuclein conformation-specific antibodies using well-characterized preparations of alpha-synuclein monomers, fibrils and oligomers with distinct structures and morphology. *Neurobiol Dis* **2020**, *146*, 105086.

(168) Pilot, R.; Signorini, R.; Durante, C.; Orian, L.; Bhamidipati, M.; Fabris, L. A Review on Surface-Enhanced Raman Scattering. *Biosensors (Basel)* **2019**, *9* (2).

(169) Lin, X. M.; Cui, Y.; Xu, Y. H.; Ren, B.; Tian, Z. Q. Surface-enhanced Raman spectroscopy: substrate-related issues. *Anal Bioanal Chem* **2009**, *394* (7), 1729-1745.

(170) Bell, S. E. J.; Charron, G.; Cortes, E.; Kneipp, J.; de la Chapelle, M. L.; Langer, J.; Prochazka, M.; Tran, V.; Schlucker, S. Towards Reliable and Quantitative Surface-Enhanced Raman Scattering (SERS): From Key Parameters to Good Analytical Practice. *Angew Chem Int Ed Engl* **2020**, *59* (14), 5454-5462.

(171) Cheng, H. W.; Xue, S. Y.; Li, J.; Gordon, J. S.; Wang, S.; Filippone, N. R.; Ngo, Q. M.; Zhong, C. J. Assessing Plasmonic Nanoprobes in Electromagnetic Field Enhancement for SERS Detection of Biomarkers. *Sensors (Basel)* **2021**, *21* (24).

(172) Li, C.; Huang, Y.; Li, X.; Zhang, Y.; Chen, Q.; Ye, Z.; Alqarni, Z.; Bell, S. E. J.; Xu, Y. Towards practical and sustainable SERS: a review of recent developments in the

construction of multifunctional enhancing substrates. *Journal of Materials Chemistry C* **2021**, *9* (35), 11517-11552.

(173) Shang, Y.; Min, C.; Hu, J.; Wang, T.; Liu, H.; Hu, Y. Synthesis of gold nanoparticles by reduction of HAuCl4 under UV irradiation. *Solid State Sciences* **2013**, *15*, 17-23.

(174) Liu, T.; Liu, Z.; Jagota, A.; Hui, C.-Y. Droplets on an elastic membrane: Configurational energy balance and modified Young equation. *Journal of the Mechanics and Physics of Solids* **2020**, *138*. DOI: 10.1016/j.jmps.2020.103902.

(175) Dai, X.; Stogin, B. B.; Yang, S.; Wong, T. S. Slippery wenzel state. *ACS Nano* **2015**, *9* (9), 9260-9267.

(176) Liu, T. L.; Chen, Z.; Kim, C. J. Dynamic Cassie-Baxter Model. *Soft Matter* **2015**, *11* (8), 1589-1596.

(177) De Angelis, F.; Gentile, F.; Mecarini, F.; Das, G.; Moretti, M.; Candeloro, P.; Coluccio, M. L.; Cojoc, G.; Accardo, A.; Liberale, C.; et al. Breaking the diffusion limit with super-hydrophobic delivery of molecules to plasmonic nanofocusing SERS structures. *Nature Photonics* **2011**, *5* (11), 682-687.

(178) Raman Spectroscopic Characterization of Secondary Structure in Natively Unfolded Proteins: α-Synuclein. *Journal of the American Chemical Society* **2004**, *126* (8), 2399-2408.

(179) Flynn, J. D.; McGlinchey, R. P.; Walker, R. L., 3rd; Lee, J. C. Structural features of alpha-synuclein amyloid fibrils revealed by Raman spectroscopy. *J Biol Chem* **2018**,

293 (3), 767-776.